Diese Dissertation haben begutachtet:

....

DISSERTATION

Measurement of the Decays $B_s^0 \to J/\psi\phi$, $B_s^0 \to J/\psi f_2'(1525)$ and $B_s^0 \to J/\psi K^+K^-$ at Belle

ausgeführt zum Zwecke der Erlangung des akademischen Grades eines Doktors der technischen Wissenschaften unter der Leitung von

Privatdoz. Dipl.-Ing. Dr.techn. Christoph Schwanda

E141
Atominstitut der Österreichischen Universitäten

eingereicht an der Technischen Universität Wien
Fakultät für Physik

von

Dipl.-Phys. Felicitas Andrea Thorne

Matrikelnummer: 1029490
Cumberlandstraße 111/1/22, 1140 Wien

February 19th, 2014

Kurzfassung

Die fundamentalen Wechselwirkungen zwischen den Elementarteilchen werden gut durch das Standardmodell der Teilchenphysik beschrieben, welches als eine der größten Errungenschaften der modernen Physik betrachtet wird. Obwohl diese Theorie sehr erfolgreich getestet und bestätigt worden ist, ist auch bekannt, dass sie unvollständig ist, weshalb die Suche nach Physik jenseits des Standardmodells eine signifikante Rolle in heutigen Teilchenphysikexperimenten spielt.

Für die CP-verletzende Phase ϕ_s wird innerhalb des Standardmodells ein kleiner Wert vorhergesagt und es wird deshalb erwartet, dass sie sensitiv auf "neue Physik" ist. Eine der wichtigsten Moden um diese Phase zu messen ist der Zerfall $B_s^0 \to J/\psi\,\phi\,(1020)$ mit $J/\psi \to \ell^+\ell^-$ und $\phi\,(1020) \to K^+K^-$. In diesem Zusammenhang ist eine detaillierte Studie des Zerfalls $B_s^0 \to J/\psi\,K^+K^-$, in der sowohl resonante Zerfallsmoden wie $B_s^0 \to J/\psi\,\phi\,(1020)$ und $B_s^0 \to J/\psi\,f_2'\,(1525)$ als auch nichtresonante Beiträge untersucht werden, von besonderem Interesse. Obwohl die Hadronkolliderexperimente LHCb, CDF und DØ in diesem Forschungsgebiet große Fortschritte erzielt haben, gibt es immer noch offene Fragen, wie zum Beispiel die Größe des S-Wellenanteils innerhalb des $\phi\,(1020)$ Massenbereiches, bei dem das von DØ berichtete Resultat nicht mit den von LHCb und CDF gewonnenen Werten übereinstimmt, und die Präsenz einer möglichen $B_s^0 \to J/\psi\,f_0\,(980)$ Komponente wie sie kürzlich von LHCb publiziert worden ist. Da alle verfügbaren Informationen über den Zerfall $B_s^0 \to J/\psi\,K^+K^-$ bisher nur auf Resultaten der Hadronkollider-experimente basieren, ist eine Analyse, welche an einem Leptonkolliderexperiment duchgeführt wird, eine wichtige Erweiterung dieser Studien.

Diese Doktorarbeit präsentiert eine umfassende Untersuchung des Zerfalls $B_s^0 \to J/\psi\,K^+K^-$, basierend auf den vom Belle Experiment am Elektron-Positron Kollider KEKB in Tsukuba in Japan aufgezeichneten Daten. Insgesamt hat die Belle Kollaboration bei einer Schwerpunktsenergie von 10.87 GeV $(7.1 \pm 1.3) \cdot 10^6$ Ereignisse aufgezeichnet, welche jeweils ein $B_s^0\overline{B}_s^0$ Mesonenpaar enthalten. In dieser Analyse wird das B_s^0 Meson unter Verwendung der $J/\psi \to e^+e^-$ und der $J/\psi \to \mu^+\mu^-$ Zerfallsmoden vollständig rekonstruiert. Die Signalextraktion, welche auf einem 2-dimensionalen ungebinnten Maximumlikelihood-Fit basiert, ist auf simulierten Monte Carlo Daten entwickelt und gestestet worden, bevor sie auf den kompletten Belle Datensatz angewendet wurde.

Die gewonnenen Resultate für die absoluten Verzweigungsverhältnisse sind

$$\begin{aligned}\mathcal{B}\left[B_s^0 \to J/\psi\,\phi(1020)\right] =& (1.25 \pm 0.07\,(\mathrm{stat}) \pm 0.08\,(\mathrm{syst}) \pm 0.22\,(f_s))10^{-3}\\ \mathcal{B}\left[B_s^0 \to J/\psi\,f_2'\,(1525)\right] =& (0.26 \pm 0.06\,(\mathrm{stat}) \pm 0.02\,(\mathrm{syst}) \pm 0.05\,(f_s))10^{-3}\\ \mathcal{B}\left[B_s^0 \to J/\psi\,K^+K^-\right] =& (1.01 \pm 0.09\,(\mathrm{stat}) \pm 0.10\,(\mathrm{syst}) \pm 0.18\,(f_s))10^{-3}\end{aligned}$$

wobei das Verzweigungsverhältnis von $B_s^0 \to J/\psi\,f_2'\,(1525)$ relativ zu dem Verzweigungsverhältnis von $B_s^0 \to J/\psi\,\phi(1020)$ auf

$$\mathcal{B}[B_s^0 \to J/\psi\,f_2'(1525)]/\mathcal{B}[B_s^0 \to J/\psi\,\phi(1020)] = (21.5 \pm 4.9\,(\mathrm{stat}) \pm 2.6\,(\mathrm{syst}))\%$$

gemessen worden ist. Diese Werte sind mit den von den Hadronkolliderexperimenten berichteten Resultaten konsistent und wurden bei der "Particle Data Group" eingereicht, um in der nächste Edition der "Review of Particle Physics" eingebunden zu werden. Der S-Wellenanteil innerhalb des $\phi\,(1020)$ Massenbereichs wurde für die Massenregion von 1.009 GeV bis 1.028 GeV auf $(0.47 \pm 0.07 \pm 0.22^{+2.2}_{-0})\%$, und für den Bereich von 1.007 GeV bis 1.031 GeV auf $(0.57 \pm 0.09 \pm 0.26^{+2.0}_{-0})\%$ bestimmt, indem die S- und P-Wellenanteile über die invariante Kaonmassenverteilung getrennt wurden. Beide Resultate stimmen innerhalb ihrer Fehlerintervalle mit den entsprechenden Werten, die von CDF und LHCb publiziert wurden, überein. Ein möglicher Beitrag des Zerfalls $B_s^0 \to J/\psi\,f_0\,(980)$ mit $f_0\,(980) \to K^+K^-$ ist untersucht, aber nicht beobachtet worden; daher kann das LHCb Resultat nicht bestätigt werden.

Abstract

The fundamental interactions between elementary particles are well described by the Standard Model of Particle Physics, which is considered to be one of the most important achievements of modern physics. Even though this theory has been very successfully tested and confirmed on experimental data, it is also known to be incomplete, which is why the search for physics beyond the Standard Model plays a significant role in present particle physics experiments.

The CP violating phase ϕ_s is predicted to be small within the Standard Model and thus expected to be sensitive to "new physics". One of the most important modes to measure this phase is the decay $B_s^0 \to J/\psi\,\phi\,(1020)$ with $J/\psi \to \ell^+\ell^-$ and $\phi\,(1020) \to K^+K^-$. In this context, a detailed study of the decay $B_s^0 \to J/\psi\,K^+K^-$, where resonant decay modes like $B_s^0 \to J/\psi\,\phi\,(1020)$ and $B_s^0 \to J/\psi\,f_2'\,(1525)$ as well as the nonresonant contribution are investigated, is of particular interest. Although the hadron collider experiments LHCb, CDF and DØ have made huge progress in this field of research, there are still open questions such as the size of the S-wave contribution within the $\phi\,(1020)$ mass range, where the result reported by DØ does not agree with the values obtained by LHCb and CDF, and the presence of a possible $B_s^0 \to J/\psi\,f_0\,(980)$ component as recently published by LHCb. As all available information for the decay $B_s^0 \to J/\psi\,K^+K^-$ is currently based only on hadron collider results, an analysis performed at a lepton collider experiment is an important extension of these studies.

This Ph.D. thesis presents a comprehensive investigation of the decay $B_s^0 \to J/\psi\,K^+K^-$ based on the data recorded by the Belle experiment at the asymmetric energy electron-positron collider KEKB in Tsukuba, Japan. At a center-of-mass energy of 10.87 GeV, the Belle collaboration accumulated $(7.1 \pm 1.3) \cdot 10^6$ events in total, each containing a $B_s^0\overline{B}_s^0$ meson pair. In this analysis, the B_s^0 meson is fully reconstructed using the $J/\psi \to e^+e^-$ and the $J/\psi \to \mu^+\mu^-$ decay modes. The signal extraction procedure, which is based on a 2-dimensional unbinned maximum likelihood fit, has been developed and tested on Monte Carlo simulated data before it has been applied to the full Belle data set.

The obtained results for the absolute branching fractions are

$$\begin{aligned}
\mathcal{B}\left[B_s^0 \to J/\psi\,\phi(1020)\right] &= (1.25 \pm 0.07\,(\mathrm{stat}) \pm 0.08\,(\mathrm{syst}) \pm 0.22\,(f_s))10^{-3} \\
\mathcal{B}\left[B_s^0 \to J/\psi\,f_2'\,(1525)\right] &= (0.26 \pm 0.06\,(\mathrm{stat}) \pm 0.02\,(\mathrm{syst}) \pm 0.05\,(f_s))10^{-3} \\
\mathcal{B}\left[B_s^0 \to J/\psi\,K^+K^-\right] &= (1.01 \pm 0.09\,(\mathrm{stat}) \pm 0.10\,(\mathrm{syst}) \pm 0.18\,(f_s))10^{-3}
\end{aligned}$$

while the branching fraction for $B_s^0 \to J/\psi\, f_2'\,(1525)$ relative to the branching fraction for $B_s^0 \to J/\psi\, \phi(1020)$ has been measured to be

$$\mathcal{B}[B_s^0 \to J/\psi\, f_2'(1525)]/\mathcal{B}[B_s^0 \to J/\psi\, \phi(1020)] = (21.5 \pm 4.9\,(\mathrm{stat}) \pm 2.6\,(\mathrm{syst}))\%$$

These values are consistent with the results reported from the hadron collider experiments and have been submitted to the "Particle Data Group" for incorporation into the next edition of the "Review of Particle Physics". The S-wave contribution within the $\phi\,(1020)$ mass range has been determined to be $(0.47 \pm 0.07 \pm 0.22^{+2.2}_{-0})\%$ for a mass range of 1.009 GeV to 1.028 GeV, and $(0.57 \pm 0.09 \pm 0.26^{+2.0}_{-0})\%$ in the range from 1.007 GeV to 1.031 GeV, by separating the S- and P-wave components via the invariant kaon mass distribution. Within their error range both results are in agreement with the corresponding values published by CDF and LHCb. A possible contribution from the decay $B_s^0 \to J/\psi\, f_0\,(980)$ with $f_0\,(980) \to K^+K^-$ has been investigated but not observed; thus, the LHCb result cannot be confirmed.

Contents

Chapter 1

Introduction

The Standard Model of Particle Physics [1] describes the fundamental interactions between all known elementary particles and is one of the most successful theories in modern physics. However, this known matter represents only about 5% of the total energy in the universe. The remainder includes the so-called dark matter and dark energy and is not explained by the Standard Model. Moreover, at least 18 free parameters of the Standard Model, e.g. the mixing angles and particle masses, cannot be derived from the theory. Therefore, besides its success it has to be admitted that the Standard Model is still an incomplete theory, which is the driving force of many experiments to search for physics beyond the Standard Model.

One of the various options to find deviations from the Standard Model is the measurement of the CP violating phase ϕ_s which is predicted to be $\phi_s = 0.0363^{+0.0016}_{-0.015}$ rad [2] in the Standard Model. The decay $B_s^0 \to J/\psi\,\phi\,(1020)$ with $J/\psi \to \ell^+\ell^-$ and $\phi\,(1020) \to K^+K^-$ is one of the most important modes which gives access to this parameter[1] [3]. In this context, the detailed study of other decays with the final state $B_s^0 \to J/\psi\,K^+K^-$ are of great interest. During the past two years, the main discoveries in this research area were the first observation of the decay $B_s^0 \to J/\psi\,f_2'\,(1525)$ with $f_2'\,(1525) \to K^+K^-$ by the LHCb experiment [4] and its confirmation by the DØ collaboration [5], as well as the first measurement of the entire branching fraction of the decay $B_s^0 \to J/\psi\,K^+K^-$ [6] that includes resonant and nonresonant decays. Together with the branching ratio of the decay $B_s^0 \to J/\psi\,\phi\,(1020)$, which has been published by CDF [7–9] and LHCb [6], all these studies are based on the data obtained from the hadron colliders LHC (pp) and Tevatron ($p\overline{p}$).

This thesis presents a comprehensive study of the decay mode $B_s^0 \to J/\psi\,K^+K^-$.

[1] The charge conjugate decay mode is always implied throughout this thesis, if not stated otherwise.

The analysis is based on the full data sample collected by the Belle experiment when the asymmetric-energy electron-positron collider KEKB operated at the center-of-mass energy of 10.87 GeV, corresponding to the fourth radially excited $b\bar{b}$ state $\Upsilon(5S)$, the first one with an open decay into $B_s^0\overline{B}_s^0$ pairs. In the course of this study, the branching fractions for the decay modes $B_s^0 \to J/\psi\,\phi\,(1020)$, $B_s^0 \to J/\psi\,f_2'\,(1525)$ and the entire branching ratio for the decay $B_s^0 \to J/\psi\,K^+K^-$, which includes resonant as well as nonresonant contributions, are determined. Furthermore, the S-wave contribution is calculated within the $\phi\,(1020)$ mass range. It is expected to be dominated by the nonresonant decay $B_s^0 \to J/\psi\,K^+K^-$ where the spin J of the K^+K^- system is zero while the resonant decays $B_s^0 \to J/\psi\,\phi\,(1020)$ $(J = 1)$ and $B_s^0 \to J/\psi\,f_2'\,(1525)$ $(J = 2)$ are the P- and D-wave components, respectively. Compared to the hadron collider experiments, my analysis uses different methods which result in different systematic errors and thus contributes an important extension to the previous measurements. The main differences in the analysis method concern

- The reconstruction of the J/ψ meson:
  While the hadron collider experiments mostly constrain their analyses to the $J/\psi \to \mu^+\mu^-$ channel, since their muon identification capabilities exceed those for electrons, this study includes the $J/\psi \to e^+e^-$ channel as well.
- The calculation of the branching fractions:
  As the B_s^0 meson production is well defined at a lepton collider via the process $e^+e^- \to \Upsilon(5S) \to B_s^0\overline{B}_s^0$, all branching ratios are calculated as absolute values instead of using a reference decay channel.
- Determination of the S-wave contribution:
  The S-wave contribution within the $\phi\,(1020)$ mass region is separated from the P-wave component using the invariant kaon mass distribution and not by studying angular distributions as hadron collider experiments.

This thesis is organized as follows:
Chapter 2 gives a summary of the main aspects of the Standard Model of Particle Physics, including quantum electrodynamics, quantum chromodynamics and the electroweak unification including the Brout-Englert-Higgs mechanism for spontaneous symmetry breaking. It also gives an introduction to CP violation and presents the current status of the results of B_s^0 decays into $J/\psi\,K^+K^-$ final states.
Chapter 3 gives an overview of the KEKB accelerator and describes the Belle detector including its sub-detector systems.
The Belle data sample and the event reconstruction methods that were used in this

analysis are explained in chapter 4. This chapter also contains a brief description of the software tools that were used to perform this analysis.
As the whole study is performed as a blind analysis, the complete signal extraction procedure is developed and tested on Monte Carlo simulated events. Chapter 5 describes the fitting procedure and presents the results obtained on the Monte Carlo data.
Chapter 6 shows how the developed fit is used to extract the yields of the signal components and their distinction from the background. The results obtained for the absolute branching fractions and the S-wave contribution within two specific mass ranges are presented. The systematic errors are evaluated and the presence of a possible $B_s^0 \to J/\psi\, f_0\,(980)$ component is discussed.
A summary of the main results of this thesis and the conclusions are given in chapter 7.
All results presented in this thesis are published in F. Thorne et al. (Belle Collaboration), Phys. Rev. D 88, 114006 [arXiv:1309.0704 [hep-ex]] (2013).

Chapter 2

The Standard Model of particle physics

At the end of the 19th century, the electron was the first elementary particle to be discovered by physicists. Together with the proton, neutron and photon it was possible to describe the composition of ordinary matter and the main physics processes which were known around the year 1930. However, the positron, muon and pion which were later discovered in cosmic radiation, and the detection of so-called "strange particles", e.g. kaons and the lambda baryon, puzzled physicists for roughly three decades. Apart from the positron which could be interpreted by the Dirac equation, and the pion which was identified as the predicted Yukawa meson, most of these particles were not explained by theory at that time. The quark model, proposed by Gell-Mann and Zweig in 1964, was an important step towards the formulation of a theory that explains the existence of these particles. Today, the Standard Model of particle physics (SM) describes all known elementary particles and their interactions.

This chapter starts with a summary of the main characteristics of the elementary particles and fundamental forces, which is followed by a description of the important components of the SM, including the theory of quantum electrodynamics, quantum chromodynamics as well as the electroweak unification and the mechanism for the spontaneous symmetry breaking. The violation of the CP symmetry is discussed in the third section. The last section is devoted to the description of the decay $B_s^0 \to J/\psi\, K^+K^-$, which is an important mode regarding the search for physics beyond the SM, and summarizes the current status of the research for this decay mode.

2.1 The Standard Model of particle physics

The theoretical framework of the Standard Model is based on two gauge theories, described by the $SU(3)_C$ and $SU(2)_L \otimes U(1)_Y$ symmetry groups, for the strong and the unified weak and electromagnetic interactions, respectively. However, the electroweak symmetry $SU(2)_L \otimes U(1)_Y$ is spontaneously broken to the electromagnetic subgroup $U(1)_{QED}$ which is necessary in order to obtain massive $W^{\pm}$ and Z^0 bosons. The SM has been tested very precisely by the measurement of numerous observables, e.g. the anomalous magnetic moment of the electron and muon and the masses of the $W^{\pm}$ and Z^0 bosons. The agreement between theory and data is excellent which makes the SM one of the most successful achievements in particle physics.
After a short introduction of the elementary particles and fundamental interactions, this section describes the basics of the Standard Model and is mainly following the presentation in reference [1].

2.1.1 Elementary particles and fundamental interactions

Today, twelve elementary particles are known as constituents of all matter: Six leptons and six quarks. With a spin of 1/2, all these particles are fermions. Table 2.1 summarizes the main characteristics of these elementary particles. Leptons and quarks are both organized in three generations, often called "families", which have identical properties with respect to the fundamental interactions. The only differences between the three generations are the flavor quantum number and the masses of the particle. In addition to the presented fermions, the same number of antiparticles exist, which have the same mass but oppositely signed electric and color charges than the corresponding particles.
Unlike leptons, the quarks carry a so-called color charge in addition to their electric charge which means that quarks are also subject to the strong interaction. As a consequence, quarks are confined to colorless bound states ("hadrons") in form of mesons, which consist of a quark and an antiquark, or baryons (anti-baryons), which are composed of three quarks (anti-quarks). Even though this confinement is not mathematically proven yet, no free quarks have been observed so far [9]. The color quantum number was originally introduced in order to satisfy the Pauli principle for baryons consisting of three identical quarks with parallel spins, such as the Δ^{++} which contains three up-quarks.
Table 2.2 gives an overview of the three fundamental interactions[1] relevant in parti-

Generation	Lepton	Mass [9]	Charge [e]	Interaction
First	ν_e	$< 2\,\mathrm{eV}$	0	weak
	electron (e^-)	$511\,\mathrm{keV}$	-1	em, weak
Second	ν_μ	$< 0.19\,\mathrm{MeV}$	0	weak
	muon (μ^-)	$105.66\,\mathrm{MeV}$	-1	em, weak
Third	ν_τ	$< 18.2\,\mathrm{MeV}$	0	weak
	tau (τ^-)	$1776.82 \pm 0.16\,\mathrm{MeV}$	-1	em, weak

Generation	Quark	Mass [9]	Charge [e]	Interaction
First	up (u)	$2.3^{+0.7}_{-0.5}\,\mathrm{MeV}$	$+\frac{2}{3}$	em, weak, strong
	down (d)	$4.8^{+0.5}_{-0.3}\,\mathrm{MeV}$	$-\frac{1}{3}$	em, weak, strong
Second	charm (c)	$1.275 \pm 0.025\,\mathrm{GeV}$	$+\frac{2}{3}$	em, weak, strong
	strange (s)	$95 \pm 5\,\mathrm{MeV}$	$-\frac{1}{3}$	em, weak, strong
Third	top (t)	$173.07 \pm 0.52 \pm 0.72\,\mathrm{GeV}$	$+\frac{2}{3}$	em, weak, strong
	bottom (b)	$4.18 \pm 0.03\,\mathrm{GeV}$	$-\frac{1}{3}$	em, weak, strong

Table 2.1: Summary of the characteristics of leptons and quarks with regard to their mass, electric charge and the interactions they can participate (electromagnetic (em), weak and strong). The error for the electron and the muon mass is much smaller than the precision given in this table and thus is not cited.

Interaction	range	coupling constant	Boson	Mass [9]
Electromagnetic	∞	1/137	Photon (γ)	0
Weak	$\approx 10^{-18}\,\mathrm{m}$	10^{-5}	$W^\pm$	$80.385 \pm 0.015\,\mathrm{GeV}$
			Z^0	$91.1876 \pm 0.0021\,\mathrm{GeV}$
Strong	$\approx 10^{-15}\,\mathrm{m}$	1	8 gluons (g)	0

Table 2.2: Summary of the fundamental interactions with regard to their range, coupling constant (at an energy scale of approximately 1 GeV) and the corresponding gauge bosons including their mass.

cle physics processes. As stated before, the fundamental interactions result from the $SU(3)_C$ and $SU(2)_L \otimes U(1)_Y$ symmetry groups by exchanging spin 1 gauge bosons.

[1]For the sake of completeness gravity should be mentioned as the fourth fundamental interaction. However, as its strength is more than 30 orders of magnitude smaller than the weak force, its influence is negligibly small and thus not taken into account in particle physics.

The number of gauge bosons related to the interaction is given by the number of independent generators of the corresponding subgroup. As the special unitary group $SU(n)$ has $n^2 - 1$ generators, this implies 8 gauge bosons (gluons) for the strong interaction, three bosons ($W^{\pm}$,Z^0) for the weak interaction, and the photon mediating the electromagnetic interaction.
The three fundamental forces do not only vary in their relative strength and exchange bosons, but also in their range. The photon is massless, which means that the range of the electromagnetic interaction is infinite, while the weak interaction is limited to about 10^{-18} m corresponding to about 10^{-3} of the radius of an atomic nucleus due to the corresponding massive exchange bosons, as the propagator of the interaction is antiproportional to the squared boson mass. Even though the gluons are also massless bosons, the strong interaction only has a range in the order of a few femtometers because the gluons also carry color charge, which leads to confinement due to self-interactions (see section 2.1.3).

2.1.2 Quantum electrodynamics

Quantum electrodynamics (QED) is a gauge theory based on the $U(1)$ symmetry group, and describes the electromagnetic interaction between charged particles which is mediated by photons. The corresponding Lagrangian has to include the propagation of a free Dirac fermion, the propagation of the photon, and the interaction between the fermion and the photon. Starting with the Lagrangian which includes a kinetic term and a mass term for a free Dirac fermion

$$\mathcal{L}_0 = i\overline{\psi}(x)\gamma^{\mu}\partial_{\mu}\psi(x) - m\overline{\psi}(x)\psi(x) \tag{2.1}$$

with the Dirac spinor $\psi(x)$ representing the field of the fermion, its adjoint spinor $\overline{\psi}(x)$ and the Dirac matrices γ^{μ}, it can be shown that it is invariant with regard to a global $U(1)$ transformation with a constant phase θ

$$\psi(x) \rightarrow \psi'(x) = e^{iQ\theta}\psi(x) \tag{2.2}$$

According to the Noether theorem, any continuous global symmetry corresponds to a conservation law [10]. In case of the QED, the conserved parameter is the electric charge Q.
However, the Lagrangian given in equation 2.1 is no longer invariant under local transformations if the introduced phase depends on the space-time coordinate x,

$\theta \to \theta(x)$, due to the derivative ∂_μ:

$$\partial_\mu \psi(x) \to \psi'(x) = e^{iQ\theta(x)} \left(\partial_\mu + iQ\partial_\mu \theta(x)\right) \psi(x) \tag{2.3}$$

This requires to apply the same convention for all space-time coordinates as it was chosen at an initial reference point x_0, which is quite unnatural. In order to achieve an invariance of the Lagrangian under local transformations, the spin 1 gauge field $A_\mu(x)$ which corresponds to the photon, and the covariant derivative D_μ have to be introduced:

$$A_\mu(x) \to A'_\mu(x) = A_\mu(x) - \frac{1}{e}\partial_\mu \theta(x) \tag{2.4}$$

$$D_\mu \psi(x) = \left[\partial_\mu + ieQA_\mu(x)\right] \psi(x) \tag{2.5}$$

which transforms in the same way as the gauge field:

$$D_\mu \psi(x) \to (D_\mu \psi)'(x) = e^{iQ\theta(x)} D_\mu \psi(x) \tag{2.6}$$

Using this covariant derivative to rephrase the Lagrangian in equation 2.1 and adding a gauge-invariant kinetic term for the photon field $A_\mu(x)$, the final QED Lagrangian is given by:

$$\mathcal{L}_{QED} = i\overline{\psi}(x)\gamma^\mu D_\mu \psi(x) - m\overline{\psi}(x)\psi(x) - \frac{1}{4}F_{\mu\nu}(x)F^{\mu\nu}(x) \tag{2.7}$$

$$= \left[i\overline{\psi}(x)\gamma^\mu \partial_\mu \psi(x) - m\overline{\psi}(x)\psi(x)\right] - \frac{1}{4}F_{\mu\nu}(x)F^{\mu\nu}(x) - eQA_\mu(x)\overline{\psi}(x)\gamma^\mu \psi(x) \tag{2.8}$$

$$= \mathcal{L}_0 + \mathcal{L}_{kin} + \mathcal{L}_{int} \tag{2.9}$$

with the electromagnetic field strength tensor $F_{\mu\nu} = \partial_\mu A_\nu - \partial_\nu A_\mu$. Equation 2.8 consists of three terms: The first one corresponds to the motion of a free Dirac fermion, while the second term defines the propagation of the photon field $A_\mu(x)$. The last term arises from the covariant derivative and describes the interaction between the particle and the photon field. Any additional mass term $\mathcal{L}_{mass} = 1/2m^2 A^\mu(x) A_\mu(x)$ for the photon field would destroy the local gauge invariance, which means that the photon has to be massless. Indeed, the photon mass measured experimentally yields an upper limit of 10^{-18} eV [9].

2.1.3 Quantum chromodynamics

Quantum chromodynamics (QCD) is the gauge theory of strong interaction and the derivation of its Lagrangian is similar to the one used in QED. The main difference is that QCD is based on the special unitary group $SU(3)$. Thus, the corresponding $SU(3)$ transformation is given by the matrices

$$U = e^{i\frac{\lambda^a}{2}\theta_a} \quad \text{with} \quad UU^\dagger = U^\dagger U = 1 \quad \text{and} \quad det(U) = 1 \tag{2.10}$$

which are defined by the eight generators $\frac{\lambda^a}{2}$, where λ^a are the so-called Gell-Mann matrices, and a set of constant parameters θ_a.
Starting with the Lagrangian for a free quark

$$\mathcal{L}_0 = \sum_f \overline{q}_f \left(i\gamma^\mu \partial_\mu - m_f\right) q_f \tag{2.11}$$

where the corresponding quark field with color α and flavor f is labelled as q_f^α, it can be seen that the free Lagrangian is invariant under global $SU(3)$ transformations

$$q_f^\alpha \rightarrow \left(q_f^\alpha\right)' = U_\beta^\alpha \, q_f^\beta \tag{2.12}$$

which leads to the conservation of color charge.
As in the case of QED, the invariance under local $SU(3)$ transformations is required, but not fulfilled by the free Lagrangian in equation 2.11 when the parameters θ_a become dependent on the space-time coordinates, $\theta_a \rightarrow \theta_a(x)$. This is solved by introducing the covariant derivative D^μ and the spin 1 gluon gauge fields $G_a^\mu(x)$

$$D^\mu q_f = \left[\partial^\mu + ig_s \frac{\lambda^a}{2} G_a^\mu(x)\right] q_f \tag{2.13}$$

where g_s is the strong coupling constant. Thus, the quark and the gluon fields behave under an infinitesimal $SU(3)_C$ transformation as following:

$$q_f^\alpha \rightarrow \left(q_f^\alpha\right)' = q_f^\alpha + i\left(\frac{\lambda^a}{2}\right)_{\alpha\beta} \delta\theta_a \, q_f^\beta \tag{2.14}$$

$$G_a^\mu \rightarrow \left(G_a^\mu\right)' = G_a^\mu - \frac{1}{g_s}\partial^\mu\left(\delta\theta_a\right) - f^{abc}\delta\theta_b \, G_c^\mu \tag{2.15}$$

with the structure constants f^{abc}, which is defined by the commutation relation $\left[\lambda^a, \lambda^b\right] = i\, f^{abc}\lambda^c$.

The field tensors corresponding to the gauge fields are defined as

$$G_a^{\mu\nu} = \partial^\mu G_a^\nu - \partial^\nu G_a^\mu - g_s\, f^{abc}\, G_b^\mu\, G_c^\nu \tag{2.16}$$

and are used to add a kinetic term for the gluons to the free Lagrangian given in equation 2.11. The resulting QCD Lagrangian is divided into three main parts:

$$\begin{aligned}
\mathcal{L}_{QCD} &= -\frac{1}{4} G_a^{\mu\nu}\, G_{\mu\nu}^a + \sum_f \overline{q}_f \left(i\gamma^\mu D_\mu - m_f\right) q_f && (2.17)\\
&= -\frac{1}{4} \left(\partial^\mu G_a^\nu - \partial^\nu G_a^\mu\right)\left(\partial_\mu G_\nu^a - \partial_\nu G_\mu^a\right) + \sum_f \overline{q}_f^\alpha \left(i\gamma^\mu \partial_\mu - m_f\right) q_f^\alpha && (2.18)\\
&\quad - g_s\, G_a^\mu \sum_f \overline{q}_f^\alpha \gamma_\mu \left(\frac{\lambda^a}{2}\right)_{\alpha\beta} q_f^\beta && (2.19)\\
&\quad + \frac{g_s}{2} f^{abc} \left(\partial^\mu G_a^\nu - \partial^\nu G_a^\mu\right) G_\mu^b G_\nu^c - \frac{g_s^2}{4} f^{abc} f_{ade} G_b^\mu\, G_c^\nu\, G_\mu^d\, G_\nu^e && (2.20)\\
&= \mathcal{L}_{kin} + \mathcal{L}_{int} + \mathcal{L}_{selfint} && (2.21)
\end{aligned}$$

The kinetic terms presented in equation 2.18 describe the propagation of the gluon and the quark fields, respectively, while equation 2.19 defines the interaction between these fields. The two terms given in equation 2.20 arise from the fact that the $SU\,(3)_C$ symmetry group is non-Abelian and characterize the self-interactions between the gluon fields in third and fourth order, respectively, which is possible as the gluons themselves carry color charge.

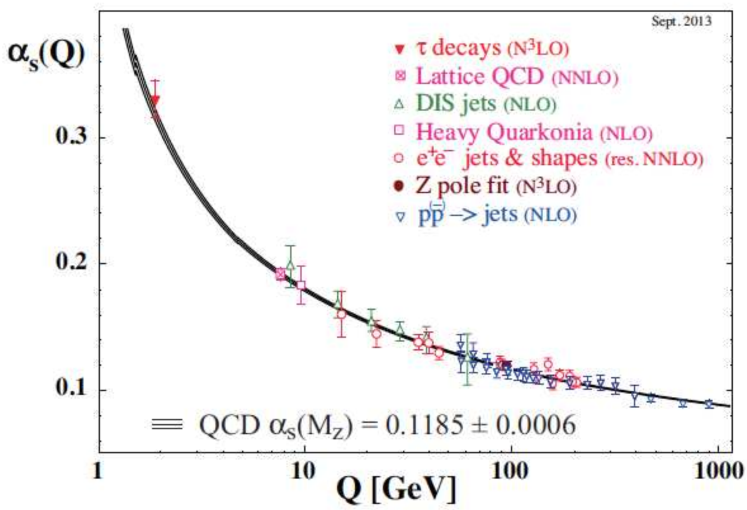

Figure 2.1: Discrete values of the strong coupling constant, here denoted as $\alpha_s\,(Q)$, are obtained from various measurements at different energy scales Q [9].

An important property of QCD can be illustrated via the energy dependence of the strong coupling constant, which is shown in figure 2.1. In contrast to the coupling constants of the electromagnetic and weak interaction which increase with energy, the strong coupling constant decreases at high energies. The confinement of quarks to colorless bound states, which was already mentioned in section 2.1.1, is visualized at low energies that correspond to large distances, where the coupling constant is strongest. However, regarding the high energy range where g_s decreases, the quarks and gluons are only weakly coupled and can be regarded as quasi free particles. This asymptotic freedom allows to approximate the QCD with perturbation theory at small distances.

2.1.4 Electroweak unification and Spontaneous Symmetry Breaking

The Standard Model combines the weak interaction with the electromagnetic one. This electroweak unification is based on the $SU(2)_L \otimes U(1)_Y$ gauge symmetry group, where the subscript L refers to the left-handed fields[2], and $Y = 2(Q - T_3)$ denotes the weak hypercharge which is defined by the electric charge Q and the third component of the weak isospin T_3. The weak interaction, which is based on the $SU(2)_L$ symmetry group of weak isospin, only affects left-handed particles and right-handed antiparticles, and all fermions are separated into left-handed doublets and right-handed singlets with respect to $SU(2)_L$:

$$\psi_1(x) = \begin{pmatrix} \nu_e \\ e^- \end{pmatrix}_L, \begin{pmatrix} u \\ d \end{pmatrix}_L \qquad \psi_2(x) = u_R \qquad \psi_3(x) = d_R, e_R^- \tag{2.22}$$

In contrast to the QED and QCD approach, the free Lagrangian does not contain a mass term, as it would mix the left- and right-handed particle fields. Therefore, it is only set up with the kinetic term:

$$\mathcal{L}_0 = \sum_{j=1}^{3} i\overline{\psi}_j(x)\gamma^\mu \partial_\mu \psi_j(x) \tag{2.23}$$

[2] A left-handed field has a negative helicity, which means that the spin and the momentum have the opposite direction, while right-handed fields have a positive helicity, where the spin and the momentum have the same orientation.

and is invariant under global $SU(2)_L \otimes U(1)_Y$ transformations, which are defined as

$$\psi_1(x) \to (\psi_1(x))' = e^{iY_1\beta} U_L \psi_1(x) \qquad \text{with} \qquad U_L = e^{i\frac{\sigma_i}{2}\alpha^i} \tag{2.24}$$
$$\psi_2(x) \to (\psi_2(x))' = e^{iY_2\beta} \psi_2(x) \tag{2.25}$$
$$\psi_3(x) \to (\psi_3(x))' = e^{iY_3\beta} \psi_3(x) \tag{2.26}$$

where σ_i are the Pauli spin matrices, and α^i and β denote the four gauge parameters. In order to obtain a Lagrangian that is also invariant under local $SU(2)_L \otimes U(1)_Y$ transformations, the covariant derivatives for the left- and right-handed fields are defined as

$$D_\mu \psi_1(x) = \left[\partial_\mu + ig\frac{\sigma_i}{2} W_\mu^i(x) + ig' Y_1 B_\mu(x)\right] \psi_1(x) \tag{2.27}$$
$$D_\mu \psi_2(x) = \left[\partial_\mu + ig' Y_2 B_\mu(x)\right] \psi_2(x) \tag{2.28}$$
$$D_\mu \psi_3(x) = \left[\partial_\mu + ig' Y_3 B_\mu(x)\right] \psi_3(x) \tag{2.29}$$

introducing coupling constants g and g' as well as the four gauge fields $W_\mu^i(x)$ and $B_\mu(x)$ which transform as follows:

$$B_\mu(x) \to B'_\mu(x) = B_\mu(x) - \frac{1}{g'}\partial_\mu \beta(x) \tag{2.30}$$
$$\frac{\sigma_i}{2} W_\mu^i(x) \to \left(\frac{\sigma_i}{2} W_\mu^i(x)\right)' = U_L(x) \frac{\sigma_i}{2} W_\mu^i(x) U_L^\dagger(x) + \frac{i}{g}\partial_\mu U_L(x) U_L^\dagger(x) \tag{2.31}$$

where $U_L(x)$ is the $SU(2)_L$ transformation in which the gauge parameter α^i depend on the space-time coordinates. While the physical fields W_μ for the charged gauge bosons $W^\pm$ can be obtained from the gauge fields W_μ^1 and W_μ^2 as

$$W_\mu^\pm = \frac{1}{\sqrt{2}}\left(W_\mu^1 \pm iW_\mu^2\right) \tag{2.32}$$

the gauge fields related to the photon and Z^0 boson are the rotations of the fields W_μ^3 and B_μ:

$$\begin{pmatrix} Z_\mu \\ A_\mu \end{pmatrix} = \begin{pmatrix} \cos(\theta_W) & -\sin(\theta_W) \\ \sin(\theta_W) & \cos(\theta_W) \end{pmatrix} \begin{pmatrix} W_\mu^3 \\ B_\mu \end{pmatrix} \tag{2.33}$$

where θ_W is the weak mixing angle (so-called Weinberg angle).
Using the gauge field tensors

$$B_{\mu\nu} = \partial_\mu B_\nu - \partial_\nu B_\mu \tag{2.34}$$

$$W^i_{\mu\nu} = \partial_\mu W^i_\nu - \partial_\nu W^i_\mu - g\epsilon^{ijk} W^j_\mu W^k_\nu \tag{2.35}$$

where ϵ^{ijk} is the Levi-Civita symbol, a kinetic term for the gauge fields is added to the free Lagrangian given in equation 2.23:

$$\mathcal{L} = \sum_{j=1}^{3} i\overline{\psi}_j(x)\gamma^\mu D_\mu \psi_j(x) - \frac{1}{4}B_{\mu\nu}B^{\mu\nu} - \frac{1}{4}W^i_{\mu\nu}W_i^{\mu\nu} \tag{2.36}$$

This Lagrangian contains the kinetic terms for the fermion and gauge fields as well as the interactions between the fermions and the $W^\pm$ bosons (the so-called charge current interaction) and between the fermions and the Z^0 boson and photon (neutral current interaction), respectively. As the $SU(2)_L$ symmetry group is a non-Abelian group, self-interactions among the gauge fields occur in third and fourth order.

Spontaneous symmetry breaking by the Brout-Englert-Higgs mechanism

Although the Lagrangian in equation 2.23 describes the kinematic structure and the interactions for the electroweak force, a mass terms for the gauge bosons have not been included as they would destroy the gauge invariance. In order to obtain massive bosons as they are observed by the experiments, the $SU(2)_L \otimes U(1)_Y$ symmetry has to be spontaneously broken. According to the Goldstone theorem [11] one additional massless boson with spin 0 occurs for every broken generator of the symmetry. The corresponding Lagrangian to describe this scalar field $\phi(x)$ is given as

$$\mathcal{L} = \partial_\mu\phi^\dagger\partial^\mu\phi - V(\phi) \qquad \text{with} \quad V(\phi) = \mu^2\phi^\dagger\phi + h\left(\phi^\dagger\phi\right)^2 \tag{2.37}$$

and is invariant under a global $U(1)$ transformation $\phi(x) \rightarrow \phi'(x) = e^{i\theta}\phi(x)$. The potential $V(\phi)$ is limited from below for positive values of the parameter h, which is necessary in order to obtain a ground state for the scalar field. The trivial solution $\phi = 0$ for the ground state arises, if the condition $\mu^2 > 0$ is fulfilled and has no further significance in this discussion. However, in the case that μ^2 is negative, an infinite number of degenerated ground states of the form $\phi_0(x) = |\phi_0|\, e^{i\theta}$ with

$|\phi_0| = \sqrt{-\frac{\mu^2}{2h}} = \frac{v}{\sqrt{2}}$ is produced due to the $U(1)$ invariance. Thus, the symmetry is spontaneously broken, when a particular ground state, e.g. $\theta = 0$, is selected.

Applying this method to the $SU(2)_L \otimes U(1)_Y$ symmetry group, that is used to describe the weak and electromagnetic interactions, the scalar field $\phi(x)$ is given as a doublet of complex scalar fields

$$\phi(x) = \begin{pmatrix} \phi^{(+)}(x) \\ \phi^{(0)}(x) \end{pmatrix} \tag{2.38}$$

and the corresponding scalar Lagrangian

$$\mathcal{L}_S = (D_\mu \phi)^\dagger D^\mu \phi - \mu^2 \phi^\dagger \phi + h\left(\phi^\dagger \phi\right)^2 \tag{2.39}$$

$$D^\mu \phi = \left[\partial^\mu + ig\frac{\sigma^i}{2} W_i^\mu + ig' Y_\phi B^\mu\right] \phi \tag{2.40}$$

is invariant under local $SU(2)_L \otimes U(1)_Y$ transformations. As before, an infinite number of degenerated ground states with an expectation value of $\left|\left\langle 0 \,\middle|\, \psi^{(0)} \,\middle|\, 0 \right\rangle\right| = \frac{v}{\sqrt{2}}$ are generated. Thus, the scalar doublet field can be written as

$$\phi(x) = e^{i\frac{\sigma_i}{2}\theta^i(x)} \frac{1}{\sqrt{2}} \begin{pmatrix} 0 \\ v + H(x) \end{pmatrix} \tag{2.41}$$

containing four fields, $\theta^i(x)$ and $H(x)$. Due to the $SU(2)_L$ invariance, there is no dependance on the fields $\theta^i(x)$, which means that the unitary gauge $\theta^i(x) = 0$ can be used. Therefore, the $SU(2)_L \otimes U(1)_Y$ symmetry is broken to the subgroup $U(1)_{QED}$ for the electromagnetic interaction by choosing this specific ground state. The three fields $\theta^i(x)$ are the massless Goldstone bosons which are produced during the spontaneous symmetry breaking, and $H(x)$ denotes the Higgs field.

Based on the chosen ground state with $\theta^i(x) = 0$, the kinetic term of the Lagrangian becomes

$$\mathcal{L}_{S,kin} = \frac{1}{2}\partial_\mu H \partial^\mu H + (v + H)^2 \left[\frac{g^2}{4} W_\mu^\dagger W^\mu + \frac{g^2}{8\cos^2(\theta_W)\, Z_\mu Z^\mu}\right] \tag{2.42}$$

establishing the masses for the $W^\pm$ and Z^0 gauge bosons as

$$M_{W^\pm} = \frac{1}{2} v g \qquad \text{and} \qquad M_{Z^0} = \frac{vg}{2\cos(\theta_W)} \tag{2.43}$$

The spontaneous symmetry breaking also provides mass terms for the quarks and charged leptons in form of Yukawa couplings to the scalar field. However, unlike the

masses of the gauge bosons, the fermion masses have to be treated as free parameters of the theory.
The Higgs boson [12] is the remaining scalar particle after the symmetry breaking and is currently identified with the boson that was discovered in 2012 at the CMS and ATLAS experiments [13, 14] at the Large Hadron Collider (LHC) at CERN. This great success lead to the award of the Nobel Prize to P. Higgs and F. Englert in 2013.

2.2 CP Violation

Unlike the continuous symmetries introduced in the previous section, the parity transformation P and the charge conjugation C are discrete symmetries, where P reverses the space coordinates of a system as $(x, y, z) \rightarrow (-x, -y, -z)$ and C transforms a particle into its anti-particle. The combination of these symmetries, labelled CP, holds a special role in the evolution of the universe as will be illustrated in the following.
In standard cosmology, the initial state of the universe is considered in cosmological models to be a hot dense state consisting only of energy. During the early expansion of the universe, pairs of particles and anti-particles were created and instantaneously annihilated into two photons. After a short timescale[3], the temperature of the universe decreased below a critical value T_c due to its continuous expansion, and the remaining average energy was insufficient to sustain pair production of particles and anti-particles. Assuming that anti-matter underlies the same decay modes as matter, all particles should have annihilated with the corresponding anti-particles, leaving behind a universe that only consists of photons, which is obviously not realized. According to A. Sacharov, the excess of matter over anti-matter and the resulting baryogenesis is based on three criteria [16]:

1. One of the fundamental interactions has to violate the C- and the CP-symmetry.

2. The universe is not in a thermal equilibrium.

3. The baryon number is not conserved.

[3]For quarks and anti-quarks this timescale corresponds to about 10^{-6} s after the so-called Big Bang (see e.g. [15]).

Therefore, the violation of the CP symmetry is a crucial issue for the explanation of the universe as observed today.
The only known source of CP violation within the Standard Model is provided by the quark mixing[4], which arises because the quark weak eigenstates are not identical to their mass eigenstates. In fact, the weak eigenstates (d', s', b') are linear combinations of the mass eigenstates (d, s, b), connected by the unitary Cabibbo-Kobayashi-Maskawa (CKM) matrix [17, 18]:

$$\begin{pmatrix} d' \\ s' \\ b' \end{pmatrix} = V_{CKM} \begin{pmatrix} d \\ s \\ b \end{pmatrix} = \begin{pmatrix} V_{ud} & V_{us} & V_{ub} \\ V_{cd} & V_{cs} & V_{cb} \\ V_{td} & V_{ts} & V_{tb} \end{pmatrix} \begin{pmatrix} d \\ s \\ b \end{pmatrix} \tag{2.44}$$

where the V_{CKM} matrix is described by a rotation with three mixing angles θ_{ij} between the generations i and j and one CP violating phase ϕ

$$V_{CKM} = \begin{pmatrix} 1 & 0 & 0 \\ 0 & c_{23} & s_{23} \\ 0 & -s_{23} & c23 \end{pmatrix} \begin{pmatrix} c_{13} & 0 & s_{13}e^{-i\phi} \\ 0 & 1 & 0 \\ -s_{13}e^{i\phi} & 0 & c_{13} \end{pmatrix} \begin{pmatrix} c_{12} & s_{12} & 0 \\ -s_{12} & c_{12} & 0 \\ 0 & 0 & 1 \end{pmatrix} \tag{2.45}$$

with $c_{ij} = \cos(\theta_{ij})$ and $s_{ij} = \sin(\theta_{ij})$, where $\theta_{12} = \theta_C$ is the so-called Cabibbo angle. Another commonly used parametrization for the CKM matrix elements is the Wolfenstein parametrization [19]

$$V_{CKM} = \begin{pmatrix} 1 - \frac{\lambda^2}{2} & \lambda & A\lambda^3(\rho - i\eta) \\ -\lambda & 1 - \frac{\lambda^2}{2} & A\lambda^2 \\ A\lambda^3(1 - \rho - i\eta) & -A\lambda^2 & 1 \end{pmatrix} + O\left(\lambda^4\right) \tag{2.46}$$

where A, λ, ρ and η are the real valued Wolfenstein parameters with $\lambda \approx 0.2 \approx \sin(\theta_C)$. Applying the unitary condition $UU^\dagger = U^\dagger U = 1$ the following relations can be extracted among the matrix elements V_{ij}:

$$V_{ud}V_{us}^* + V_{cd}V_{cs}^* + V_{td}V_{ts}^* = 0 \tag{2.47}$$
$$V_{ud}V_{ub}^* + V_{cd}V_{cb}^* + V_{td}V_{tb}^* = 0 \tag{2.48}$$
$$V_{us}V_{ub}^* + V_{cs}V_{cb}^* + V_{ts}V_{tb}^* = 0 \tag{2.49}$$

Equations 2.48 and 2.49 define the so-called "unitary triangles" for the B^0 mesons

[4]Neutrino mixing also introduces a CP violating phase which has not been measured, yet. However, as the observed neutrino oscillations require at least some of the neutrinos to be massive which is not included in the Standard Model, it is considered as a source beyond the Standard Model.

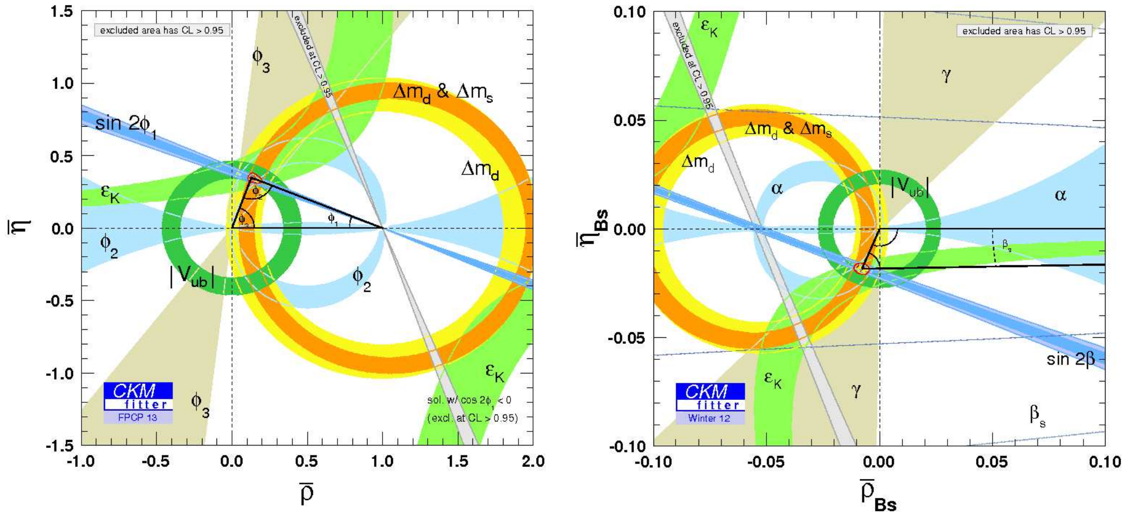

Figure 2.2: The CKM unitary triangles for the B meson (left plot) and the B_s meson system (right plot) are presented based on the fit results of the CKM matrix elements [20].

and the B_s^0 mesons, respectively. The corresponding angles ϕ_1, ϕ_2, ϕ_3 and the angle β_s of these triangles can be derived from the CKM matrix elements. Both triangles are presented in the complex plane in figure 2.2.

One important consequence arising from quark mixing is the mixing of the neutral K, B and B_s mesons with their corresponding anti-particles $\overline{K}$, $\overline{B}$ and $\overline{B}_s$, which means that for example a B_s^0 meson can oscillate into a $\overline{B}_s^0$ meson and vice versa as shown in the box diagrams in figure 2.3. The propagation of such a system is described by the Schrödinger equation[5] [21]

$$i\frac{d}{dt}\begin{pmatrix} B_s^0 \\ \overline{B}_s^0 \end{pmatrix} = \left(M - \frac{i}{2}\Gamma\right)\begin{pmatrix} B_s^0 \\ \overline{B}_s^0 \end{pmatrix} \tag{2.50}$$

with the hermitian 2×2 mass matrix M, decay matrix Γ and the flavor eigenstates B_s^0 and $\overline{B}_s^0$. The corresponding mass eigenstates B_L (mass m_L, width Γ_L) and B_H (mass m_H, width Γ_H) are generated as the linear combinations of the flavor eigenstates

$$|B_L\rangle = p\,|B_s^0\rangle + q\,|\overline{B}_s^0\rangle \tag{2.51}$$

$$|B_H\rangle = p\,|B_s^0\rangle - q\,|\overline{B}_s^0\rangle \tag{2.52}$$

where the parameters p and q are required to fulfill the normalization relation $|p|^2 + |q|^2 = 1$. The mass difference Δm_s and width difference $\Delta\Gamma_s$ of the two

[5]The following discussion is explicitly written for the B_s system

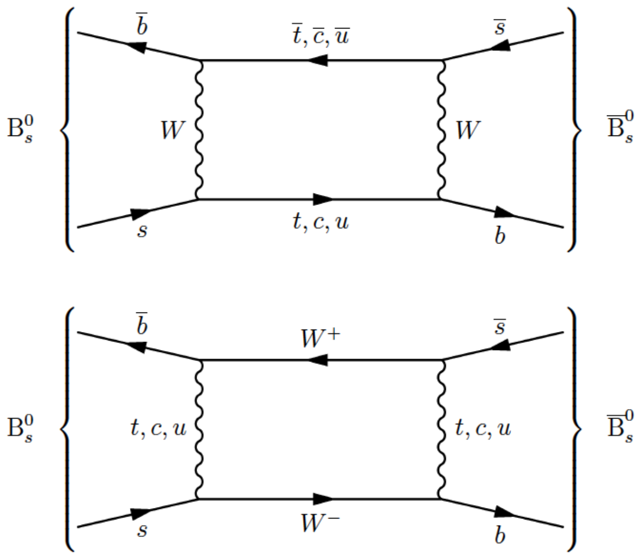

Figure 2.3: The box diagrams show the $B_s^0\overline{B}_s^0$ mixing mediated via up-type quarks (upper plot) or through the exchange of W bosons (lower plot) [22].

mass eigenstates are then defined as $\Delta m_s = m_H - m_L$ and $\Delta\Gamma_s = \Gamma_H - \Gamma_L$. As the absolute value of the off-diagonal matrix element Γ_{12} is much smaller than the absolute value of M_{12}, the mass and width difference can be simplified to [22–24]

$$\Delta m_s \approx 2\,|M_{12}| \tag{2.53}$$

$$\Delta\Gamma_s \approx 2\,|\Gamma_{12}|\cos(\phi_s) \tag{2.54}$$

introducing the CP violating phase ϕ_s. The Standard Model prediction for this phase is [2]

$$\phi_s = -2\beta_s = 0.0363^{+0.0016}_{-0.015}\,\mathrm{rad} \qquad \text{with} \quad \beta_s = arg\left(-\frac{V_{ts}V_{tb}^*}{V_{cs}V_{cb}^*}\right) \tag{2.55}$$

and thus ϕ_s is expected to be sensitive to deviations from the Standard Model as contributions from physics beyond the Standard Model can enter the $B_s^0\overline{B}_s^0$ mixing through loop diagrams and increase this parameter [25, 26]. The decay $B_s^0 \to J/\psi\,\phi\,(1020)$, which will be discussed in the next section, is a crucial mode for measuring the phase ϕ_s [3, 27–29] as its final state including two charged leptons and two charged kaons is an experimentally clean signature.
The time evolution of a state $|B^0_{\mathrm{phys}}\rangle$ which is a pure B_s^0 meson at time $t = 0$ is then

described by [21]

$$|B^0_{\text{phys}}(t)\rangle = g_+(t)\,|B^0_s\rangle + \left(\frac{q}{p}\right) g_-(t)\,|\overline{B}^0_s\rangle \tag{2.56}$$

with

$$g_+(t) = e^{-iMt}e^{-\frac{1}{2}\Gamma t}\cos\left(\frac{1}{2}\Delta m_s\, t\right) \tag{2.57}$$

$$g_-(t) = e^{-iMt}e^{-\frac{1}{2}\Gamma t}\, i\sin\left(\frac{1}{2}\Delta m_s\, t\right) \tag{2.58}$$

where M is the average from the masses m_H and m_L. As the $B^0_s\overline{B}^0_s$ oscillation is dominated by the mass difference Δm_s, the terms including $\Delta\Gamma_s$ are neglected in equations 2.56 to 2.58.

2.3 Status of B^0_s decays into $J/\psi\, K^+K^-$ final states

The decay $\mathrm{B^0_s} \to \mathrm{J}/\psi\,\mathrm{K^+K^-}$ is mediated by the charged gauge bosons of the weak interaction. The leading order Feynman diagram for this decay of the $\overline{B}^0_s$ meson is given in figure 2.4, showing the $b \to c\bar{c}s$ transition. The $\bar{b}$ (b) quark from the B^0_s ($\overline{B}^0_s$) meson emits a W^+ (W^-) boson and thus transforms into the $\bar{c}$ (c) quark, while the remaining s ($\bar{s}$) quark from the B^0_s ($\overline{B}^0_s$) is the so-called spectator quark, which is not affected by this process.
As the decay $B^0_s \to J/\psi\,\phi(1020)$ with $J/\psi \to \ell^+\ell^-$ and $\phi(1020) \to K^+K^-$ has a clean experimental signature, it has a special role in determining the CP violating phase ϕ_s and has already been studied at hadron collider experiments more than 15 years ago. However, a detailed investigation of other decay modes resulting in the

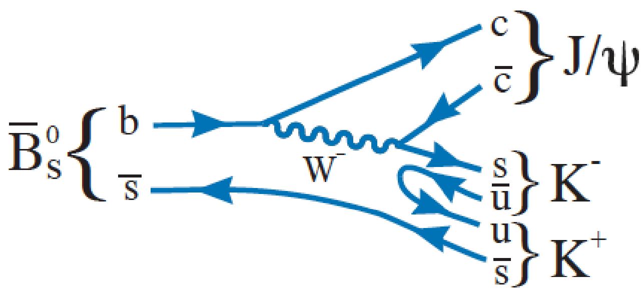

Figure 2.4: The leading order Feynman diagram for the decay $\overline{B}^0_s \to J/\psi\, K^+K^-$ [6].

same final state, e.g. the decay $B_s^0 \to J\psi f_2'(1525)$ and nonresonant contributions, as well as precise measurements of the corresponding branching fractions only have started about 3 years ago.
All available results for the decay $B_s^0 \to J/\psi\,\phi\,(1020)$ [6–9], e.g. the branching fraction, are based on measurements performed at hadron collider experiments. The situation is similar for the decay $B_s^0 \to J/\psi f_2'(1525)$, which has first been observed by the LHCb collaboration [4] and confirmed by the DØ experiment [5], as well as the measurement of the entire $B_s^0 \to J/\psi\, K^+K^-$ branching ratio which was quite recently also performed by LHCb [6]. Furthermore, LHCb claims to see a signal for the decay $B_s^0 \to J/\psi f_0\,(980)$ with $f_0\,(980) \to K^+K^-$ [6] with a yield similar to the decay $B_s^0 \to J/\psi f_2'(1525)$. However, this has not been confirmed by any other experiment, so far.
Besides the branching fraction of the mentioned decays, another crucial issue in order to improve the measurements of the phase ϕ_s is the determination of the S-wave contribution within the $\phi\,(1020)$ mass range. While the results published by the LHCb [6], CDF [27] and ATLAS [29] experiments for this parameter are in agreement with each other and found to be in the order of 1% to 2%, the value reported by the DØ collaboration [28] is approximately one order of magnitude larger.
Therefore, even though the hadron collider experiments have made huge progress in measuring the CP violating phase ϕ_s as well as studying the decay $B_s^0 \to J/\psi\, K^+K^-$, there are still several open questions. Thus, a comprehensive study of the decay $B_s^0 \to J/\psi\, K^+K^-$, based on data obtained from a lepton collider experiment includes different methods and different systematic effects than the analyses performed at hadron collider experiments, is an important extension to this field of research. As already described in chapter 1, the main differences of the analysis presented in this thesis compared to the studies published by hadron collider experiments are the reconstruction of J/ψ meson in the $J/\psi \to e^+e^-$ and the $J/\psi \to \mu^+\mu^-$ channel, the determination of absolute branching fractions which are normalized to the absolute number of B_s^0 available in the Belle data and the determination of the S-wave contribution which will be determined via the invariant kaon mass distribution.

Chapter 3

The Belle Experiment

The Belle experiment is performed by an international collaboration consisting of 496 scientists from 80 institutes distributed over four continents (as of February 2014). Its main goal is the measurement of the CP violation in the $B\bar{B}$ system and the test of the Cabibbo-Kobayashi-Maskawa (CKM) mechanism [17, 18].
The Belle detector is located at the KEKB asymmetric-energy electron-positron collider. The experiment started data acquisition in 1999 and operated until summer 2010. During this runtime the KEKB accelerator as well as the detector had a very good performance and the experiment collected about 772 million $B\overline{B}$ and about 7.1 million $B_s^0\overline{B}_s^0$ meson pairs. With this large data sample it was possible to confirm the predictions of the CKM mechanism which led to the award of the Nobel price in physics to Kobayashi and Maskawa in 2008. Besides this achievement, the Belle collaboration also discovered and investigated hitherto unknown resonant states, e.g. the charmonium state $X\,(3872)$ [30] and bottonium states [31].
This chapter summarizes the different aspects of the Belle experiment. The first section gives a basic overview of the KEKB accelerator, while the second section describes the Belle detector and its sub-detectors.

3.1 The KEKB accelerator

The KEKB accelerator is an asymmetric-energy electron-positron collider located in the former TRISTAN tunnel at the High Energy Accelerator Research Organization (KEK) campus in Tsukuba, Japan [32].
The performance of an accelerator is often described by its integrated luminosity $\mathcal{L} = N/\sigma$, which is defined as the number of collected events N divided by the

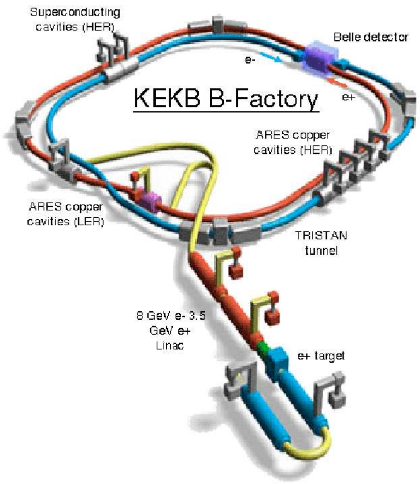

Figure 3.1: Overview of the composition of KEKB asymmetric electron-positron accelerator.

cross section σ. As the unit of the cross section is given in "barn" (b), with $1\,\mathrm{b} = 10^{-28}\,\mathrm{m}^2$, the unit of the integrated luminosity is the inverse barn (b^{-1}). With $1 \times 10^{34}\,\mathrm{cm}^{-2}s^{-1}$, the design luminosity of KEKB was planned to be approximately one order of magnitude higher compared to previous electron-positron colliders. In June 2009 the accelerator exceeded this goal by more than a factor of two.

Figure 3.1 presents a schematic overview of the accelerator. It consists of two 3016 m long storage rings which are directly filled by a preceding linear accelerator with electrons and positrons at their final energy. Beam losses, e.g. due to interactions of the electrons and positrons with remaining gas molecules in the beam pipe, are compensated by refilling both storage rings permanently. This procedure increases the data taking efficiency as it was not necessary to stop the data taking for the abort and re-injection of the beams.

The high energy ring (HER) of the KEKB collider contains electrons with an energy of 8 GeV while the 3.5 GeV positrons are injected into the low energy ring (LER)[1]. The KEKB accelerator has one interaction point (IP) where the two beams collide with a crossing angle of $\theta = 22\,\mathrm{mrad}$. To countervail the loss of the luminosity due to this crossing angle, the accelerator was operated using "crab cavities" since 2007 [33] which re-establish the head-on collisions of the electron and positron bunches despite the crossing angle.

The center-of-mass (CM) energy of the KEKB collider is

[1]These are the energies used in the "standard" operation mode of accelerator at the $\Upsilon(4S)$ resonance. Other operation modes are described in section 4.1.

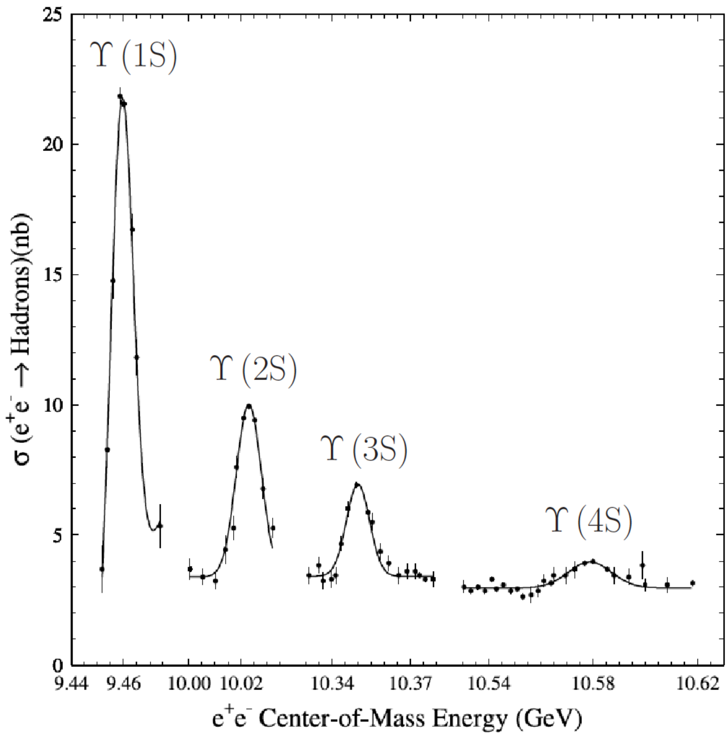

Figure 3.2: The hadronic cross section in e^+e^- collisions measured as a function of the e^+e^- center-of-mass energy. The four identified resonances are the $b\bar{b}$ ground state $\Upsilon\,(1S)$ and the first three excited states $\Upsilon\,(2S)$, $\Upsilon\,(3S)$ and $\Upsilon\,(4S)$ [34].

$$\sqrt{s} = \sqrt{2E_H E_L\,(1+\cos\theta)} = 10.58\,\text{GeV} \tag{3.1}$$

where E_H and E_L correspond to the energies of the high and low energy beams, respectively. This CM energy is chosen to correspond to the invariant mass of the third excited $b\bar{b}$ state, the so-called $\Upsilon\,(4S)$ resonance, which implies that the production cross-section for this state is maximal at this energy (see figure 3.2).
The decay process $\Upsilon\,(4S) \to B\bar{B}$ has a branching fraction of more than 96% [9], including charged and neutral B mesons[2]. The setup of this experiment implies that the B mesons are produced in pairs and furthermore that they are produced almost at rest in the center-of-mass frame. In order to measure time-dependent CP violation it is necessary to separate the decay vertices of the two B mesons, which is challenging due to their short lifetime of about 1.5 ps [9]. The solution lies within the asymmetry of the collider, creating a Lorentz boost with a boost factor of $\beta\gamma \approx 0.425$. The generated time dilation increases the flight length of the B mesons

[2]Due to the high production rate of B mesons in this kind of collider, it is often called a "B factory".

and therefore allows to distinguish their decay vertices.

3.2 The Belle Detector

The Belle detector is a large-solid-angle magnetic spectrometer which was built as a general-purpose detector covering almost the full 4π range around the interaction point. Figure 3.3 shows a schematic view of the main detector and the arrangement of the sub-detector systems. The inner part of the Belle detector is composed of a silicon vertex detector (SVD), a central drift chamber (CDC), an aerogel Cherenkov counter (ACC) and time-of-flight scintillation counters (TOF). To measure the deposited energy of the observed particles, an electromagnetic calorimeter (ECL) is used, consisting of CsI(Tl) crystals. All these components are located within a superconducting solenoid coil which provides a magnetic field of 1.5 T. The associated iron flux-return is instrumented to detect muons and K_L^0 mesons (KLM). The complete detector system is described in great detail in reference [35].
The Belle reference frame is a right-handed coordinate system. The z axis is aligned to the opposite direction of the LER beam and the y axis is defined as the vertical radial axis. The x axis is perpendicular to the y and z axes. The polar angle θ is measured from the positive z axis while the azimuthal angle ϕ is calculated from the positive x axis. Regarding the polar angle, the main parts of the detector provide a coverage of $17° \leq \theta \leq 150°$.

3.2.1 The interaction region

The precise measurement of decay vertices is mandatory for the study of CP violation. However, the resolution in z is limited due to multiple Coulomb scattering in the beam pipe and the first layer of the SVD as many of the detected particles have momenta of less than 1 Gev/c. Therefore, a reduction of the amount of material in the interaction region is required to improve the spatial resolution.
The beam pipe is a double-wall beryllium cylinder with a total material thickness of 0.3% radiation length. The inner radius of the beam pipe is 20 mm and is reduced to 15 mm around the IP [36]. The gap between the inner and the outer wall is 2.5 mm and is flushed with helium. This active cooling system removes the beam induced heat which is in the order of a few hundred watts.
Low energetic x-rays from the high energy beam are shielded by a 20 μm gold sheet, corresponding to 0.6% radiation length, located around the outer wall of the beam

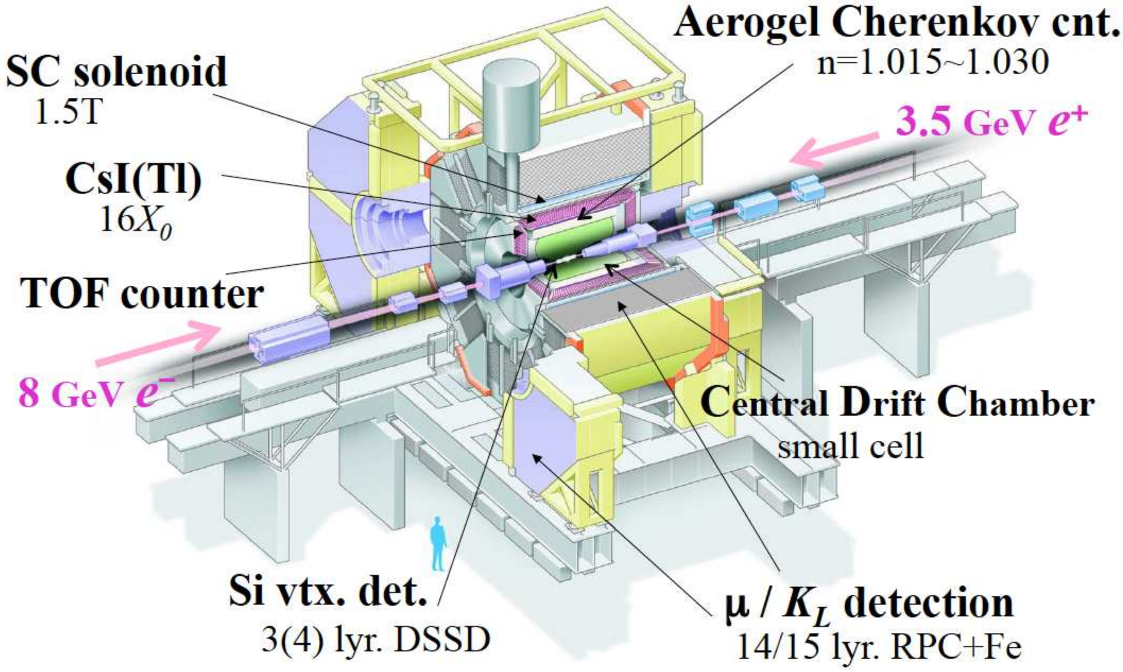

Figure 3.3: Schematic view of the Belle detector and its sub-detector system.

pipe.

3.2.2 The silicon vertex detector

In order to measure the time-dependent CP violation in the $B\bar{B}$ system, high precision in determining the difference in the z coordinate of the B meson vertices is necessary. As the B mesons travel approximately 200 μm before they decay, the required resolution in z direction is 100 μm or even better. The high accuracy applied for the vertex measurement also benefits the reconstruction of D and τ decays [35]. Moving outwards from the IP, the silicon vertex detector is the first sub-detector system of the Belle detector. It is built using double-sided silicon strip detector (DSSD), consisting of n- and p-doted silicon. By applying an external voltage and operating the pn-junction under reverse bias, the silicon bulk is fully depleted. In this state a crossing ionizing particle creates an electron-hole pair within the bulk and the thus generated current is detected as signal. To obtain 2-dimensional information for the vertex reconstruction, the cathodes and anodes of the DSSDs are segmented into strips and rotated against each other by 90°. As mentioned before, the multiple coulomb scattering is a limiting factor regarding the resolution in z direction. Thus, the SVD has to be placed as close as possible to the interaction point while the non active parts of the detector, e.g. the readout electronics, have to be outside of the detector volume to reduce the amount of material. Due to the nearby proximity of the SVD to the IP, the radiation hardness of the different components of this detector is a crucial factor.

The original SVD (SVD1) used in the Belle experiment had three layers of DSSDs which were installed at a distance of 30 mm, 45.5 mm and 60.5 mm from the IP and covered a region of $23° \leq \theta \leq 139°$ in the polar angle. As the components of the SVD1 only had a limited radiation tolerance, it was exchanged with a new SVD (SVD2) in 2003 (figure 3.4). The SVD2 was built with four layers of DSSDs located at 20 mm, 43.5 mm, 70 mm and 88 mm and the acceptance in the polar angle was extended to $17° \leq \theta \leq 150°$ which corresponds to the coverage of the central drift chamber.

Overall, the performance of the SVD was very good. Using the SVD2, the resolution of the vertex position was improved by approximately 25% compared to its predecessor [22]. The achieved resolution in z direction is 19 μm and 12 μm in the (r, ϕ) plane [37].

3.2.3 The central drift chamber

Besides a good particle identification, most of the measurements performed at the Belle experiment depend on the precise determination of the trajectories and the momenta of charged particles which are calculated via the curvature of their tracks originating within the magnetic field of the super-conducting solenoid coil and recorded by the SVD and the CDC. The central drift chamber (CDC) of the Belle detector was built to fulfill these challenges. Furthermore, it transfers information on the $(r-\phi)$

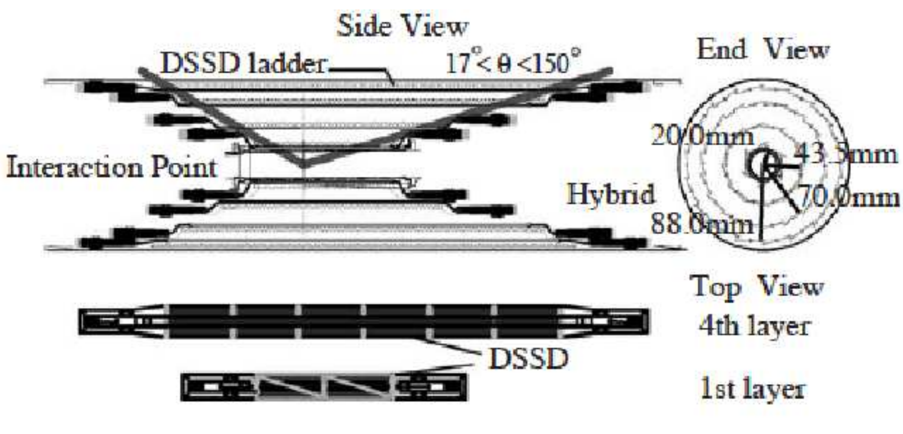

Figure 3.4: Schematic view and dimensions of the SVD2.

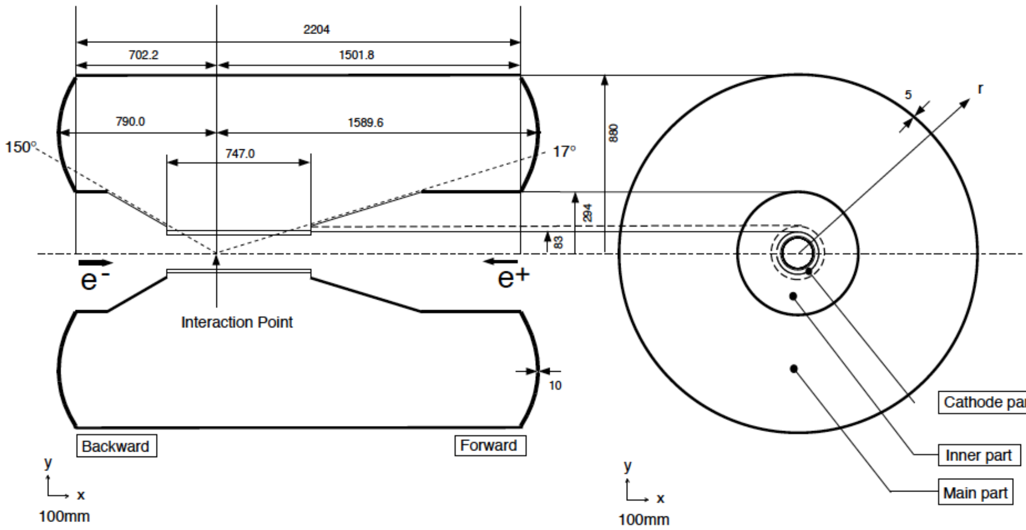

Figure 3.5: Overview on the location and the dimensions of the Belle central drift chamber [35].

plane of the tracks to the Belle trigger system which helps to distinguish physics events from beam-induced background [38].

The principle of operation of the CDC is based on gas ionization which means that a charged particle creates an electron-ion pair by exciting an electron from the outer shell of a gas atom. An applied high voltage provides a homogeneous electric field which accelerates the ionized particles and electrons to the cathode and anode, respectively. Due to the acceleration, the electrons gain enough energy to ionize additional atoms close to the anode. The thus amplified electric signal is detected.

A schematic view of the Belle CDC is given in figure 3.5. It is a cylindrical wire drift chamber with an inner radius of 103.5 mm and an outer radius of 874 mm. The polar angular coverage is $17° \leq \theta \leq 150°$. In total, the CDC consists of 50 cylindrical layers with 8400 almost square drift cells. Every drift cell contains 8 field wires built from unplated aluminium with a diameter of 126 μm and one sense wire built from gold plated tungsten with a diameter of 30 μm.

As multiple scattering is a crucial problem for measuring momenta below 1 GeV, it was decided that the used gas in the drift chamber is a mixture composed of 50% helium, which has a low atomic number, and 50% ethane, which provides a good resolution of the $d\mathrm{E}/d\mathrm{x}$ measurements. The gas mixture has a radiation length of 640 m and the drift velocity saturates at 4 cm/s even for low electric fields which is important because of the arising non-uniformities caused by the square shape of the drift cells.

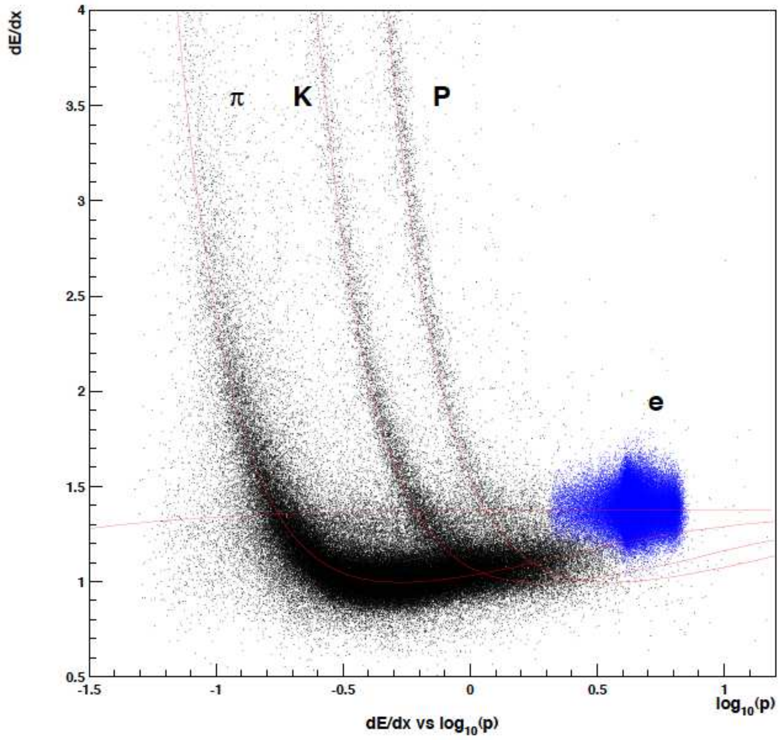

Figure 3.6: Truncated mean of dE/dx measurements from collision data plotted versus the logarithm of the observed momentum. The red lines indicate the expected distributions for pions, kaons, protons and electrons [35].

The CDC is operated within a 1.5 T magnetic field provided by a super-conducting solenoid coil. A positive high voltage of 2.35 kV is applied to the sense wires while the field wires are grounded. To avoid possible radiation damage due to the resulting electric field, the electric field strength was kept below 20 kV/cm.
The overall performance of the Belle CDC was good. The resolution of the transverse momentum P_T for muon pairs obtained from $e^+e^+ \rightarrow \mu^+\mu^-$ events is 1.85 %, while the resolution in the dE/dx measurement for these events is approximately 6 % [35, 38]. Figure 3.6 shows the dE/dx distributions for pions, kaons, protons and electrons measured with collision data which is in good agreement with the expected distribution for these particles.

3.2.4 The aerogel Cherenkov counter

To extend the momentum coverage of the Belle detector for particle identification and to improve the particle identification, especially the discrimination between charged pions and kaons, an aerogel Cherenkov counter (ACC) is installed. This

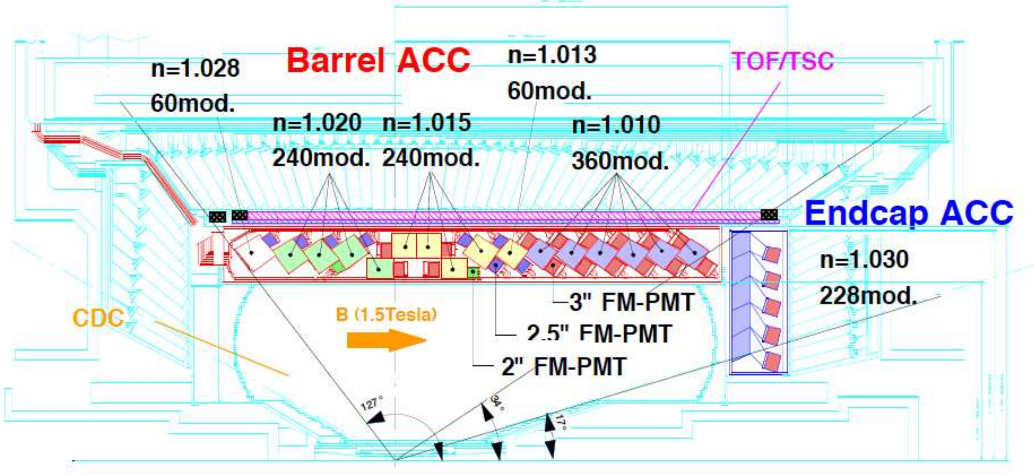

Figure 3.7: Overview of the structure and the composition of the barrel part of the Belle ACC and TOF detector systems [35].

detector measures the so-called Cherenkov light that is emitted by a particle passing through a medium with a velocity higher than the speed of light in the medium:

$$|\vec{v}| \geq \frac{c}{n}$$

Here c denotes the speed of light in vacuum and n the refraction index of the medium. This principle allows for the separation of two particles having the same momentum but different mass and therefore different velocity, by choosing a material with appropriate refraction index such that only one of the two particles will emit Cherenkov light. As only about 1% of the particle's total energy is emitted as Cherenkov light, the ACC has no significant influence on the measurement of the particle energy in the electromagnetic calorimeter.

The ACC system of the Belle experiment consists of an array of silica aerogel threshold Cherenkov counters. The barrel part of this detector is shown in figure 3.7 together with the time-of-flight detector system. It is built from 960 counter modules which are segmented into 60 cells in ϕ direction while the forward end-cap part is composed of 228 modules which are arranged in 5 concentric layers. Each module contains 5 aerogel tiles stored in a 0.2 mm thick aluminium box with the dimensions $12 \times 12 \times 12\,\mathrm{cm}^3$. One or two fine-mesh photomultiplier tubes (FM-PMTs) are attached directly to the aerogel in order to enhance the light detection efficiency. The refraction indices of the silica aerogels are chosen to lie within 1.010 and 1.028 and depend on the polar angle region where the module is installed.

The ACC covers a polar angle region of $17^\circ \leq \theta \leq 127^\circ$ and a momentum range from 1.2 GeV/c to 3.5 GeV/c which is not within the reach of the CDC. As part of the particle identification system of the Belle experiment the light yield of the ACC modules are used to calculate the likelihoods for electron-pion and kaon-pion separation. A good kaon-pion separation was first demonstrated successfully for $\mathrm{D}^{*+} \to \mathrm{D}^0\pi^+$ and $\mathrm{D}^0 \to K^-\pi^+$ decays [39].

3.2.5 The Time-of-Flight scintillation counter

The time-of-flight (TOF) system as shown in figure 3.7 is based on the detection of scintillation light emitted when the scintillator is excited by a particle and enhanced by photomultiplier tubes. A time-of-flight measurement with scintillation counters can provide useful information for particle identification. While the momentum of an incident particle is determined via the curvature of its track, the installed TOF scintillation counters determine the particle's velocity with two accurate time measurements. With this information the particle can be identified by calculating its mass.

The TOF is designed to distinguish particles with momenta below 1.2 GeV/c which applies to about 90% of all particles produced at the $\Upsilon(4S)$ resonance. Besides particle identification, the TOF also provides fast timing signals for the trigger system. In order to avoid pile-up in the trigger, the trigger rate from the TOF has to be below 70 kHz which was achieved by complementing the TOF with thin trigger scintillation counters (TSC). The fast trigger signal is then produced by averaging the signal from two ends of a TOF counter and create a coincidence with a TSC signal. The information of the TOF system is discarded if no TSC signal is observed.

The TOF detector system consists of 64 TOF/TSC modules. Every module is built by two trapezoidally shaped TOF counters and one TSC counter. A radial gap of 1.5 cm between the TOF and TSC counters reduces background from photon conversion. The modules are located at a radius of 1.2 m from the interaction point which means that a particle needs a transverse momentum of at least 0.28 GeV/c to reach the TOF counters. The detector system covers a polar angle between 34° and 120°.

With a flight path of 1.2 m, a time resolution of 100 ps is necessary to achieve a $2\,\sigma$ separation between charged pions and kaons. In order to achieve this design goal, it is important to use a fast scintillator with an attenuation length higher than 2.5 m, to minimize the time dispersion of the scintillation photons by reducing the amount of light guides and to maximize the photon collection by installing photomultiplier tubes with large-area photocathodes. The Bicron BC408 scintillator has a light propagation velocity of 14.4 cm/s and an attenuation length of 3.9 m and was therefore found to meet the first requirement. The second and the third requirements are fulfilled by attaching 2-inch fine-mesh photomultiplier tubes (FM-PMTs) directly to the TOF and TSC counters.

3.2.6 The electromagnetic calorimeter

While the identification of charged hadrons relies on the combined information of the CDC, ACC and TOF sub-detectors, the electromagnetic calorimeter (ECL) is essential for photon detection and complements the electron[3] identification. The latter is based on the comparison between the deposited energy in the ECL system and the measured momentum of the charged particle.

For the Belle experiment it is important to achieve a high efficiency in the photon detection, as there are often final state particles at the end of decay cascades with energies around 500 MeV. In addition, photons play a crucial role in rare 2-body decays, such as $B \to K^*\gamma$ and $B^0 \to \pi^0\pi^0$ with $\pi^0 \to \gamma\gamma$, in which the photons can obtain energies up to 4 GeV. Therefore, a good energy resolution over a wide energy range is very important. Furthermore, the correct reconstruction of a π^0 meson relies on the separation and the precise measurement of the opening angle of two nearby photons. This requirement can only be met with a good position resolution which is ensured by a fine-grained segmentation of the ECL.

The structure of the Belle ECL is shown in figure 3.8. It is built as a highly segmented array of Thallium doped Caesium Iodide (CsI(Tl)) crystals. These crystals were chosen as they provide a large photon yield and weak hygroscopicity. An electron or photon passing through this ECL material will lose energy due to the bremsstrahlung effect and pair production, respectively. Based on these processes, an electromagnetic shower is created inside the crystals until the energy of the particles drop below 10 MeV. At this point excitation processes and Coulomb scattering start to dominate and produce scintillation light which is then detected with silicon photodiodes. The added Thallium shifts the scintillation light into the visible spectrum. While electrons and photons will deposit their total energy inside the ECL crystals, other particles will only lose a small amount of their energy due to ionization processes.

The ECL consists of a barrel part which is 3 m in length and has an inner radius of 1.25 m as well as a forward and a backward end-cap, located at $z = +2$ m and $z = -1$ m from the IP, respectively and provides an averaged polar angle coverage

[3] In section 3.2.6, the term "electron" refers to both particles electron and positron.

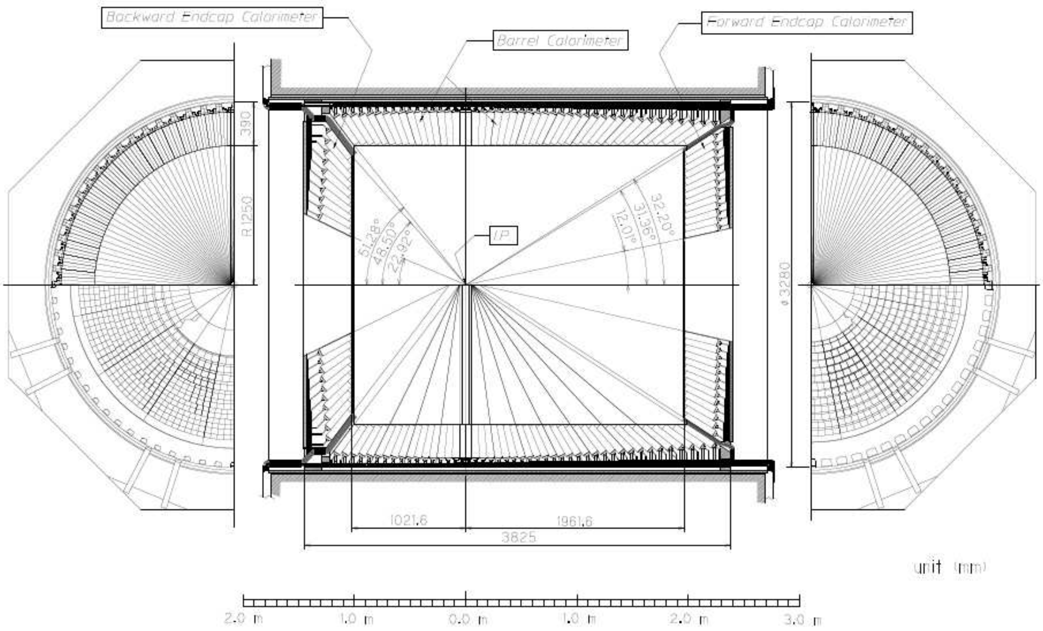

Figure 3.8: Overview on the structure and the dimensions of the Belle electromagnetic calorimeter [35].

	θ coverage	θ seg.	ϕ seg.	No. of crystals
Forward end-cap	12.4° to 31.4°	13	48 to 144	1152
Barrel	32.2° to 128.7°	46	144	6624
Backward end-cap	130.7° to 155.1°	10	64 to 144	960

Figure 3.9: Specifications for the three parts of the Belle ECL regarding the polar angle coverage and the segmentation in θ and ϕ direction as well as the number of installed CsI(Tl) crystals [35].

between 17° and 150°. More detailed information regarding the ECL specifications are given in table 3.9.

In total 8736 CsI(Tl) crystals are installed in the Belle ECL. They have a tower-like shape and point in the direction of the IP. To avoid particles escaping through the gaps between the crystals, the crystals are tilted 1.3° in θ and ϕ direction in the barrel part and 1.5° and 4° in θ direction in the forward and backward end-cap, respectively. The dimensions of the crystals installed in the barrel part of the detector are 55×55 mm^2 for the front face and 65×65 mm^2 for the rear face. Regarding the end-caps, the dimensions vary between 44.5 mm to 70.8 mm for the front face and 54 mm to 82 mm for the rear face. These dimension make sure that 80% of the energy deposited by a photon is contained within one crystal. All crystals have a length of 30 cm which corresponds to 16.2 radiation lengths and reduces the amount

of shower leakage out of the rear part of the crystal and thus improve the energy resolution.
In the end, the energy resolution is dominated by the lateral shower leakage and the electronic noise. The ECL has been calibrated using Bhabha and $e^+e^- \to \gamma\gamma$ events and the energy resolution is measured to be 1.7% in the barrel part and 1.74% and 2.85% in the forward and the backward end-cap, respectively [35].

The extreme forward calorimeter

The extreme forward calorimeter (EFC) extends the polar angle coverage to the region $6.4° \leq \theta \leq 11.5°$ in the forward direction and $163.3° \leq \theta \leq 171.2°$ in the backward direction. It also serves as a beam mask to reduce the background by shielding the CDC and as a tagging device for two-photon physics. Furthermore, the beam monitor for the KEKB control and the luminosity monitor for Belle are based on the EFC. Similarly to the ECL, this sub-detector system consists of a crystal array. However, as the EFC is positioned within a very high radiation area, the crystals are built from Bismuth Germanate (BGO, $Bi_4Ge_3O_{12}$).

3.2.7 The K_L^0 and μ detection system

Charged and neutral hadrons as well as muons and neutrinos are able to escape the electromagnetic calorimeter as they deposit only a small fraction of their energy inside the ECL crystals and have a lifetime which is long enough that they do not decay inside of the detector. Therefore, the iron flux return from the super-conducting solenoid coil, located outside of the electromagnetic calorimeter, is used as absorber material for the K_L^0 and μ detection system (KLM) and has been instrumented with glass-electrode resistive plate counters (RPCs). They consist of two parallel plate electrodes which are separated by a gap filled with gas (see figure 3.10). The electrode's bulk resistivity exceeds $10^{10}\,\Omega$cm. A particle crossing these detectors will ionize the gas and generate a local discharge of the plate electrodes, producing a signal on external pickup strips. Thus, the time and the location of the discharge is recorded.
These RPCs alternating with 4.7 cm thick iron plates make the KLM system. The barrel part (forward and backward end-caps) of the detector consists of 15 (14) detector layers. This results in a total amount of 3.9 interaction length considering a particle traveling normal to the detector layer and an additional 0.8 interaction length for K_L^0 arising from the ECL. Overall, the barrel KLM system provides a

polar angle coverage between 45° and 125° which is extended by the endcaps to $20° \leq \theta \leq 155°$. Each barrel (end-cap) detector module has 2.4 mm (2.0 mm) thick glass plates and a 1.9 mm broad gas gap. The injected gas is a non-flammable mixture of 62% HFC-134a, 30% Argon and 8% butane-silver.

A K_L^0 meson traveling through the detector will produce a shower within the ECL and a signal in the KLM system. The ECL shower is used to identify the direction of the K_L^0, but as the K_L^0 mesons and the muons escape the detector, no suitable energy measurement is possible. Basically, the K_L^0 mesons are identified by any cluster in the KLM that does not lie within 15° around a recorded track in the CDC. With this procedure, the averaged number of K_L^0 mesons per event is in agreement with the expectation which indicates that the K_L^0 identification works correctly.

Only muons with a momentum above 500 MeV/c reach the KLM. They are distinguished from charged hadrons through the different range and transverse scattering in the detector. Muons have smaller deflections than charged pions and kaons and as they deposit a smaller amount of energy in the detector than charged hadrons, they have a higher penetration depth. An overall identification efficiency of more than 90% with a fake rate of less than 5% was achieved for muons with momenta above 800 MeV/c.

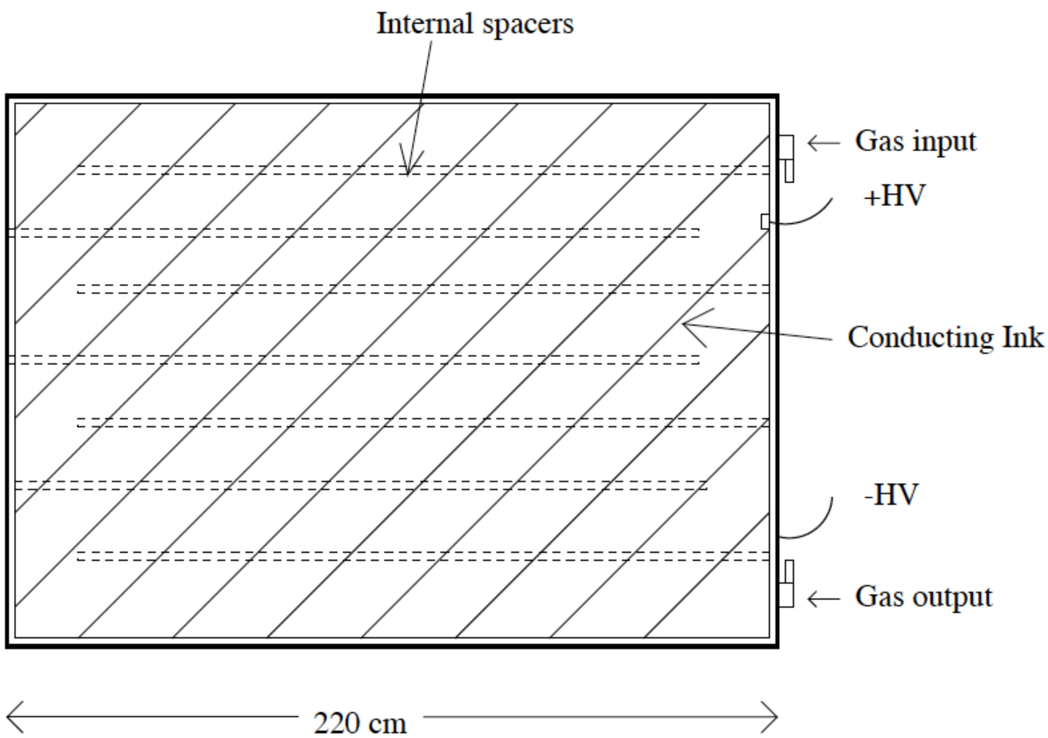

Figure 3.10: Overview of the structure of the resistive plate counters as they are used in the Belle KLM system [35].

Chapter 4

Data samples and Analysis Software

The data collected with the Belle detector is separated into experiments (experiment numbers 7 to 71 are usable for physics analysis) and is further divided into so-called runs. Each experiment was performed for a period of several month with constant basic conditions, e.g. the same quality of the vacuum in the beam pipes, while a run stopped after eight hours if no error occurred during the data taking which forces the run to abort early. Aside from the real data, a large amount of Monte Carlo (MC) data is available for investigation. Monte Carlo data consists of events obtained from an event generator, which are processed by a detector simulation in order to model the measured real data. Signal MC data only includes the decay modes that are relevant for the specific analysis, while generic MC data contains all decays listed by the Particle Data Group [9] and thus is expected to provide a reliable representation of the real data sample.

As Belle is a very mature experiment, all necessary software, e.g for event classification, track reconstruction, particle identification, is already available and included in the "Belle Analysis Software Framework" `BASF`. The raw data collected by the detector is reprocessed offline and the information important for physics analysis, e.g. the helix parameters and momenta of the reconstructed tracks, number of hits in the muon system, deposited energy in the ECL system, is stored in tabular form on data summary tapes (`dst`).

The analysis of the decay mode $B_s \to J/\psi\, K^+K^-$ is performed in different steps. At first, a pre-selection of the data is performed, which means that the number of events in the data set which was recorded on the $\Upsilon\,(5S)$ resonance is reduced by applying loose selection criteria on the event information. The remaining data is then copied from the KEK computing system to a local computing center to allow faster access to the data. Subsequently, this data will be further reduced using tight selection criteria that maximize the signal-to-background ratio for the investigated decay channel. During these processes only events passing the selection criteria will be saved for further investigation. Afterwards, a detailed study of the signal and background distributions will be performed within the `ROOT` [40] and `RooFit` [41] software environments.

The first and second part of this chapter describe the structure of the Belle $\Upsilon(5S)$ data sample and the production and composition of the MC data used in this analysis, respectively. As the computing system and analysis software of the Belle collaboration are described in detail elsewhere [42–44], the third section of this chapter only summarizes the main features of the Belle analysis software. The fourth section gives a detailed description of the event reconstruction for the decay $B_s \to J/\psi\, K^+K^-$, while the last section introduces the `ROOT` and `RooFit` analysis software and their main functions with respect to this analysis.

4.1 The Belle $\Upsilon(5S)$ data sample

Overall, the Belle detector and the KEKB accelerator performed very well and the Belle collaboration recorded a data set with an integrated luminosity of more than $1\,\mathrm{ab}^{-1}$ during the runtime of the experiment from 1999 to 2010, which significantly exceeds the luminosity collected by the BaBar experiment (see figure 4.1). As de-

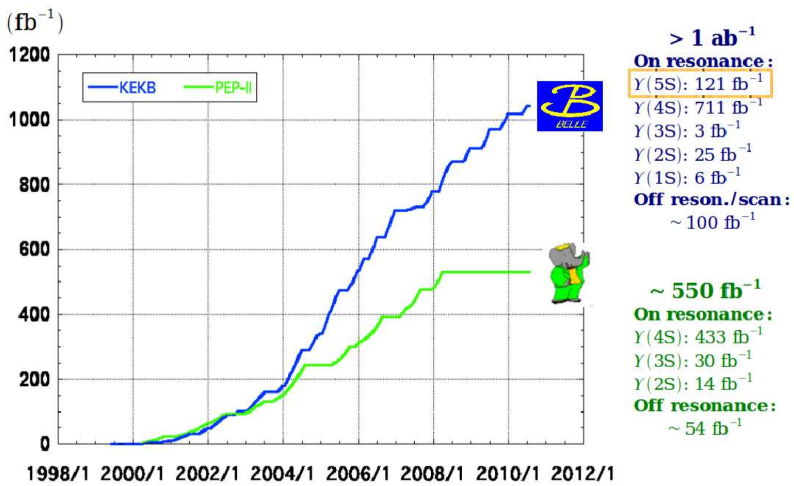

Figure 4.1: Integrated luminosity of the Belle and BaBar experiments which were performed at the KEKB and PEP-II B factories, respectively, and recorded at different center-of-mass energies. The Belle $\Upsilon(5S)$ data sample is a worldwide unique data set at lepton collider experiments.

experiment	run	$\mathcal{L}$ in $\left[\text{fb}^{-1}\right]$	date
43	1013-1034	1.857	June 2005
53	1-272	21.513	June 2006
67	98-696	27.222	Oct.-Dec. 2008
69	12-819&892-1309	47.830	Apr.-June 2009
71	27-221&2001-2244	22.938	Oct.-Dec. 2009
Total	1512	121.36	

Table 4.1: The integrated luminosity of the $\Upsilon(5S)$ data set recorded by Belle, listed by experiment and run number.

scribed in section 3.1, the KEKB accelerator produces pairs of charged or neutral B mesons at a CM energy of 10.58 GeV. The corresponding data collected at the $\Upsilon(4S)$ resonance corresponding to approximately 711 fb^{-1} is the main part of the total Belle data set, while much smaller data samples are available for studies of the $\Upsilon(\mathrm{n}S)$ $(\mathrm{n}=1,2,3)$ states.
In the years 2005 and 2006 the CLEO experiment, which was performed at the CESR electron-positron collider in Ithaca, New York, reported the first observation of B_s^0 meson production using a data sample of 0.42 fb^{-1}. CLEO had collected this data at a CM energy of about 10.86 GeV [45, 46], which approximately corresponds to the mass of the $\Upsilon(5S)$ resonance (see figure 4.2). In the same years, the Belle collaboration recorded their first data at a CM energy of 10.87 GeV in order to open the opportunity to study the properties of the B_s meson. This was achieved by increasing the energy of the KEKB electron and positron beam to 8.2 GeV and 3.6 GeV, respectively, leaving the boost factor to be the same as for the $\Upsilon(4S)$ data sample. By the year 2010 Belle had collected a luminosity of 121.4 fb^{-1} at the $\Upsilon(5S)$ resonance, which is a worldwide unique data sample at lepton collider experiments until today. A detailed record of the integrated luminosity of the $\Upsilon(5S)$ data sample according to the experiment and run numbers is given in table 4.1.
Figure 4.3 schematically illustrates the production process for the B_s^0 meson via the $\Upsilon(5S)$ resonance. The cross section for the process $e^+e^- \to b\bar{b}$ is measured to be $\sigma_{b\bar{b}} = (0.340 \pm 0.016)$ nb and was derived from the total number of $b\bar{b}$ events within the $\Upsilon(5S)$ data set [47]. The fraction of these $b\bar{b}$ states containing B_s mesons is determined to be $f_s = (17.2 \pm 3.0)\,\%$, investigating inclusive $\Upsilon(5S) \to D_s X$ and $\Upsilon(5S) \to D_0 X$ decays [47]. The total number of B_s^0 events in the full Belle $\Upsilon(5S)$ data sample is thus calculated to be

$$N_{B_s} = \mathcal{L} \cdot \sigma_{b\bar{b}} \cdot f_s = (7.1 \pm 1.3) \cdot 10^6 \tag{4.1}$$

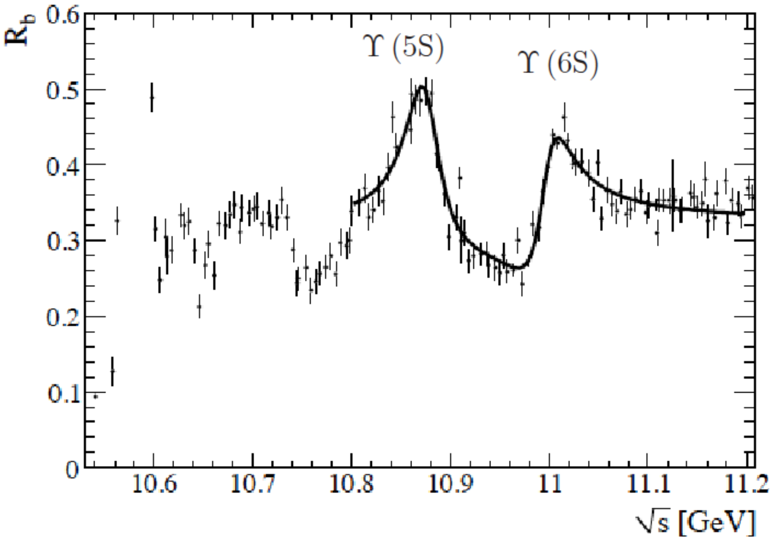

Figure 4.2: The hadronic cross section in e^+e^- collisions normalized to $\sigma\left(e^+e^- \to \mu^+\mu^-\right)$ was measured as a function of the e^+e^- center-of-mass energy. The two identified peaks are the $\Upsilon\left(5S\right)$ and $\Upsilon\left(6S\right)$ resonances [48]. The $\Upsilon\left(5S\right)$ resonance has first been observed by the CLEO collaboration [49].

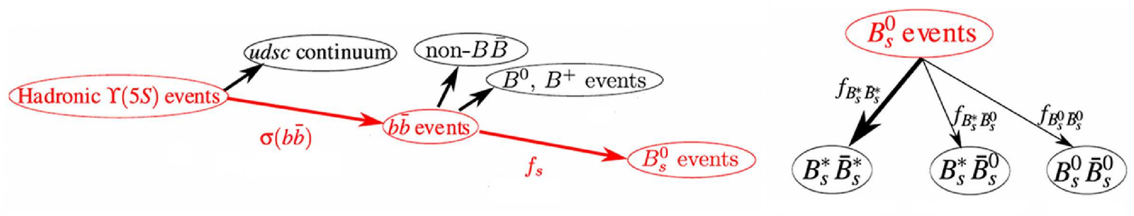

Figure 4.3: The production process of B_s^0 mesons via the $\Upsilon\left(5S\right)$ resonance is illustrated in red. The $B_s^*\bar{B}_s^*$ final state is the most abundant one in this production process.

As shown in figure 4.3, there are three different production channels for the B_s meson that are kinematically allowed. The most abundant mode is the $B_s^*\bar{B}_s^*$ final state where the B_s^* meson further decays into a B_s^0 meson via $B_s^* \to B_s^0\gamma$. The fraction of $B_s^*\bar{B}_s^*$ states within all B_s events is measured to be $f_{B_s^*\bar{B}_s^*} = (87.0 \pm 1.7)\,\%$ using a clean $B_s \to D_s^-\pi^+$ data sample [50]. The remaining two production channels, $B_s^*\bar{B}_s^0$ $\left(B_s^0\bar{B}_s^*\right)$ and $B_s^0\bar{B}_s^0$, only contribute to about 13% of all B_s events and thus usually play a minor role in most analyses performed on the $\Upsilon\left(5S\right)$ data sample.
Besides the production of a $b\bar{b}$ state, the formation of so-called continuum events with $e^+e^- \to q\bar{q}$ where q denotes an up-, down-, strange- or charm-quark is a frequently seen process and causes an important background that has to be separated from signal events during the event reconstruction (see section 4.4). In

order to allow the detailed investigation of this continuum background the Belle experiment has also taken about $88\,\mathrm{fb}^{-1}$ data at a CM energy of $10.52\,\mathrm{GeV}$ which is $60\,\mathrm{MeV}$ below the $\Upsilon(4S)$ resonance.

4.2 MC production and available MC data samples

Monte Carlo simulated data is used for several purposes in the Belle analyses, e.g. for the optimization of selection criteria with regard to the signal-to-background ratio and determination of the reconstruction efficiency as well as the investigation of the signal and background distributions in different variables. Thus, the correct simulation of the underlying physics processes and the detector response is crucial. As Belle is a very mature experiment, the software necessary for MC production and a large amount of MC data samples are accessible to every collaboration member. The MC production process includes event and detector simulation and is explained in detail in the first part of this section. The second part describes the composition of the MC data samples used in this analysis.

4.2.1 Monte Carlo data production

The production of MC simulated data is divided into two steps:

1. At first, a generator is used to simulate the decay chains that are expected to be relevant for the respective experiment or analysis, e.g. a decay of the B_s^0 meson. It produces the corresponding mesons and particles that will occur during the considered physics process according to the given decay probabilities which are usually obtained from the PDG [9]. The simulation ends when all remaining particles are so-called "stable" particles, which means that the average lifetime of these particles is high enough that they can reach the active detector material.

2. Afterwards, the information from the generator regarding the stable particles is handed over to a detector simulation which determines the detector response. At the end of this process, the such produced MC data does not only contain the same information as the real measured data but also the generator information, which means that the originally generated decay mode can be clearly identified.

For the accurate simulation of physics processes the Belle collaboration uses the `EvtGen` [51] framework. The `EvtGen` package was especially developed for the simulation of processes and decays that are relevant for the B meson factories Belle and Babar and includes for instance the mixing of B_s^0 mesons, while radiative corrections from QED photons, especially the bremsstrahlung gammas, are handled by the `PHOTOS` algorithm [54]. Figure 4.4 presents a comparison between the simulation of the energy distribution for neutral pions and the corresponding data measured at the Belle detector, which are good agreement. However, the `EvtGen` framework is not only in agreement with the Belle data, but also with the Cleo experiment [51, 55].
The simulation of the events is usually based on a generic decay table that mainly contains all known decay modes as they are listed by the Particle Data Group (PDG) [9]. The `EvtGen` framework provides this generic table, however as the generic MC data only contains a limited amount of statistics for every individual decay mode, it is not suitable for the detailed investigation of a specific process or decay. In these situations it is necessary that the user redefines the decay table and produces his own MC sample that matches the requirements of the respective analysis.
After the event simulation with `EvtGen` is finished, the information is handed over to

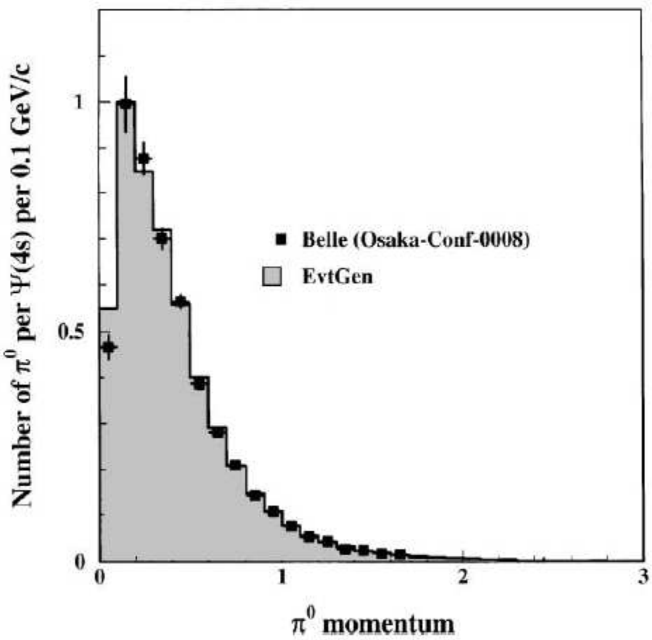

Figure 4.4: The simulation of the π^0 energy distribution is illustrated as a histogram, while the corresponding data and statistical errors measured by the Belle experiment are presented as black dots. Both distributions are in good agreement within the statistical uncertainty [51–53].

the Belle detector simulation which uses the `Geant3` package [56]. During this process, the simulation calculates the detector response, based upon e.g. the detector geometry and the interaction of the simulated particles with the detector material, adds events for beam background which are obtained from randomly triggered real data and performs the offline data reprocessing so that at the end of the simulation the same information is available as in the real data.

4.2.2 Monte Carlo data samples

During the years, a huge amount of MC data was produced with generic decay tables to match the various data samples that were collected by the Belle detector and the varying experimental conditions during the data taking. Regarding the $\Upsilon(5S)$ data, six streams of generic MC were simulated by the collaboration, including all known B_s^0 production and decay modes as well as the production and decay of other initial states arising from the $\Upsilon(5S)$ resonance and continuum background. Every stream contains the same amount of luminosity and is segmented in the same way as the real $\Upsilon(5S)$ data sample, which means that overall six times more statistics are available in MC data than what was recorded with the Belle detector.
Besides this generic MC, four different signal MC data samples were produced for this analysis in order to investigate the reconstruction efficiency for the different decay modes. The setup of the simulation of these data samples is very similar to the generic MC production. The main difference is that the decay table is adjusted so that only one of the two generated B_s^0 mesons decays according to the generic decay table, while the other B_s^0 meson is forced to undergo a specific decay. The following lines present a short quote from the `EvtGen` code that was implemented for the simulation of the different signal MC data samples:

```
Alias    MYB_s0    B_s0
Alias    MYJ/psi    J/psi
Alias    MYphi    phi
Alias    MYf'_2    f'_2
Decay MYB_s0
1.0    MYJ/psi    MYphi    SVV_HELAMP 0.7014 0.0 0.7127 0.0 0.00713 3.1416;
1.0    MYJ/psi    MYphi    SVV_HELAMP 1.0 0.0 1.0 0.0 1.0 0.0;
0.5    MYJ/psi    K+    K-    PHOTOS    PHSP;
0.2    MYJ/psi    MYf'_2    PHOTOS    PHSP;
Enddecay
```

At the beginning of the simulation, the user has to set aliases that indicate which particle decay modes from the generic decay table are redefined. In this example it affects the decay modes of the B_s^0, the J/ψ, the $\phi\,(1020)$ and the $f_2'\,(1525)$ mesons. Afterwards, the new decay modes for the respective particles are implemented. This example presents the four decays which were used for the production of the four signal MC data samples necessary for this analysis. Even though the B_s^0 decay that is cited here shows all four modes together in order to simplify the presentation, each of these lines correspond to one of the separately produced MC samples.
The number at the beginning of each line denotes the relative ratio of the respective decay mode. It is only relevant, if the user wants to simulate several decay modes simultaneously, and the sum of all relative ratios is always normalized to one by `EvtGen`. The next part of the line defines the decay mode that should be produced by `EvtGen`, which are the decays $B_s^0 \to J/\psi\phi\,(1020)$, $B_s^0 \to J/\psi K^+K^-$ and $B_s^0 \to J/\psi f_2'\,(1525)$ for this analysis. In case the user wants to activate the `PHOTOS` package, it is called after the decay was defined as shown in the third and fourth line of the example. At the end of each line, the decay model is assigned that will be used by `EvtGen` for the simulation of the respective decay. The model that is labeled as `PHSP` produces a decay according to a generic phase space, while `SVV_HELAMP` describes the decay of a scalar meson into two vector mesons. The latter requires the helicity amplitudes as input parameters, which describe the angular distribution of the decay $B_s^0 \to J/\psi\,\phi\,(1020)$ [57, 58]:

$$\begin{aligned} \frac{d^4\Gamma[B_s \to (\ell^+\ell^-)_{J/\psi}(K^+K^-)_\phi]}{d\cos\theta\; d\varphi\; d\cos\psi\; dt} &\propto 2|A_0|^2\cos^2\psi(1-\sin^2\theta\cos^2\varphi) \\ + \sin^2\psi\{|A_\parallel|^2(1-\sin^2\theta\sin^2\varphi) &+ |A_\perp|^2\sin^2\theta - \mathrm{Im}(A_\parallel^* A_\perp)\sin 2\theta\sin\varphi\} \\ + \frac{1}{\sqrt{2}}\sin 2\psi\{\mathrm{Re}(A_0^* A_\parallel)&\sin^2\theta\sin 2\varphi + \mathrm{Im}(A_0^* A_\perp)\sin 2\theta\cos\varphi\} \end{aligned} \tag{4.2}$$

Here A_0, $A_\perp$ and $A_\parallel$ denote the helicity amplitudes in the transversity frame, where the coordinate system is chosen such that the x axis is given by the direction of the $\phi\,(1020)$ meson in the J/ψ rest frame, the z axis is perpendicular to the $\phi\,(1020) \to K^+K^-$ decay plane and the y axis is defined by $p_y\,(K^+) > 0$. The direction of the positively charged lepton in the J/ψ rest frame is described by the angles θ and φ, while ψ is the angle between the momentum of the K^+ meson and the x axis in the $\phi\,(1020)$ rest frame.
For the analysis presented in this thesis two different signal MC data samples were

produced for the decay $B_s^0 \to J/\psi\phi\,(1020)$. The first one is based on the polarization parameters for this decay as they were measured by the CDF collaboration [27]. As the CDF experiment uses the transversity frame to determine the polarization parameters and Belle uses the helicity frame, the CDF values have to be recalculated according to equation 4.3 before they can be used in the simulation [21, 22]:

$$A_{\parallel} = \frac{H_+ + H_-}{\sqrt{2}} \qquad A_{\perp} = \frac{H_+ - H_-}{\sqrt{2}} \qquad A_0 = H_0 \tag{4.3}$$

The second $B_s^0 \to J/\psi\phi\,(1020)$ signal MC sample was obtained by using default values for the polarization parameters which are outside of the error range of the CDF results. This is necessary in order to study the systematic effect that arise from the $B_s^0 \to J/\psi\phi\,(1020)$ polarization (see section 6.2).
Overall, one million events were produced for each of the two $B_s^0 \to J/\psi\phi\,(1020)$ MC samples, while the $B_s^0 \to J/\psi K^+K^-$ and $B_s^0 \to J/\psi f_2'\,(1525)$ samples contain 500,000 and 200,000 events, respectively. All simulations generate the B_s^0 meson according to the three production channels introduced in section 4.1 and except for the decay $B_s^0 \to J/\psi K^+K^-$, they also take into account the $B_s^0 - \bar{B}_s^0$ mixing.
As the decay $B_s^0 \to J/\psi f_2'\,(1525)$ was discovered several years after the production of the generic MC data, it is not included in this data sample. Thus, events from the $B_s^0 \to J/\psi f_2'\,(1525)$ signal MC are merged with the available generic MC data according to the relative branching fraction of this decay that was published by the LHCb collaboration [4]. During the merging process every generic MC stream was complemented with events from a different signal MC `mdst` file and thus, all generic MC streams are still statistically independent from each other.

4.3 The Belle Analysis Software

The Belle Analysis Software Framework `BASF` is used for the event processing and the offline data analysis. To perform an analysis on Monte Carlo simulated data or events recorded by the Belle detector, the user has to write an analysis module in `Fortran`, `C` or `C++` and link it dynamically to `BASF` as a shared object. Thus, the user can load his own module together with modules from other collaborators which are then used by `BASF` to process the events in the data. The framework is configured for parallel processing of events, which reduces the runtime of the analysis module significantly for large data samples. A schematic description of `BASF` is shown in figure 4.5.

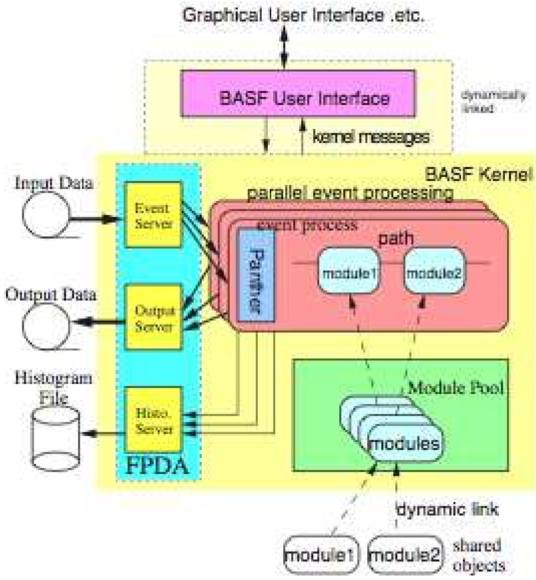

Figure 4.5: Schematic overview of the composition of the Belle Analysis Framework `BASF` [44].

The information on all recorded events is tabularly stored in so-called `Panther` tables. Some of these `Panther` tables only exist for Monte Carlo simulated events, while others are used for all types of data. The most important panther tables that were used for the analysis of the decay $B_s \to J/\psi\, K^+K^-$, are labelled `Gen_hepevt`, `MDST_Charged` and `MDST_Gamma`.
The `Gen_hepevt` table provides information on particles that are generated for Monte Carlo events. Every entry in this table is identified as a distinct particle by the Monte Carlo particle numbering scheme [9]. The user can access the status code of the particles which indicates if the corresponding particle further decays within the detector (accounts for most of the mesons) or if it is considered to be stable (applies to protons, charged kaons, charged pions, muons and electrons). Furthermore, the mother and daughter particles of every entry are listed as well as the 3-momentum of the generated particle. Thus, in this analysis the `Gen_hepevt` table is used to identify the decay mode that was generated in the investigated event before the event reconstruction (see section 4.4) is applied and to check if the reconstruction code has worked correctly. This information is crucial as it is used to determine the reconstruction efficiency.
The table labelled as `MDST_Gamma` basically gives the 3-momentum of a photon and a pointer to the `MDST_ECL` and `MDST_EFC` tables, where the energy of the associated cluster is stored. The information on all reconstructed charged tracks of an event is stored in the `MDST_Charged` table. It includes the charge and the 3-momentum of

the track as well as the mass that was used for the track fitting. The information which is necessary for particle identification is not stored in this table, but can be accessed through the `eid`, `Muid_mdst` and `atc_pid` classes of `basf` which contain the likelihood probabilities for charged tracks identified as electron, muon and hadron, respectively. The definition and calculation of the likelihood probabilities are described in section 4.3.1.
Another useful class that is implemented in the `basf` framework, is the `particle` class. This class can create a particle from any entry in the `Gen_hepevt` and `MDST_Charged` panther table when the user hands over the line of the table and a particle hypothesis. The particle class recalculates the energy of the assigned particle according to the applied hypothesis and provides this information to the user.

4.3.1 Particle Identification

The Belle particle identification is based on the ratio of likelihood values for different particle hypotheses. The likelihood value L for N independent measurements of a random variable x is defined as

$$L(\theta) = \prod_{i=1}^{N} f(x_i, \theta) \tag{4.4}$$

where $f(x, \theta)$ is the probability density function describing the distribution of x.
To identify a charged track as a kaon, pion, electron, muon or proton, the information of several sub-detector systems is combined. Depending on the hypothesis that is applied, e.g. the charged track is a kaon, different sub-detector systems are used to determine a likelihood value for this hypothesis. For kaons, pions and protons, the combined information of the ACC, TOF and the $d\mathrm{E}/d\mathrm{x}$ measurement from the CDC are used to calculate the likelihood probability

$$L = L^{ACC} \times L^{TOF} \times L^{CDC} \tag{4.5}$$

for the assumed hypothesis. In order to separate between two particles i and j and to identify that the charged track was produced by particle i, the likelihood ratio

$$PID(i:j) = \frac{L(i)}{L(i) + L(j)} \tag{4.6}$$

is determined to test the hypothesis. This ratio lies between zero and one and is a valuable discriminating variable to distinguish the different particles in an analysis

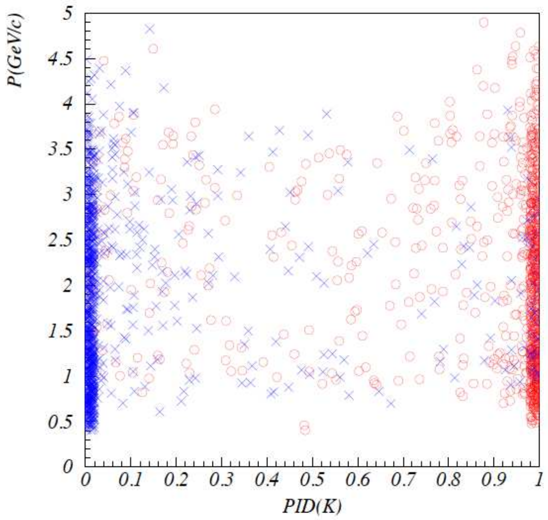

Figure 4.6: The likelihood ratio $PID\,(K:\pi)$ were the charged tracks are assumed to be a kaon and not a pion is plotted versus the measured momentum. The red circles mark the kaons while the blue crosses belong to the pion tracks. This data was obtained from $D^0 \to K^-\pi^+$ decays [35].

(see figure 4.6).

The approach to identify electrons and muons is very similar to the hadron identification. Regarding the electrons, the information from the ECL is added to the data obtained from the ACC, TOF and CDC to calculate the likelihood probability. The ratio of the energy deposited in a 3×3 and a 5×5 crystal cluster in the ECL is important to separate electrons from hadrons. The likelihood probability for a charged track to be a muon is mainly based on the number of hits in the KLM detector system and the matching of these hits with a track in the CDC and SVD. The efficiency for the electron identification in the Belle experiment is approximately 92%, while the fake rate for charged pions is only 0.25% [59]. Both values are in agreement with the Monte Carlo expectations. The muon identification provides an efficiency of approximately 90% with a fake rate between 1% and 3% for charged pions and kaons [60].

4.3.2 Event shape discrimination

As explained before, the term continuum background denotes $e^+e^- \to q\bar{q}$ processes where q is an up-, down-, charm- or strange-quark. The produced quarks hadronize and thus continuum events are formed by jets along the original directions of the quarks, while the momenta of the particles originating from a B meson decay are not

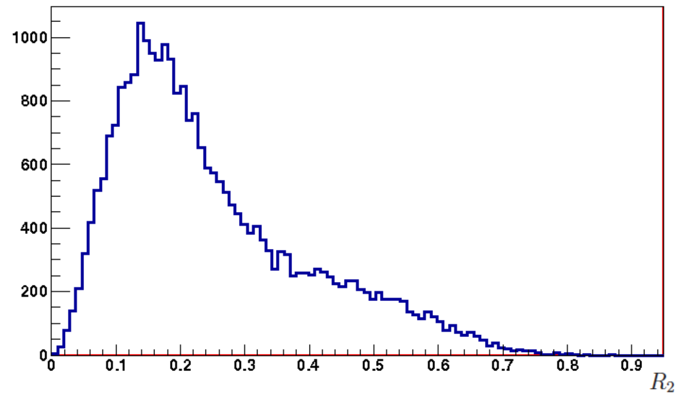

Figure 4.7: The presented distribution of the ratio of the second to zeroth Fox-Wolfram moment is obtained from five streams of generic MC data.

a priori aligned in a specific direction which results in a spherical event. Therefore, an event shape variable can be used to distinguish the continuum background. from events containing a B meson. At the Belle experiment the applied variable is the ratio of the second to zeroth Fox-Wolfram moment [61]

$$R_2 = \frac{H_2}{H_0} \tag{4.7}$$

which provides a value between zero and one for every event (see figure 4.7). Events with a small ratio are more spherical, while events with a ration close to one are mostly continuum background.

4.4 Event Reconstruction

As most Belle analyses study the decays of B or B_s mesons, the recorded amount of data is reduced by classifying the events and separating events where hadrons were produced in the final state from non-hadronic processes. The non-hadronic events mainly contain contributions from Bhabha interactions, QED processes and beam gas events, where the electron or positron beam interacts with remaining gas molecules in the beam pipe. The so-called `hadronBJ` requirement rejects a large amount of this background and mainly selects events with a hadronic final state that usually originates from a $B\bar{B}$ pair, continuum events or events containing a J/ψ meson [36, 62]. This `hadronBJ` data is stored in mini-dst (`mdst`) files on which the analysis presented in this thesis is based upon.

This analysis is a comprehensive study of the decay $B_s \to J/\psi\, K^+K^-$, including the

resonant decay modes $B_s \to J/\psi\,\phi\,(1020)$ and $B_s \to J/\psi\,f_2'\,(1525)$. All these channels have the same final state which consists of four charged particles: Two charged leptons originating from the decay $J/\psi \to \ell^+\ell^-$ with $\ell = e, \mu$ and two charged kaons which are produced either nonresonant or via one of the two resonances $\phi\,(1020)$ or $f_2'\,(1525)$.
This section describes the selection criteria that are applied to reconstruct the decay $B_s \to J/\psi\,K^+K^-$ and the study of combinatorial background.

4.4.1 Event selection criteria

The event reconstruction presented in this section was applied to signal and generic Monte Carlo (MC) data as well as the full real $\Upsilon\,(5S)$ data. The selection criteria that were implemented for the pre-selection and the final selection are summarized in table 4.2.
The point of closest approach of all investigated charged tracks is required to lie within 0.5 cm in radial direction and 4.0 cm along the beam axis with regard to the interaction point (IP). This rejects tracks that are generated from particles which enter the detector from the outside, e.g. cosmic muons, as well as tracks produced from beam induced background.
As described in section 4.3.1, the identification of the electrons and muons is based

	pre-selection	**final selection**
IP	$\lvert\mathrm{dr}\rvert \leq 0.5$ cm; $\lvert\mathrm{dz}\rvert \leq 4.0$ cm	$\lvert\mathrm{dr}\rvert \leq 0.5$ cm; $\lvert\mathrm{dz}\rvert \leq 4.0$ cm
$\mathrm{e}^\pm$	electron likelihood ≥ 0.1	electron likelihood ≥ 0.1
γ_{brems}	$\sphericalangle\left(\mathrm{p_e};\mathrm{p}_\gamma\right) \leq 5°$	$\sphericalangle\left(\mathrm{p_e};\mathrm{p}_\gamma\right) \leq 5°$
$\mu^\pm$	muon likelihood ≥ 0.1 and `muID.Chi_2()` > 0	muon likelihood ≥ 0.1 and `muID.Chi_2()` > 0
$\mathrm{K}^\pm$	kaon likelihood ≥ 0.1	kaon likelihood ≥ 0.1
J/ψ	2.86 GeV $\leq M\left(e^+e^-\left(\gamma\right)\right) \leq$ 3.34 GeV 3.0 GeV $\leq M\left(\mu^+\mu^-\right) \leq$ 3.2 GeV	2.946 GeV $\leq M\left(e^+e^-\left(\gamma\right)\right) \leq$ 3.133 GeV 3.036 GeV $\leq M\left(\mu^+\mu^-\right) \leq$ 3.133 GeV
$M\left(K^+K^-\right)$	-	$\geq$ 0.95 GeV
B_s^0	-0.4 GeV $\leq \Delta E \leq$ 0.2 GeV 5.25 GeV $\leq M_{bc} \leq$ 5.45 GeV	-0.2 GeV $\leq \Delta E \leq$ 0.1 GeV $M_{bc} >$ 5.4 GeV
event shape	-	$R_2 \leq 0.4$

Table 4.2: Summary of the selection criteria that were applied for the pre-selection (first column) and the final selection (second column) of $B_s^0 \to J/\psi\,K^+K^-$ events.

on the likelihood probability for the respective hypothesis where a lower limit of 0.1 is applied on the likelihood probability in both cases. Regarding the muons the χ^2 value , derived from the deviation of the hits in the KLM from the calculated muon track, is required to be unequal to zero, to assure that more than 1 hit was observed in the KLM system. In order to accommodate bremsstrahlung photons radiating from the electrons, possible photon candidates are searched within a cone of 5° around the electron track. If a photon is found, the electron momentum is corrected taking into account the momentum of the photon.
The decay $J/\psi \to \ell^+\ell^-$ is reconstructed by combining two oppositely charged leptons with the same flavor with the `particle` class of `BASF`. The invariant mass $M(\ell^+\ell^-)$ of the J/ψ candidate is defined by the energy-momentum relation (c is the speed of light)

$$\left[M\left(\ell^+\ell^-\right)c^2\right]^2 = \left[E\left(\ell^+\ell^-\right)\right]^2 + \left[p\left(\ell^+\ell^-\right)c\right]^2 \tag{4.8}$$

and is required to lie within 2.946 GeV $\leq M(e^+e^-(\gamma)) \leq$ 3.133 GeV when it is reconstructed in the electron channel and within 3.036 GeV $\leq M(\mu^+\mu^-) \leq$ 3.133 GeV in the muon channel. These selection criteria have been optimized for the J/ψ reconstruction in the analysis $B_s^0 \to J/\psi\,\pi^+\pi^-$ [63]. The invariant lepton mass distribution for the electron and the muon channel is shown in figure 4.8. In the whole analysis the available data is separated according to the reconstructed J/ψ decay mode and investigated independently. This procedure is necessary as each of the two decays provides a different distribution for the invariant lepton mass due to the bremsstrahlung tail which is still present in the electron channel as only less than 50% percent of the bremsstrahlung photons can be recovered. The radiative tail in the $M(e^+e^-)$ distribution results in longer tails also in other kinematic variables. Additionally, this approach provides an internal cross-check of the analysis, as the results from the electron and the muon data have to be consistent. For the final results the values obtained from both samples will be combined.
To identify two oppositely charged kaons a likelihood probability higher than 0.1 is required for the test of the kaon hypothesis against the pion hypothesis. Afterwards, the invariant kaon mass is calculated and a lower limit of $M(K^+K^-) \geq 0.95$ GeV is required to accommodate resolution effects at the lower end of the K^+K^- phase space. As no limit is set on the upper end of the phase space, it is possible to investigate the full invariant kaon mass distribution including the ϕ and $f_2'(1525)$ resonances and to search for a nonresonant contribution of the decay $B_s^0 \to J/\psi\,K^+K^-$. Finally, the B_s^0 meson is reconstructed by combining the J/ψ meson and the two identified kaons. Due to the special 2-body kinematics in the process $e^+e^- \to$

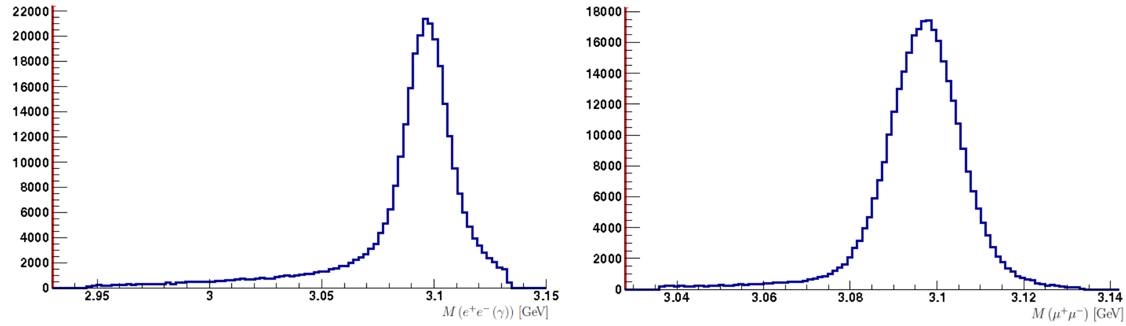

Figure 4.8: The invariant lepton mass distribution for events reconstructed in the $J/\psi \to e^+e^-$ (left) and $J/\psi \to \mu^+\mu^-$ (right) decay mode. The tail originating from the loss of bremsstrahlung photons is visible in the electron channel. The events are obtained from signal Monte Carlo simulated events for the decay $B_s^0 \to J/\psi\,\phi$.

$\Upsilon(5S) \to B_s^{(*)}\overline{B}_s^{(*)}$ the following two kinematic variables can be introduced:

$$\Delta E = E_B^* - E_{\text{beam}} \qquad \text{and} \qquad M_{bc} = \sqrt{E_{\text{beam}}^2 - (p_B^*)^2} \tag{4.9}$$

Here, E_{beam} denotes the beam energy in the center of mass frame and E_B^* and p_B^* are the energy and the momentum of the reconstructed B_s^0 meson, respectively, given in the center of mass frame.

The photon from the decay $B_s^* \to B_s^0\gamma$ is not reconstructed in this analysis, as it is very soft and has an energy of about 50 MeV, which lies at the lower end of the energy threshold that is detectable at Belle. Thus, its energy information is lost, which induces a shift in the corresponding ΔE distribution to negative values and separates the M_{bc} distribution in three disjunct signal regions depending on the number of B_s^* mesons produced in the electron-positron collision, as it is illustrated in figure 4.9.

To determine the expected significance of the signal (S) for the decay $B_s^0 \to J/\psi\,\phi$, the figure-of-merit (FoM)

$$FoM = \frac{S}{\sqrt{S+B}} \tag{4.10}$$

is studied. Here, B denotes the so-called combinatorial background which originates from events where random combinations of final state particles have passed the selection criteria. The figure-of-merit was calculated for $5.25\,\text{GeV} \leq M_{bc} \leq 5.45\,\text{GeV}$ leading to a FoM value of 14.49 taking into account all available generic Monte Carlo streams. However, restricting the M_{bc} distribution to values above 5.4 GeV shows an increase of the FoM to 24.65. Therefore, in order to increase the expected signal significance, this analysis merely selects events with $M_{bc} > 5.4$ GeV which means

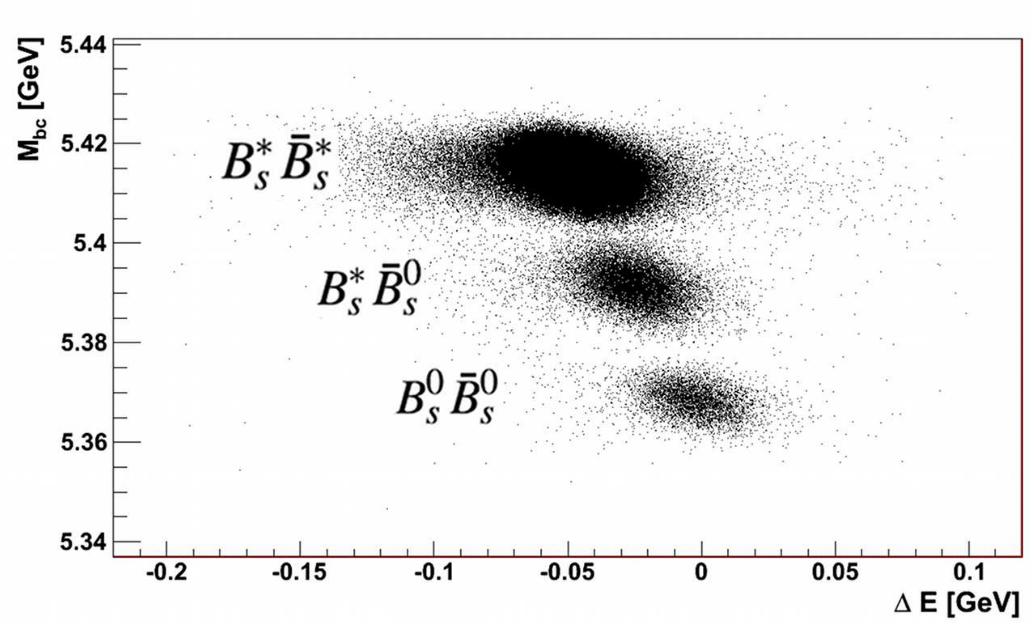

Figure 4.9: Scatter plot for the M_{bc} and the ΔE distribution obtained from $B_s^0 \rightarrow J/\psi\,\phi$ signal Monte Carlo simulated events.

only the most abundant production state $B_s^* \bar{B}_s^*$ is used in the following.

4.4.2 Continuum background

As explained in section 4.3.2 the continuum background can be distinguished from events with B meson decays with the event shape variable R_2 which is the ratio of the second to zeroth Fox-Wolfram moments. For this analysis only events with $R_2 < 0.4$ were taken into account for further investigation. This selection criterion was not optimized for the decay mode $B_s^0 \rightarrow J/\psi\, K^+K^-$ but for $B_s^0 \rightarrow J/\psi\, \pi^+\pi^-$ [63].

final selection criteria (see table 4.2)	e^+e^- channel	$\mu^+\mu^-$ channel
without tight M_{bc} and R_2 selection	476 ± 59	389 ± 53
including tight M_{bc} but without R_2 selection	95 ± 26	44 ± 18
including tight M_{bc} and R_2 selection	37 ± 16	15 ± 10

Table 4.3: The number of remaining events in the 15.509 fb^{-1} off-resonance data sample measured during the $\Upsilon(5S)$ experiments was scaled to match 121.4 fb^{-1}. Thus, the numbers indicate the expected amount of continuum background for this analysis in the full $\Upsilon(5S)$ data sample after the application of different selection criteria.

However, as both decays have the same decay topology, the optimized value for $B_s^0 \to J/\psi\,\pi^+\pi^-$ is also used for this analysis.
The final selection criteria as summarized in table 4.2 were applied on the so-called off-resonance data that was collected during the experiments 43, 67, 69 and 71 and corresponds to $15.509\,\mathrm{fb}^{-1}$. This off-resonance data sample was reduced to 7 events in total after introducing the selection on the ratio of the Fox-Wolfram moments. The obtained results on the off-resonance data were scaled to $121.4\,\mathrm{fb}^{-1}$ and presented in table 4.3. While the expected number of continuum events is thus too high to neglect this background source, the statistics are too low to allow a reliable determination of the shape of the continuum background, e.g. in the ΔE and the $M\left(K^+K^-\right)$ distributions. Therefore, the continuum background will be determined simultaneously with the combinatorial background.

4.5 The `ROOT` framework

The development of the object-oriented framework `ROOT` started about 20 years ago during the runtime of the NA 49 experiment at CERN. The parameters that are important for the further investigation of the decay $B_s^0 \to J/\psi\,K^+K^-$ are saved in the `ROOT` data format for all events passing the selection criteria summarized in section 4.4. The produced `ROOT` files are organized in a tree-like structure, similar to a `UNIX` file directory and the stored data can be accessed and edited either via a graphical user interface or through a software program written in `C++` where the `ROOT` library has to be included. The latter was the approach commonly used in this analysis, as it usually provides a much easier way to handle the data.
The `ROOT` framework is designed to meet the data analysis requirements of experiments in high energy physics. It uses the `C++` interpreter `CINT` to understand and execute single command lines or larger scripts written in pure `C++` code. This setup allows to process scripts that contain more than ten thousand lines of source code. Including the `ROOT` library into a `C++` script provides the user access to numerous features that are essential for physics analyses. This includes for example visualization of recorded data in form of graphs and histograms, a generator for random numbers, a geometry package and a linear algebra class that simplifies the work with matrices. The `ROOT` math libraries provide numerical constants, trigonometric functions as well as special functions relevant to calculations in physics, such as the bessel, gamma and error functions. Furthermore, `ROOT` provides the possibility to integrate user defined classes into the existing framework.

In order to evaluate the statistics of a given data sample, the `ROOT` developers implemented several statistical functions and probability density functions (PDFs) to determine the mean, standard deviation and shape of a given distribution. In the context of this analysis, the `RooFit` library was used for the development of the fitting procedure to extract the yields of the signal and the background components. This library includes numerous PDFs as well as functions for addition and convolution of PDFs. It also provides the option to build a multi-dimensional PDF model and perform a multi-dimensional fit to the data. The development and application of such a multi-dimensional fit to the analysis of the decay $B_s^0 \to J/\psi\, K^+K^-$ is presented in the next chapter.
More detailed information on the potential and the use of the `ROOT` framework and the `RooFit` library is given elsewhere [40, 41].

Chapter 5

Investigations on Monte Carlo simulated Data

The investigation of the decay $B_s^0 \to J/\psi K^+K^-$ is performed as a blind analysis. This means, that the complete procedure for the signal and background yield extraction has to be developed and tested on Monte Carlo (MC) simulated events. In order to extract the yields, a 2-dimensional unbinned maximum likelihood fit in ΔE and $M\left(K^+K^-\right)$ is performed separately for the $J/\psi \to e^+e^-$ and the $J/\psi \to \mu^+\mu^-$ channel and this fitting procedure is only applied to the real data sample, after it was proven to work correctly on the MC data.

The production of MC data has been illustrated in section 4.2 and this chapter is devoted to the development and test of the fitting procedure. It starts with the development of the fit, including a summary of the probability density functions (PDFs) that are suitable for this analysis. The second section describes the test of the fitting procedure on generic MC data, while the final PDF model that is used for the signal and background yield extraction on the real data is introduced in the last section.

5.1 Fitting Procedure development

The signal and background yield extraction is performed as a 2-dimensional unbinned maximum likelihood fit in the ΔE and $M\left(K^+K^-\right)$ distributions. The corresponding fit range is chosen to be -0.2 GeV $< \Delta E <$ 0.1 GeV, which is basically defined by the signal peak but also includes enough sideband to determine the background yield, and 0.95 GeV $< M\left(K^+K^-\right) <$ 2.4 GeV, which is the complete K^+K^- phase space and takes into account resolution effects at the lower end of the $M(K^+K^-)$ distribution. The development of this fit is performed in several steps. At first, suitable PDFs have to be found which are able to describe the shape of the investigated distributions. After the PDF parameters have been determined and fixed, the PDFs are combined to different models and every model is tested on the MC data in order to find the model which gives the best agreement with the MC truth. Finally, possible interference effects between the components in the PDF model have to be studied and included if necessary.

5.1.1 Suitable probability density functions

As explained in section 4.2.2 there are six streams of generic MC data available for this analysis and every stream contains the same luminosity as the real $\Upsilon\,(5S)$ data sample. Thus, five of the six streams are combined to determine the parameters of all PDFs that seem suitable to describe the shape of the ΔE and $M\,(K^+K^-)$ distributions, while the sixth stream is considered to simulate the real data sample and is used for the test of the fitting procedure (see section 5.1.3). This procedure is repeated six times, whereas each time a different MC stream is regarded as the simulated real data sample, which guarantees the independence of all performed tests and additionally provides six measurements of all PDF parameters.
Figure 5.1 presents the ΔE distribution for the $B_s^0 \to J/\psi\phi\,(1020)$ decay using five combined streams of generic MC, while stream number one is considered as simulated data sample and omitted during the determination of the PDF parameters. As the ΔE distribution only depends on the beam energy and the reconstructed energy of the B_s^0 (see equation 4.9) it is independent of the reconstructed decay mode, which means that the ΔE distribution has the same shape for all reconstructed signal components[1]. A Gaussian PDF

$$f\,(x;\mu,\sigma) = \frac{1}{\sigma\sqrt{2\pi}} e^{-\frac{(x-\mu)^2}{2\sigma^2}} \tag{5.1}$$

with mean μ and width σ is the obvious function to model the signal peak in ΔE in the $J/\psi \to \mu^+\mu^-$ channel. However, due to the bremsstrahlung tail that is present in the $J/\psi \to e^+e^-$ channel it is necessary to model this mode with a Crystal Ball function [64, 65]

[1] In this thesis, the term "signal component" refers to all three decays $B_s^0 \to J/\psi\phi\,(1020)$, $B_s^0 \to J/\psi f_2'\,(1525)$ and $B_s^0 \to J/\psi\,(K^+K^-)_{\text{other}}$, where $B_s^0 \to J/\psi\,(K^+K^-)_{\text{other}}$ includes the nonresonant decay $B_s^0 \to J/\psi K^+K^-$ and decays via other intermediate states, except the $\phi\,(1020)$ and the $f_2'\,(1525)$ resonances.

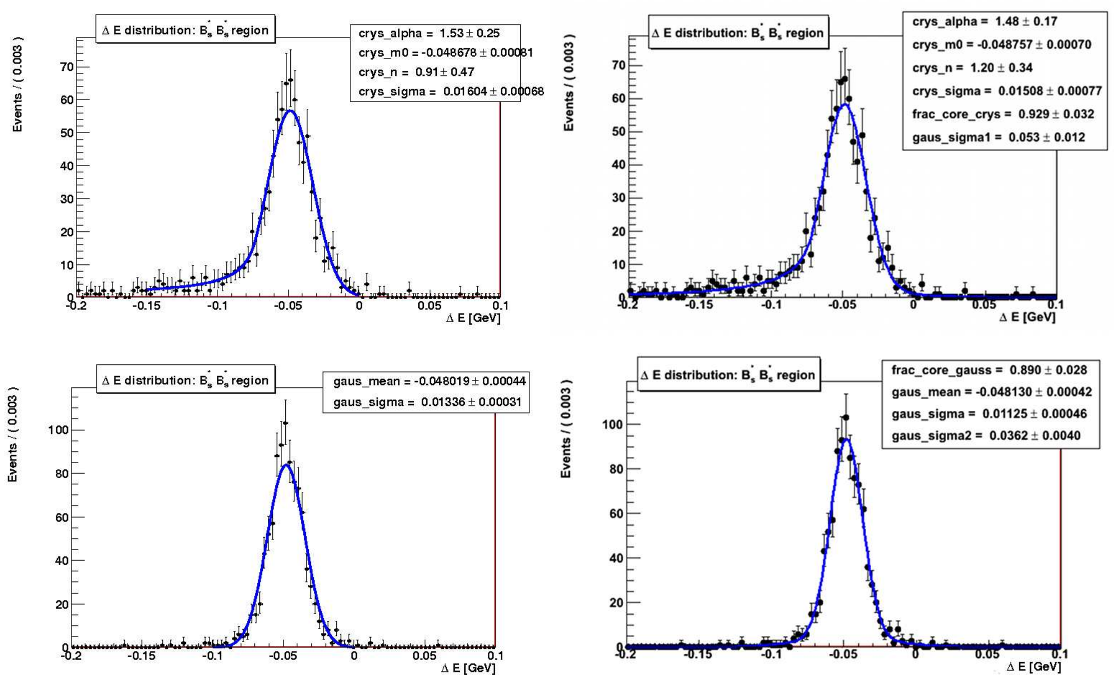

Figure 5.1: The ΔE distribution for the $B_s^0 \rightarrow J/\psi\phi(1020)$ decay in the $J/\psi \rightarrow e^+e^-$ channel (upper plots) was fitted with a Crystal Ball [64, 65] function (upper left plot) and a combination of Crystal Ball and Gaussian function (upper right plot), where the Crystal Ball and the Gaussian have a common mean but different widths. The corresponding ΔE distribution for the $J/\psi \rightarrow \mu^+\mu^-$ channel (lower plots) has been fitted with a single Gaussian (lower left plot) and a double Gaussian distribution (lower right plot) with common mean but different widths, respectively. The black dots with error bars are the simulated data points, while the fitted PDF is shown as blue solid line. The framed numbers are the fitted values of the respective PDF parameters.

$$f(x;\mu,\sigma,\alpha,n) \propto \begin{cases} e^{-\frac{(x-\mu)^2}{2\sigma^2}} & \text{for} \quad \frac{x-\mu}{\sigma} > -\alpha \\ \left(\frac{n}{\alpha}\right)^n e^{-\frac{\alpha^2}{2}} \left(\frac{n}{\alpha} - \alpha - \frac{x-\mu}{\sigma}\right)^{-n} & \text{for} \quad \frac{x-\mu}{\sigma} \leq -\alpha \end{cases} \tag{5.2}$$

with mean μ and width σ. The Crystal Ball PDF is a Gaussian distribution that changes into a power law at lower energies, where the threshold for the transition is given by the parameter α and n denotes the power. Thus, this description accommodates the bremsstrahlung losses. In figure 5.1 it is visible that it is not sufficient to model the ΔE distributions for the signal components with only a single Gaussian or Crystal Ball function, respectively. The use of a double Gaussian distribution and a combination of a Crystal Ball function with a Gaussian provides a considerably better agreement between the MC data and the fitted PDF. In this model, both Gaussian functions are required to have a common mean but different widths. The same restriction is applied to the Crystal Ball and the Gaussian PDF. As there are no reasonable alternative PDFs that give a better description of the signal peak in ΔE, these PDF combinations are chosen to model the ΔE distribution. The final PDF parameter values for the double Gaussian as well as the Crystal Ball and Gaussian function are determined from a real data control sample of the decay $B^0 \to J/\psi\ K^{*0}(892)$ (see section 5.1.2), which allows to adjust the values on a real data sample instead of using MC simulated events, without unblinding the signal

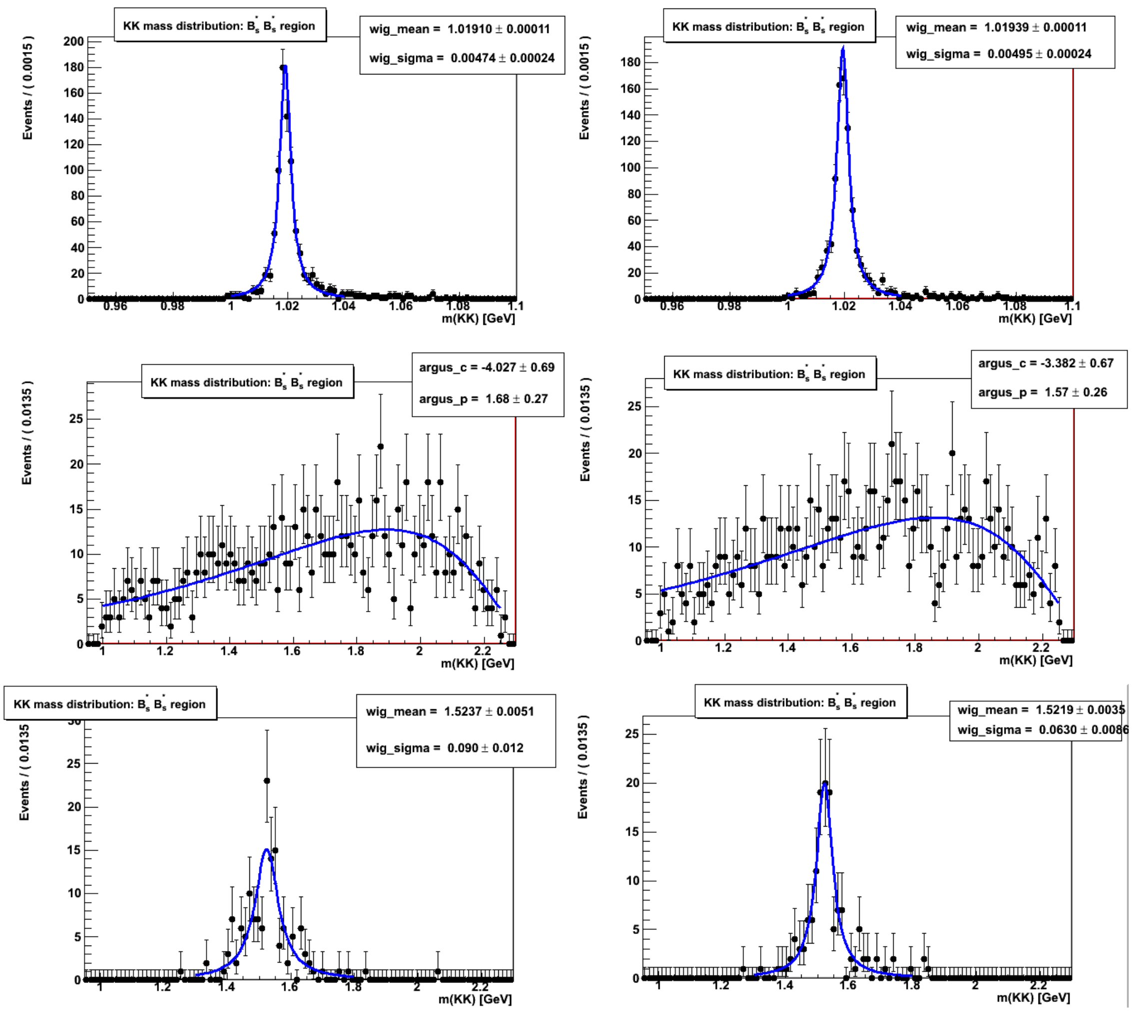

Figure 5.2: From top to bottom the plots show the $M(K^+K^-)$ distribution for the $B_s^0 \to J/\psi\phi(1020)$, $B_s^0 \to J/\psi(K^+K^-)_{\text{other}}$ and $B_s^0 \to J/\psi f_2'(1525)$ components separately for the $J/\psi \to e^+e^-$ (left plots) and $J/\psi \to \mu^+\mu^-$ channel (right plots). The black dots with the error bars represent the simulated data, while the blue solid line describes the PDF. In this figure, the ϕ and $f_2'(1525)$ resonances are modeled with a nonrelativistic Breit-Wigner function, while the $J/\psi(K^+K^-)_{\text{other}}$ is fitted with an ARGUS function [66].

region.
Figure 5.2 presents a sample of PDFs fitted to the $M(K^+K^-)$ distribution using again all generic MC streams except stream number one. The obvious PDF to describe the shape of a meson resonance is a Breit-Wigner function. Therefore, the first option to model the ϕ and the $f_2'(1525)$ resonances is a nonrelativistic Breit-Wigner PDF

$$f(x;\mu,\sigma) \propto \frac{1}{(x-\mu)^2 + \frac{1}{4}\sigma^2} \tag{5.3}$$

that is defined by its position μ and its width σ and which is found to be in good agreement with the data (see figure 5.2). Another possibility that does not add extra free parameters, is to complement the nonrelativistic Breit-Wigner with a phase space correction factor. A relativistic Breit-Wigner function that includes the spin of the corresponding meson is the third alternative PDF that is available for the description of the resonance peaks. Compared to the nonrelativistic Breit-Wigner, the width of the relativistic Breit-Wigner depends on the energy which is described by the Blatt-Weisskopf factors [9]. Just as the spin of the resonance is no free parameter, this factor is fixed, using an interaction radius of $3\,\mathrm{GeV}^{-1}$ [67]. Thus, there are no additional free parameters for the relativistic Breit-Wigner function. As all three versions of the Breit-Wigner PDF give a good description of the MC data, they are all investigated during the test of the fitting procedure to find the PDF that gives the best agreement with the MC truth with regard to the signal yield (see section 5.1.3).
A pure phase space description as well as an ARGUS function [66] are suitable to model the remaining $B_s^0 \to J/\psi\,(K^+K^-)_{\mathrm{other}}$ distribution in $M(K^+K^-)$. The ARGUS PDF

$$f(x;p,c,m_0) \propto x\left[1-\left(\frac{x}{m_0}\right)^2\right]^p e^{c\cdot\left[1-\left(\frac{x}{m_0}\right)^2\right]} \tag{5.4}$$

is defined by a fixed cut-off parameter $m_0 = 2.25\,\mathrm{GeV}$, a slope parameter c and a factor p which denotes the power of the function [68], while the phase space function has no free parameters. Both PDFs are studied during the test of the fitting procedure.
As presented in section 4.4.2, the number of continuum events is to low to investigate this background source separately. Therefore, the continuum background is determined simultaneously with the combinatorial background originating from randomly combined charged tracks. The distribution of the background events in ΔE and $M(K^+K^-)$ are obtained from a 100 MeV sideband in M_{bc} with $5.25\,\mathrm{GeV} \leq M_{bc} \leq 5.35\,\mathrm{GeV}$. The upper bound of this sideband is defined by the $B_s^0\bar{B}_s^0$ signal

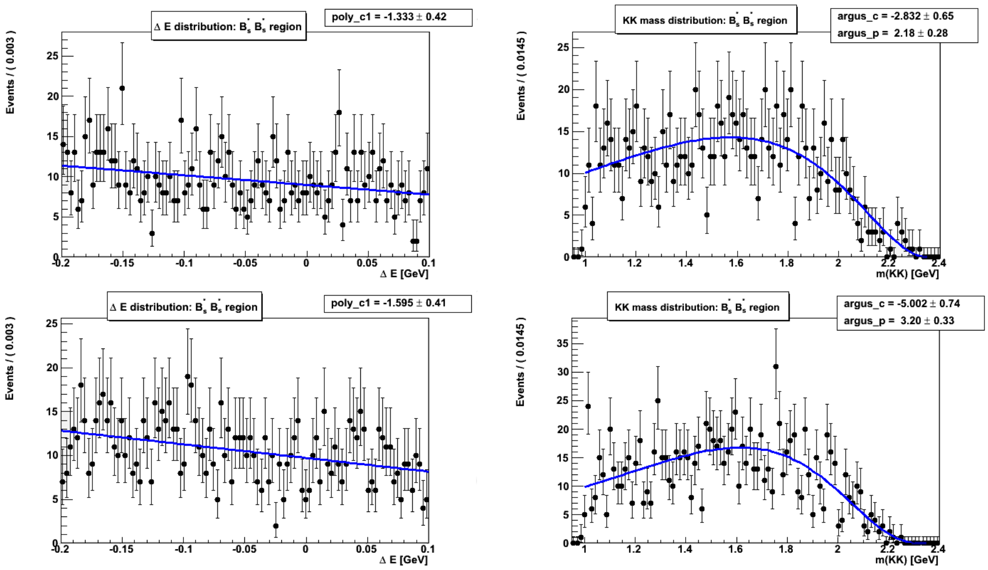

Figure 5.3: The ΔE and $M\left(K^{+}K^{-}\right)$ distributions for the combinatorial and continuum background are shown for the $J/\psi \rightarrow e^{+}e^{-}$ (upper plots) and the $J/\psi \rightarrow \mu^{+}\mu^{-}$ channel (lower plots). The simulated data is illustrated as black dots with error bars and is obtained from a sideband in M_{bc} with $5.25\,\mathrm{GeV} \leq M_{bc} \leq 5.35\,\mathrm{GeV}$. The fitted PDF function is presented as blue solid line. The applied PDFs are a first order polynomial in ΔE and the ARGUS function in $M\left(K^{+}K^{-}\right)$.

region which starts right above this threshold (see figure 4.9), while the lower bound prevents the integration of low energetic background which is not significant in the signal region. Again, this procedure has the advantage that the PDF parameters for the fit on the full $\Upsilon(5S)$ data sample can be determined from a real data sample (see section 5.1.2), instead of using the MC simulated events, without unblinding the signal region.

Figure 5.3 presents the ΔE and $M\left(K^{+}K^{-}\right)$ distributions for the background events that are obtained from the M_{bc} sideband in stream number one. A first order polynomial with a fixed ordinate value and a free slope and an ARGUS function with its cut-off parameter fixed at $m_0 = 2.35\,\mathrm{GeV}$ are found to be good descriptions of the ΔE and $M\left(K^{+}K^{-}\right)$ distributions, respectively.

5.1.2 Adjustment of PDF parameters on real data

Although it is possible to obtain all PDF parameter values from MC simulated events, the MC data is not a perfect description of the real data. Especially with regard to the resolution in the ΔE distribution, there might be differences in MC and real data. Thus, it is preferable to use real data samples for accurate determination of the PDF parameters, if possible.

A control data sample consisting of reconstructed events of the decay $B^0 \to J/\psi\, K^{*0}\,(892)$ with $K^{*0}\,(892) \to K^{\pm}\pi^{\mp}$ is used to obtain the PDF parameter values of the double Gaussian and the Crystal Ball and Gaussian PDF that describe the ΔE distribution. This investigation is performed on a real data sample that was collected at the energy of the $\Upsilon\,(4S)$ resonance and is based on the Belle official J/ψ skim, as well as on a MC simulated data sample which is based on the inclusive J/ψ MC data sample that was produced by the Belle collaboration in the year 2010 and mainly includes all known B decays with a J/ψ meson in the final state. The real data sample includes all experiments since experiment number 31 and its integrated luminosity adds up to $562.615\,\mathrm{fb}^{-1}$.

The decay mode $B^0 \to J/\psi\, K^{*0}\,(892)$ was chosen for the determination of the PDF parameters as it has a very similar final state as the decay $B_s^0 \to J/\psi K^+K^-$. The main difference between these two decays is that one kaon in the decay $B_s^0 \to J/\psi K^+K^-$ is replaced by a pion. Therefore, most of the selection criteria that are applied to reconstruct events in the $B_s^0 \to J/\psi K^+K^-$ mode are adopted for the reconstruction of $B^0 \to J/\psi\, K^{*0}\,(892)$ events. Table 5.1 summarizes all selection criteria that have to be changed with regard to the criteria listed in table 4.2. In order to identify a charged track as a pion and not as a kaon, it is required that the likelihood probability for the test of the pion against the kaon hypothesis is greater than 0.1. The $K^{*0}\,(892)$ meson has a nominal mass of $M\,(K^{*0}) = (895.81 \pm 0.19)$ MeV and a width of $\Gamma\,(K^{*0}) = (47.4 \pm 0.6)$ MeV [9]. Thus, only events that have a reconstructed invariant mass within $0.8\,\mathrm{GeV} \leq M\,(K\pi) \leq 1.0\,\mathrm{GeV}$ are taken into account for further investigation. The selected range in M_{bc} has to be adjusted, too, as the $\Upsilon\,(4S)$ data was recorded at a lower center-of-mass energy than the $\Upsilon\,(5S)$ events.

Figures 5.4 and 5.5 present the fitted ΔE distributions that were obtained from the real data and MC data control sample, respectively. All fits confirm a good agreement between the data and the applied PDFs. However, in order to verify that the

particle	selection criteria
$\pi^{\pm}$	pion likelihood ≥ 0.1
$K^{*0}\,(892)$	0.8 GeV $\leq M\,(K\pi) \leq 1.0$ GeV
B_s^0	$M_{bc} > 5.27$ GeV

Table 5.1: List of selection criteria that are applied to reconstruct the decay $\mathrm{B}^0 \to \mathrm{J}/\psi\ \mathrm{K}^{*0}\,(892)$. This table only summarizes the selection criteria that are different from the criteria listed in table 4.2.

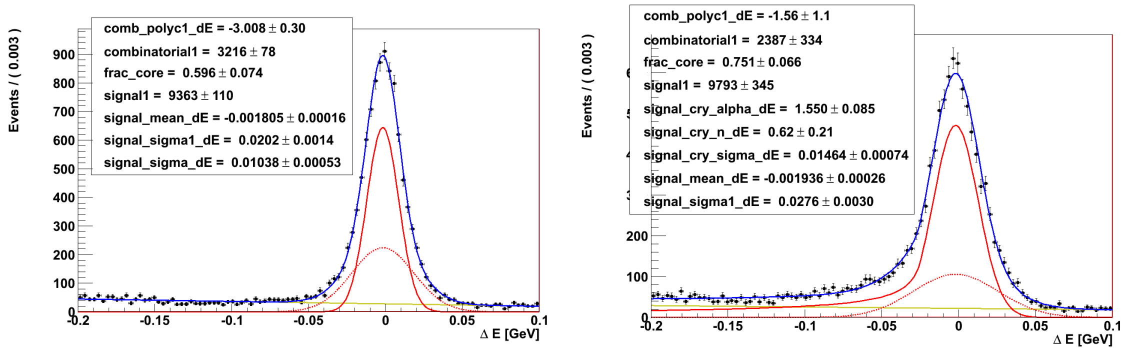

Figure 5.4: The ΔE distribution of the real data control sample is shown for the $J/\psi \to e^+e^-$ channel in the left plot, while the $J/\psi \to \mu^+\mu^-$ channel is illustrated on the right plot. The data is represented as black dots with error bars. The red solid lines indicate the Crystal Ball and Gaussian PDFs (left) and the two Gaussian functions (right), respectively, that were used to fit the data. The background component is fitted with a first order polynomial and shown as yellow solid line.

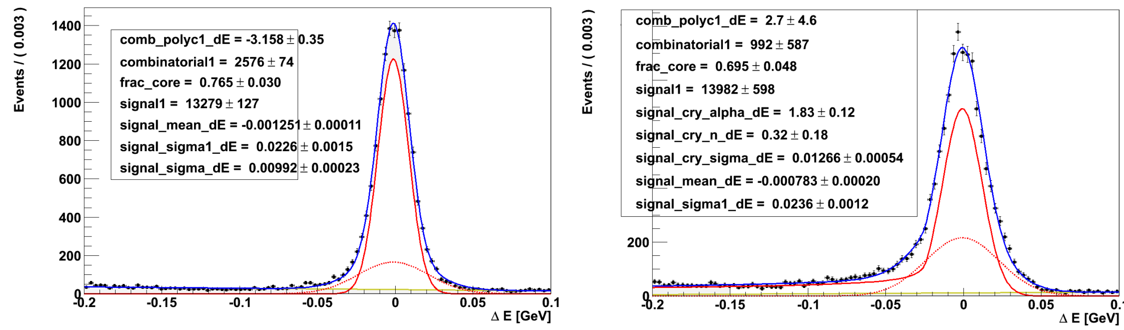

Figure 5.5: The ΔE distribution of the MC simulated control sample is shown for the $J/\psi \to e^+e^-$ channel in the left plot, while the $J/\psi \to \mu^+\mu^-$ channel is illustrated on the right plot. The data is represented as black dots with error bars. The red solid lines indicate the Crystal Ball and Gaussian PDFs (left) and the two Gaussian functions (right), respectively, that were used to fit the data. The background component is fitted with a first order polynomial and shown as yellow solid line.

parameters that were determined from the $B^0 \to J/\psi\, K^{*0}\,(892)$ control sample are sufficient to describe the ΔE distribution of the decay $B_s^0 \to J/\psi K^+K^-$ correctly, this parametrization is used for the test of the fitting procedure that is introduced in section 5.1.3.

Besides the ΔE distribution of the signal components, it is also possible to determine the PDF parameter values for the background component on a real data sample, as mentioned in the previous section. Figure 5.6 present the ΔE and $M\,(K^+K^-)$ distributions in the sideband region for $5.25\,\text{GeV} \leq M_{bc} \leq 5.35\,\text{GeV}$ that were obtained

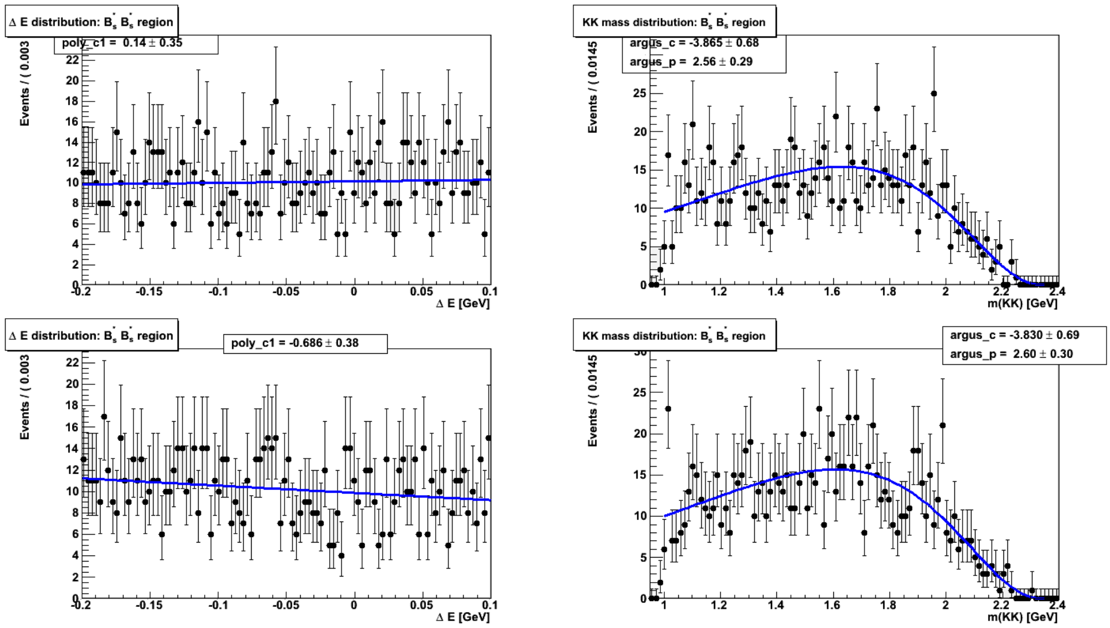

Figure 5.6: The ΔE and $M\left(K^+K^-\right)$ distributions for the background component are shown for the $J/\psi \to e^+e^-$ (upper plots) and the $J/\psi \to \mu^+\mu^-$ channel (lower plots). The data is illustrated as black dots with error bars and is obtained from a sideband in M_{bc} with $5.25\,\mathrm{GeV} \le M_{bc} \le 5.35\,\mathrm{GeV}$. The fitted PDF function is presented as blue solid line.

from the full $\Upsilon(5S)$ data sample after the application of the event reconstruction for the $B_s^0 \to J/\psi K^+K^-$ decay. The ΔE distribution is again described with a first order polynomial with fixed ordinate value and free slope, while the $M\left(K^+K^-\right)$ distribution is modeled with an ARGUS function. In both cases, the fit shows a good agreement with the data.

5.1.3 Test of the fitting procedure

The test of the fitting procedure is performed as realistic as possible in order to obtain reliable results on the quality of the different PDF models. Thus, the fit is always performed on only one MC stream, so that the yields of the signal and background components are comparable with the statistics in the full $\Upsilon(5S)$ data sample.

The parametrization of the double Gaussian and the Crystal Ball and Gaussian PDFs, respectively, is preserved from the MC control sample as introduced in the previous section. All signal components are described with the same PDF parametrization in ΔE, as the energy difference only depends on the beam energy and the energy

of the reconstructed B_s^0 meson, which is independent of the decay mode. In order to avoid any shift between the data and the fitted PDF in ΔE, the mean of the double Gaussian PDF as well as the mean of the Crystal Ball and Gaussian function is not fixed to a certain value, but treated as a free parameter.
While one MC stream is considered as simulated data sample, the PDF parameters for the description of the signal components in the $M\left(K^+K^-\right)$ distribution are determined from the remaining five MC streams. The PDF parameters modeling the background component are obtained from a fit of the M_{bc} sideband in the region $5.25\,\mathrm{GeV} \leq M_{bc} \leq 5.35\,\mathrm{GeV}$ as presented in section 5.1.1.
All fits presented in this section are separately performed for the $J/\psi \rightarrow e^+e^-$ and the $J/\psi \rightarrow \mu^+\mu^-$ channel as 2-dimensional unbinned likelihood fits to the ΔE and $M\left(K^+K^-\right)$ distribution. Every fit was executed with a different PDF model and different PDF parameters. The fitted yields for the signal and background components are compared with the expected number of events which is obtained from the generator information stored in the MC data files. All fit results are presented in tables 5.3 to 5.6, which are located at the end of this chapter. Tables 5.3 and 5.4 summarize the results for the fits in the $J/\psi \rightarrow e^+e^-$ channel where the $J/\psi\left(K^+K^-\right)_{\mathrm{other}}$ component is modeled with an ARGUS function and a pure phase space description, respectively. Tables 5.5 and 5.6 provide the same information for the $J/\psi \rightarrow \mu^+\mu^-$ channel. The acronyms in the first column of each table refer the respective Breit-Wigner function that was used for the fit:

- *nonrel* : nonrelativistic Breit-Wigner PDF
- *rel* : relativistic Breit-Wigner PDF that includes the spin of the resonance
- *phsp* : nonrelativistic Breit-Wigner PDF with an applied phase space correction

Thus, the description "*nonrel-rel*" states that the $\phi\,(1020)$ resonance is fitted with the nonrelativistic Breit-Wigner function, while the $f_2'\,(1525)$ resonance is modeled with the relativistic Breit-Wigner PDF. This kind of labeling applies to all other combinations of Breit-Wigner models, too.
Basically, all fitted yields for the signal and background components are in good agreement with the expected yields obtained from the MC generator. No significant differences were observed between the fit results obtained with a pure phase space description of the $J/\psi\left(K^+K^-\right)_{\mathrm{other}}$ component and the results yielded by the ARGUS function. The same conclusion is drawn for the nonrelativistic Breit-Wigner PDF and the Breit-Wigner function including the phase space correction. The only exception where the fitted yields are not in agreement with the expectations are

the fits, in which the $\phi\,(1020)$ resonance is modeled with a relativistic Breit-Wigner function. In these cases the results present a significant bias for the $J/\psi\,\phi$ and the $J/\psi\,(K^+K^-)_{\text{other}}$ components. The description of the $f_2'\,(1525)$ resonance with a relativistic Breit-Wigner does not seem to lead to the same bias, however, it might not be visible here, as the statistics for the decay $B_s^0 \to J/\psi\; f_2'\,(1525)$ is much lower than the statistics for $B_s^0 \to J/\psi\,\phi\,(1020)$. Due to this bias, the relativistic Breit-Wigner function is ruled out as a possible PDF for the fit on the full $\Upsilon\,(5S)$ data sample, while all remaining PDFs are equally capable of extracting the signal and background yields.

5.1.4 Bias originating from relativistic Breit-Wigner function

The test of the fitting procedure introduced in the previous section has revealed a bias for all fits, where the $\phi\,(1020)$ resonance is modeled with a relativistic Breit-Wigner function. This bias causes a systematic overestimation of the number of $B_s^0 \to J/\psi\phi\,(1020)$ decays, while the number of $B_s^0 \to J/\psi\,(K^+K^-)_{\text{other}}$ events is systematically underestimated (see tables 5.3 to 5.6).

In order to better understand the reason for this bias, two different fits were performed on the $J/\psi \to \mu^+\mu^-$ channel of stream number zero. As both fits are 1-dimensional unbinned likelihood fits only modeling the $M\,(K^+K^-)$ distribution, any effects from bremsstrahlung photons are excluded and no further difference between the electron and the muon channel is expected that might influence the fit results.

The first fit is performed only on correctly reconstructed $B_s^0 \to J/\psi\phi\,(1020)$ decays, which were selected with the information from the MC generator. The fit result is shown in figure 5.7. The $\phi\,(1020)$ resonance was described with a relativistic Breit-Wigner and the fitted yield for the $J/\psi\phi\,(1020)$ component is in perfect agreement with the expected number of 201 events. Thus, the bias is certainly not produced by a wrong implementation or application of the relativistic Breit-Wigner PDF.

In the second fit, the other two signal components ($J/\psi\,(K^+K^-)_{other}$ and $J/\psi f_2'\,(1525)$) are added, while all events from the combinatorial and continuum background are still omitted. From the MC generator information, the expected number of events for this data sample is determined to be 201 events for the $B_s^0 \to J/\psi\phi\,(1020)$ decay, 194 events for the $J/\psi\,(K^+K^-)_{other}$ component and 29 events for the decay $B_s^0 \to J/\psi f_2'\,(1525)$. The fitted distribution and the fitted signal yields are presented in figure 5.8 and the same bias was found that already has been observed during the test of the fitting procedure. Again, the yield of the $J/\psi\phi\,(1020)$ component is strongly overestimated, while the fitted yield of the $J/\psi\,(K^+K^-)_{other}$

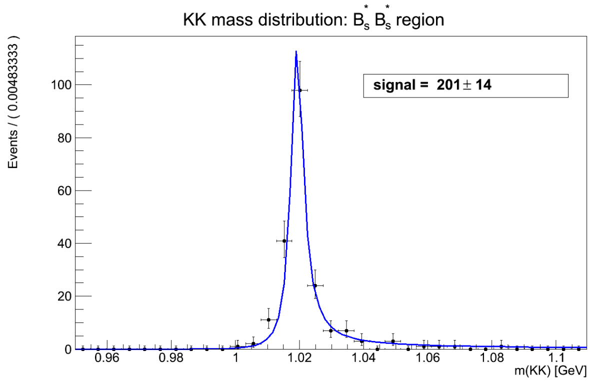

Figure 5.7: Correctly reconstructed events from the decay $B_s^0 \rightarrow J/\psi\phi\,(1020)$ were selected from the $J/\psi \rightarrow \mu^+\mu^-$ channel in MC stream number zero with the information from the MC generator. The MC data is illustrated as black dots with error bars, while the solid blue line presents the fitted PDF. The $\phi\,(1020)$ resonance was described with a relativistic Breit-Wigner function and the fit result is in perfect agreement with the expectations.

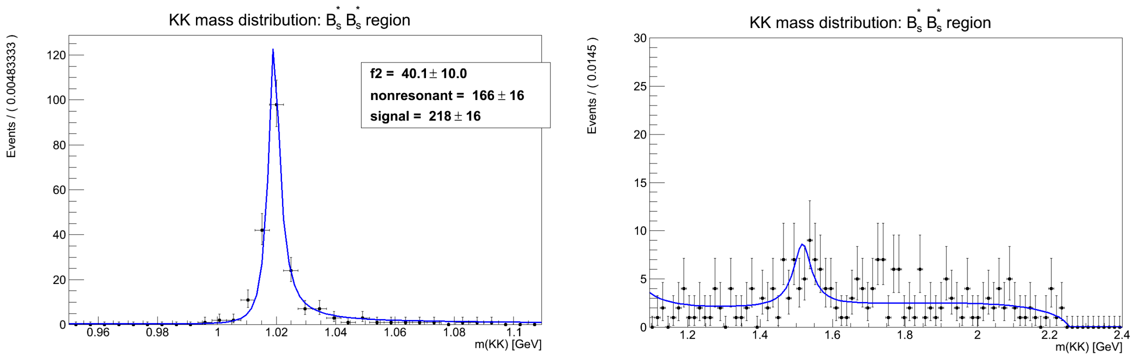

Figure 5.8: Correctly reconstructed events from all signal components were selected from the $J/\psi \rightarrow \mu^+\mu^-$ channel in MC stream number zero with the information from the MC generator. The background component is omitted. The MC data is illustrated as black dots with error bars, while the solid blue line presents the fitted PDF. The $\phi\,(1020)$ resonance was modeled with a relativistic Breit-Wigner function and the fit results show a significant bias. To provide a better overview, the whole $M\,(K^+K^-)$ distribution is separated in two energy regions.

component drops far below the expectation. As the background component is not present in this fit, it can be ruled out as a possible reason for the bias.

The main difference between the two fits is given by the additional signal components which are present in the second fit. This expands the $M\,(K^+K^-)$ distribution and thus the fit range from $0.95\,\text{GeV} \leq M\,(K^+K^-) \leq 1.1\,\text{GeV}$ to the full K^+K^- phase space with $0.95\,\text{GeV} \leq M\,(K^+K^-) \leq 2.4\,\text{GeV}$. Therefore, the bias in the

	$J/\psi \to e^+e^-$ channel	$J/\psi \to \mu^+\mu^-$ channel
ΔE distribution:		
all signal components	Crystal Ball + Gaussian	double Gaussian
background	1st order polynomial	1st order polynomial
$M\,(K^+K^-)$ distribution:		
$J/\psi\,\phi\,(1020)$	nonrel. Breit-Wigner	nonrel. Breit-Wigner
$J/\psi\,(K^+K^-)_{\text{other}}$	ARGUS	ARGUS
$J/\psi\,f_2'\,(1525)$	nonrel. Breit-WIgner	nonrel. Breit-Wigner
background	ARGUS	ARGUS

Table 5.2: The composition of the default PDF model that is used for the fit on the full $\Upsilon\,(5S)$ data sample is presented separately for the $J/\psi \to e^+e^-$ channel and $J/\psi \to \mu^+\mu^-$ channel.

fit results has to be caused by the high energy tail of the relativistic Breit-Wigner that is much more dominant than the tail of the nonrelativistic Breit-Wigner. If the fit is performed on the full $M\,(K^+K^-)$ distribution, the high energy tail of the relativistic Breit-Wigner assigns additional events to the $J/\psi\phi\,(1020)$ component which leads the fit into a wrong minimum and causes the underestimation of the rather flat $J/\psi\,(K^+K^-)_{other}$ distribution. On the other hand, this effect is negligible if the $M\,(K^+K^-)$ distribution breaks off at low energies. However, as it is necessary to perform a fit on the full $M\,(K^+K^-)$ distribution in this analysis, the relativistic Breit-Wigner function is no possible option for the fit on the real $\Upsilon\,(5S)$ data sample.

5.2 Final PDF model

The selection of the PDF model that is applied on the full $\Upsilon\,(5S)$ data sample is based on the results obtained from the test of the fitting procedure. As all PDFs, except the relativistic Breit-Wigner function, provided results in good agreement with the expectations and no significant biases in the obtained signal yields were found, it was decided to use the simple PDF model that is summarized in table 5.2 as the default fit model, while the remaining PDFs that are not included in this default model are taken into account as systematic error (see section 6.2).
The default PDF model describes the shape of the ΔE distribution for the signal components with a combination of a Crystal Ball and a Gaussian function in the $J/\psi \to e^+e^-$ channel and with a double Gaussian PDF in the $J/\psi \to \mu^+\mu^-$ channel, respectively. The parameter values for these PDFs which will be used for the fit

on the $\Upsilon\,(5S)$ data were determined with the $B^0 \to J/\psi\, K^{*0}\,(892)$ real data control sample. The $\phi\,(1020)$ and the $f_2'\,(1525)$ resonances are modeled with a nonrelativistic Breit-Wigner PDF, while the shape of the $J/\psi\,(K^+K^-)_{\text{other}}$ component is fitted with an ARGUS function. As the PDF parameters of the Breit-Wigner and the ARGUS functions are measured six times (see section 5.1.1), their parametrization is defined by the weighted mean value of all six measurements. The ΔE distribution of the background component is described with a first order polynomial and the $M\,(K^+K^-)$ distribution with an ARGUS function. The parameter values for the background component are obtained from the M_{bc} sideband of the $\Upsilon\,(5S)$ data sample with $5.25\,\text{GeV} \leq M_{bc} \leq 5.35\,\text{GeV}$.
This default PDF model has demonstrated a good agreement between the fitted yields and the expected number of events during the test on the generic MC data. However, it does not take into account interference effects. As all of the signal components have distinct quantum numbers (spin $J = 0$ for $B_s^0 \to J/\psi\,(K^+K^-)_{\text{other}}$ (S-wave component), $J = 1$ for $B_s^0 \to J/\psi\phi\,(1020)$ (P-wave component) and $J = 2$ for $B_s^0 \to J/\psi f_2'\,(1525)$ (D-wave component)) the effects of possible interference between these states is expected to be negligible. However, all interference effects will exactly cancel out, if the reconstruction efficiency depending on the helicity angles ϕ and ψ provides a flat distribution [6,69]. These helicity angles are defined as follows:

- ϕ is the angle between the K^+K^- and $\ell^+\ell^-$ plane
- ψ is the angle between the J/ψ and K^+ momentum

The reconstruction efficiency for these two angles is presented in figures 5.9 and 5.10 (obtained from the combined data of all six generic MC streams). These distributions are fitted with a constant function and the resulting χ^2/ndf values show, that the efficiency is in agreement with this assumption. Thus, due to the flat reconstruction efficiency, it is not necessary to perform any further investigations on interference effects and they are not taken into account for the default PDF model.

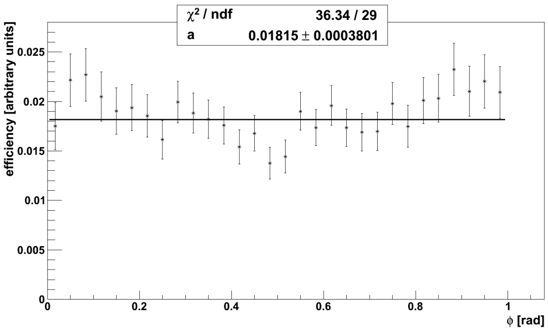

Figure 5.9: The reconstruction efficiency depending on the helicity angle ϕ is shown for the $J/\psi \to \mu^+\mu^-$ channel (left plot) and the $J/\psi \to e^+e^-$ channel (right plot). The data is illustrated as black dots with error bars and is fitted with a constant function (black solid line).

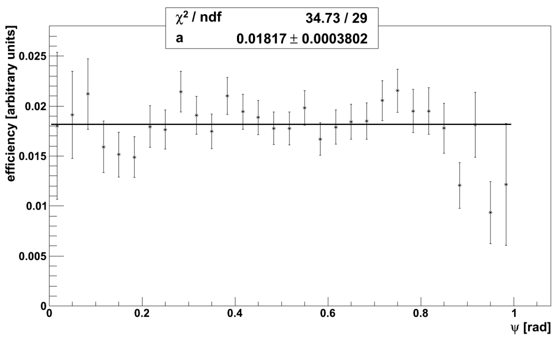

Figure 5.10: The reconstruction efficiency depending on the helicity angle ψ is shown for the $J/\psi \to \mu^+\mu^-$ channel (left plot) and the $J/\psi \to e^+e^-$ channel (right plot). The data is illustrated as black dots with error bars and is fitted with a constant function (black solid line).

$J/\psi \to e^+e^-$ channel	$J/\psi\,\phi\,(1020)$	$J/\psi\,(K^+K^-)_{\mathrm{other}}$	$J/\psi\ f_2'\,(1525)$	background
s00 MC truth	185	178	34	276
nonrel - nonrel	181.8±14.1	199.7±20.7	37.7±11.9	252.8±20.3
rel - rel	207.9±15.6	176.1±20.7	40.0±12.8	248.0±20.0
phsp - rel	188.4±14.5	193.1±21.0	37.9±12.5	252.5±20.2
phsp - nonrel	188.3±14.5	194.6±20.6	37.3±12.0	251.8±20.2
nonrel - rel	182.0±14.1	199.1±21.1	37.3±12.3	253.6±20.3
rel - nonrel	207.5±15.6	179.6±20.2	37.3±12.0	247.5±20.0
s01 MC truth	153	170	27	282
nonrel - nonrel	157.9±13.0	168.3±20.1	32.7±11.6	273.1±20.9
rel - rel	179.8±14.6	150.1±20.0	35.2±12.1	266.8±20.8
phsp - rel	162.9±13.4	163.4±20.3	33.7±12.0	271.9±20.9
phsp - nonrel	162.7±13.4	164.6±20.0	32.9±11.6	271.7±20.9
nonrel - rel	158.1±13.0	167.5±20.4	33.1±11.9	273.3±21.0
rel - nonrel	179.3±14.5	152.9±19.7	33.0±11.5	266.8±20.7
s02 MC truth	157	173	26	273
nonrel - nonrel	155.8±13.0	209.1±21.0	28.6±11.3	235.5±20.0
rel - rel	172.6±14.2	194.0±21.2	30.8±11.9	231.6±19.9
phsp - rel	159.8±13.3	204.5±21.2	30.7±11.8	233.9±20.0
phsp - nonrel	159.8±13.3	206.5±21.1	28.1±11.3	234.5±20.0
nonrel - rel	156.0±13.0	207.4±21.2	31.0±11.7	234.6±20.0
rel - nonrel	172.5±14.2	196.9±20.9	27.6±11.3	232.0±19.9
s03 MC truth	183	156	27	258
nonrel - nonrel	181.7±13.9	156.1±19.2	31.7±11.0	254.6±20.3
rel - rel	204.6±15.3	135.1±19.0	39.4±12.1	245.0±19.9
phsp - rel	187.4±14.3	146.5±19.4	38.4±11.9	251.7±20.2
phsp - nonrel	187.2±14.3	152.9±19.1	31.5±11.0	252.4±20.2
nonrel - rel	182.0±14.0	150.2±19.4	38.2±11.8	253.6±20.2
rel - nonrel	204.3±15.3	142.7±18.7	31.2±10.9	245.9±20.0
s04 MC truth	184	167	30	261
nonrel - nonrel	185.4±14.1	180.8±20.4	26.7±11.1	249.1±20.5
rel - rel	208.5±15.5	161.0±20.5	30.6±11.9	241.9±20.2
phsp - rel	191.0±14.4	174.1±20.7	29.4±11.8	247.6±20.4
phsp - nonrel	190.8±14.4	177.0±20.4	26.9±11.1	247.3±20.4
nonrel - rel	185.6±14.1	178.3±20.8	28.8±11.7	249.3±20.5
rel - nonrel	208.1±15.5	165.3±20.0	26.9±11.0	241.8±20.2
s05 MC truth	170	168	26	290
nonrel - nonrel	168.9±13.4	153.6±19.3	31.6±10.8	298.9±21.5
rel - rel	189.5±14.8	139.1±19.4	31.9±11.6	292.5±21.3
phsp - rel	173.8±13.8	149.3±19.6	31.9±11.5	298.1±21.5
phsp - nonrel	173.8±13.8	151.4±19.3	30.1±11.0	297.6±21.4
nonrel - rel	169.0±13.4	152.6±19.6	32.1±11.3	299.3±21.5
rel - nonrel	189.4±14.8	142.1±19.0	29.0±10.9	292.4±21.3

Table 5.3: The results for the test of the fitting procedure are shown for the $J/\psi \to e^+e^-$ channel. The $J/\psi\,(K^+K^-)_{\mathrm{other}}$ component is modeled with an ARGUS function. The labeling of the different PDF models is described in the text in section 5.1.3.

$J/\psi \to e^+e^-$ channel	$J/\psi\,\phi\,(1020)$	$J/\psi\,(K^+K^-)_{\text{other}}$	$J/\psi\ f_2'\,(1525)$	background
s00 MC truth	185	178	34	276
nonrel - nonrel	183.7±14.1	210.0±21.3	28.4±11.7	249.9±20.2
rel - rel	208.7±15.5	186.4±21.5	31.2±12.9	245.7±20.0
phsp - rel	190.0±14.5	203.8±21.7	28.9±12.5	249.3±20.2
phsp - nonrel	190.0±14.5	205.3±21.3	27.7±11.9	248.9±20.2
nonrel - rel	183.8±14.1	209.4±21.7	28.5±12.1	250.3±20.3
rel - nonrel	208.5±15.5	189.8±21.0	28.3±12.0	245.4±20.0
s01 MC truth	153	170	27	282
nonrel - nonrel	158.8±13.0	184.6±21.1	21.8±11.4	266.8±20.8
rel - rel	179.6±14.5	164.9±21.2	25.7±12.2	261.8±20.7
phsp - rel	163.6±13.4	179.4±21.4	23.5±12.0	265.4±20.8
phsp - nonrel	163.4±13.4	180.7±21.0	22.3±11.4	265.5±20.8
nonrel - rel	158.9±13.0	183.7±21.4	22.7±12.0	266.6±20.8
rel - nonrel	179.2±14.5	167.6±20.8	23.3±11.4	261.9±20.7
s02 MC truth	157	173	26	273
nonrel - nonrel	157.9±13.0	222.9±21.7	18.3±11.1	230.0±19.9
rel - rel	173.5±14.2	206.7±22.0	20.3±11.8	228.5±19.9
phsp - rel	161.6±13.3	218.4±22.0	19.7±11.6	229.3±19.9
phsp - nonrel	161.6±13.3	220.0±21.8	18.0±11.1	229.4±19.9
nonrel - rel	158.0±13.0	221.4±21.9	19.9±11.4	229.6±19.9
rel - nonrel	173.4±14.2	209.0±21.7	18.1±11.1	228.5±19.9
s03 MC truth	183	156	27	258
nonrel - nonrel	182.7±13.9	171.0±20.1	22.2±10.9	248.0±20.2
rel - rel	204.5±15.3	149.4±20.1	30.2±12.1	239.9±19.9
phsp - rel	188.1±14.3	161.4±20.4	28.8±11.9	245.7±20.1
phsp - nonrel	188.0±14.3	167.8±20.1	22.2±10.9	246.0±20.1
nonrel - rel	182.9±14.0	165.0±20.4	28.6±11.8	247.5±20.2
rel - nonrel	204.3±15.3	157.1±19.8	22.4±10.9	240.3±19.9
s04 MC truth	184	167	30	261
nonrel - nonrel	186.6±14.1	196.9±21.3	15.4±10.8	243.2±20.3
rel - rel	208.0±15.4	177.2±21.6	19.1±11.9	237.8±20.1
phsp - rel	191.7±14.4	191.3±21.8	17.1±11.7	241.9±20.3
phsp - nonrel	191.6±14.4	192.8±21.2	15.9±10.8	241.7±20.3
nonrel - rel	186.7±14.1	195.7±21.8	16.2±11.6	243.5±20.3
rel - nonrel	207.7±15.4	180.0±21.0	16.8±10.8	237.5±20.1
s05 MC truth	170	168	26	290
nonrel - nonrel	169.9±13.4	170.0±20.2	22.3±10.4	290.8±21.4
rel - rel	189.4±14.7	155.7±20.7	22.0±11.6	285.9±21.3
phsp - rel	174.6±13.7	166.7±20.7	21.6±11.3	290.0±21.4
phsp - nonrel	174.7±13.7	168.2±20.4	20.4±10.8	289.7±21.4
nonrel - rel	170.0±13.4	169.5±20.6	22.4±10.9	291.2±21.4
rel - nonrel	189.4±14.7	158.2±20.2	19.7±10.8	285.6±21.3

Table 5.4: The results for the test of the fitting procedure are shown for the $J/\psi \to e^+e^-$ channel. The $J/\psi\,(K^+K^-)_{\text{other}}$ component is modeled with a phase space function. The labeling of the different PDF models is described in the text in section 5.1.3.

$J/\psi \to \mu^+\mu^-$ channel	$J/\psi\,\phi\,(1020)$	$J/\psi\,(K^+K^-)_{\text{other}}$	$J/\psi\,f_2'\,(1525)$	background
s00 MC truth	201	194	29	288
nonrel - nonrel	198.3±14.5	187.4±18.3	37.6±10.5	288.8±19.2
rel - rel	218.9±15.8	165.3±18.3	41.3±11.1	286.5±19.1
phsp - rel	203.3±14.8	180.2±18.4	40.3±11.0	288.2±19.2
phsp - nonrel	203.0±14.8	182.9±18.3	37.9±10.5	288.3±19.2
nonrel - rel	198.5±14.5	185.1±18.5	39.7±11.0	288.8±19.2
rel - nonrel	218.2±15.7	169.2±18.0	37.9±10.5	286.7±19.1
s01 MC truth	183	200	29	308
nonrel - nonrel	187.7±14.2	198.7±18.4	26.9±9.6	306.7±19.6
rel - rel	211.5±15.6	174.9±18.1	30.2±10.0	303.4±19.5
phsp - rel	193.6±14.5	191.2±18.4	29.1±9.9	306.1±19.6
phsp - nonrel	193.3±14.5	193.3±18.3	27.4±9.6	306.0±19.6
nonrel - rel	187.9±14.2	196.9±18.5	28.5±9.8	306.8±19.6
rel - nonrel	211.0±15.5	178.0±18.0	27.6±9.6	303.3±19.5
s02 MC truth	205	195	25	308
nonrel - nonrel	199.9±14.6	207.0±18.2	17.4±8.3	308.7±19.6
rel - rel	221.4±15.9	188.5±18.2	17.7±8.8	305.4±19.5
phsp - rel	205.2±14.9	202.0±18.3	17.9±8.7	307.9±19.5
phsp - nonrel	205.4±14.9	204.0±18.3	15.6±8.4	307.9±19.5
nonrel - rel	199.8±14.6	205.4±18.2	19.1±8.5	308.6±19.6
rel - nonrel	221.4±15.9	190.8±18.1	15.3±8.4	305.5±19.5
s03 MC truth	179	187	29	277
nonrel - nonrel	172.2±13.6	184.3±18.3	28.8±9.5	286.6±19.3
rel - rel	194.4±15.0	162.2±18.1	30.5±9.7	284.7±19.2
phsp - rel	177.3±13.9	179.1±18.3	29.1±9.6	286.4±19.2
phsp - nonrel	177.1±13.9	179.3±18.2	29.2±9.6	286.2±19.2
nonrel - rel	172.3±13.6	184.3±18.3	28.6±9.6	286.8±19.3
rel - nonrel	194.1±15.0	163.3±18.0	29.9±9.5	284.7±19.2
s04 MC truth	179	180	30	316
nonrel - nonrel	171.5±13.6	192.6±17.9	32.7±9.4	308.1±19.6
rel - rel	190.8±14.8	174.7±17.9	34.0±9.8	305.5±19.6
phsp - rel	176.3±13.9	187.3±18.0	33.7±9.8	307.6±19.6
phsp - nonrel	176.4±13.9	189.4±17.9	31.7±9.5	307.5±19.6
nonrel - rel	171.6±13.5	191.0±18.0	34.1±9.7	308.3±19.6
rel - nonrel	190.6±14.8	177.5±17.8	31.3±9.4	305.5±19.6
s05 MC truth	185	159	25	275
nonrel - nonrel	189.0±14.1	134.5±15.9	52.2±10.4	268.3±18.4
rel - rel	214.1±15.6	111.1±15.7	54.1±10.8	264.7±18.2
phsp - rel	195.2±14.5	123.0±16.0	53.4±10.7	267.4±18.3
phsp - nonrel	195.4±14.5	130.3±15.9	50.8±10.5	267.4±18.3
nonrel - rel	189.1±14.1	133.0±16.0	53.7±10.6	268.1±18.4
rel - nonrel	213.9±15.6	115.4±15.5	49.9±10.4	264.8±18.2

Table 5.5: The results for the test of the fitting procedure are shown for the $J/\psi \to \mu^+\mu^-$ channel. The $J/\psi\,(K^+K^-)_{\text{other}}$ component is modeled with an ARGUS function. The labeling of the different PDF models is described in the text in section 5.1.3.

$J/\psi \to \mu^+\mu^-$ channel	$J/\psi\,\phi\,(1020)$	$J/\psi\,(K^+K^-)_{\text{other}}$	$J/\psi\,f_2'\,(1525)$	background
s00 MC truth	201	194	29	288
nonrel - nonrel	200.7±14.5	193.7±18.6	30.6±10.4	287.0±19.1
rel - rel	220.5±15.7	171.6±18.5	34.8±11.1	285.2±19.0
phsp - rel	205.5±14.8	186.8±18.7	33.3±10.9	286.4±19.1
phsp - nonrel	205.3±14.8	189.2±18.5	31.0±10.4	286.5±19.1
nonrel - rel	200.8±14.5	191.7±18.7	32.6±10.9	286.9±19.1
rel - nonrel	220.0±15.7	175.0±18.3	31.6±10.4	285.5±19.0
s01 MC truth	183	200	29	308
nonrel - nonrel	190.2±14.2	203.4±18.6	21.1±9.5	305.2±19.6
rel - rel	213.3±15.5	180.0±18.3	24.9±9.9	301.8±19.4
phsp - rel	195.9±14.5	196.1±18.6	23.5±9.8	304.5±19.5
phsp - nonrel	195.8±14.5	198.2±18.5	21.6±9.5	304.4±19.5
nonrel - rel	190.4±14.2	201.5±18.7	22.7±9.7	305.3±19.6
rel - nonrel	213.0±15.5	182.9±18.2	22.2±9.5	301.8±19.4
s02 MC truth	205	195	25	308
nonrel - nonrel	202.3±14.6	210.0±18.2	13.1±8.0	307.6±19.5
rel - rel	223.2±15.8	192.5±18.2	13.1±8.6	304.2±19.5
phsp - rel	207.6±14.9	205.5±18.4	13.2±8.5	306.7±19.5
phsp - nonrel	207.7±14.9	207.7±18.4	10.8±8.2	306.7±19.5
nonrel - rel	202.2±14.6	208.2±18.2	15.0±8.1	307.6±19.5
rel - nonrel	223.3±15.8	194.8±18.1	10.6±8.2	304.3±19.4
s03 MC truth	179	187	29	277
nonrel - nonrel	174.4±13.6	191.6±18.5	22.3±9.3	283.8±19.1
rel - rel	195.6±15.0	169.4±18.3	24.6±9.6	282.4±19.1
phsp - rel	179.3±13.9	186.4±18.5	22.9±9.5	283.5±19.1
phsp - nonrel	179.1±13.9	186.6±18.4	22.8±9.4	283.4±19.1
nonrel - rel	174.4±13.6	191.5±18.6	22.2±9.4	283.8±19.1
rel - nonrel	195.3±15.0	170.4±18.2	23.9±9.4	282.4±19.1
s04 MC truth	179	180	30	316
nonrel - nonrel	173.7±13.6	198.0±18.1	27.1±9.2	306.1±19.5
rel - rel	192.1±14.8	180.8±18.1	28.5±9.7	303.5±19.5
phsp - rel	178.2±13.9	193.2±18.2	28.1±9.6	305.4±19.5
phsp - nonrel	178.3±13.9	195.4±18.1	25.8±9.3	305.3±19.5
nonrel - rel	173.7±13.6	196.3±18.1	28.8±9.5	306.1±19.5
rel - nonrel	192.1±14.8	183.5±18.0	25.8±9.3	303.5±19.5
s05 MC truth	185	159	25	275
nonrel - nonrel	190.4±14.1	143.9±16.3	45.6±10.2	264.0±18.2
rel - rel	213.8±15.5	121.2±16.2	47.4±10.6	261.4±18.1
phsp - rel	196.1±14.5	137.8±16.4	46.3±10.5	263.6±18.2
phsp - nonrel	196.4±14.5	140.0±16.3	44.2±10.2	263.3±18.1
nonrel - rel	190.5±14.1	142.5±16.4	46.6±10.3	264.4±18.2
rel - nonrel	213.7±15.5	125.2±15.9	43.9±10.2	261.2±18.0

Table 5.6: The results for the test of the fitting procedure are shown for the $J/\psi \to \mu^+\mu^-$ channel. The $J/\psi\,(K^+K^-)_{\text{other}}$ component is modeled with a phase space function. The labeling of the different PDF models is described in the text in section 5.1.3.

Chapter 6

Analysis of the full $\Upsilon(5S)$ data sample

After developing the fitting procedure for the extraction of the signal and background yields in the previous chapter, the default PDF model introduced in section 5.2 is now applied to the full $\Upsilon(5S)$ data sample. This chapter presents the results obtained from this study. The first section examines the measured signal yields and the derived branching ratios. Compared to hadron collider experiments, the Belle experiment has the advantage that the total number of produced B_s^0 mesons is known precisely, which allows to determine absolute branching fractions instead of normalizations relative to a reference decay mode, as it is done by LHCb, CDF and DØ. The second section summarizes all systematic uncertainties that enter the branching fraction measurement. The third section of this chapter is devoted to the measurement of the S-wave contribution within the $\phi(1020)$ mass region, while the last section investigates systematic effects arising from a possible contribution of the decay $B_s^0 \to J/\psi f_0(980)$.

6.1 Obtained signal yields and branching ratios

As it was done during the investigation of the MC simulated data, the fit used for the extraction of the signal and background yields is performed as a 2-dimensional unbinned likelihood fit on the ΔE and the $M(K^+K^-)$ distributions. All PDF parameters are fixed, except the position of the double Gaussian and the combination of Crystal Ball and Gaussian PDF, respectively. The yields for the $J/\psi\phi(1020)$, the $J/\psi(K^+K^-)_{\text{other}}$, the $J/\psi f_2'(1525)$ and the background components are also float-

Channel	$J/\psi \to e^+e^-$	$J/\psi \to \mu^+\mu^-$
$J/\psi\,\phi(1020)$	168 ± 13.5	158 ± 13
$J/\psi(K^+K^-)_{\rm other}$	83 ± 17	67 ± 14
$J/\psi\,f_2'(1525)$	34 ± 10	26 ± 8
Background	232 ± 19	300 ± 20

Table 6.1: The extracted yields for the signal and background components are separately listed for the $J/\psi \to e^+e^-$ and $J/\psi \to \mu^+\mu^-$ channel. The obtained results for the signal components in both channels are in agreement with each other within their statistical error.

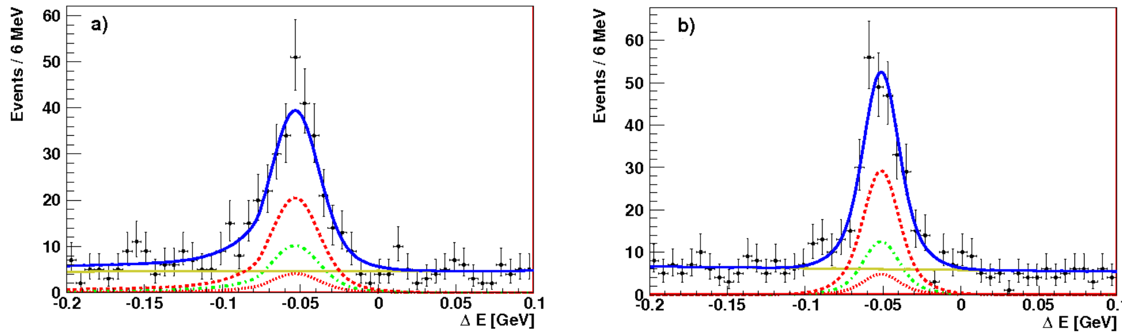

Figure 6.1: The fitted ΔE distribution is shown a) for the $J/\psi \to e^+e^-$ channel and b) for the $J/\psi \to \mu^+\mu^-$ channel. The data is illustrated as black dots with error bars and the blue solid line represent the complete PDF model fitted to the data. From top to bottom, the remaining dashed red and green lines are the $J/\psi\phi\,(1020)$, the $J/\psi\,(K^+K^-)_{\rm other}$ and the $J/\psi f_2'\,(1525)$ signal components, while the solid yellow line indicate the background distribution.

ing parameters.

The obtained yields for the signal and the background components are summarized in table 6.1, while the fitted ΔE and $M\,(K^+K^-)$ distributions are presented in figures 6.1 and 6.2, respectively. The signal yields for the $J/\psi \to e^+e^-$ and the $J/\psi \to \mu^+\mu^-$ channel are found to be consistent within their statistical error which is in agreement with the expectations as the difference in the reconstruction efficiencies (see table 6.2) for both channels is only about 2%. The fitted ΔE and $M\,(K^+K^-)$ distributions show a very good agreement between the data and the applied PDF model.

From the signal yields the absolute branching ratio for the decay $B_s^0 \to J/\psi\phi\,(1020)$ is calculated as:

$$\mathcal{B}[B_s^0 \to J/\psi\,\phi(1020)] = \frac{N_{J/\psi\,\phi(1020)}}{2\mathcal{L}\sigma_{b\bar{b}}f_s f_{B_s^*\bar{B}_s^*}\epsilon\,\mathcal{B}[J/\psi \to \ell^+\ell^-]\mathcal{B}[\phi(1020) \to K^+K^-]} \tag{6.1}$$

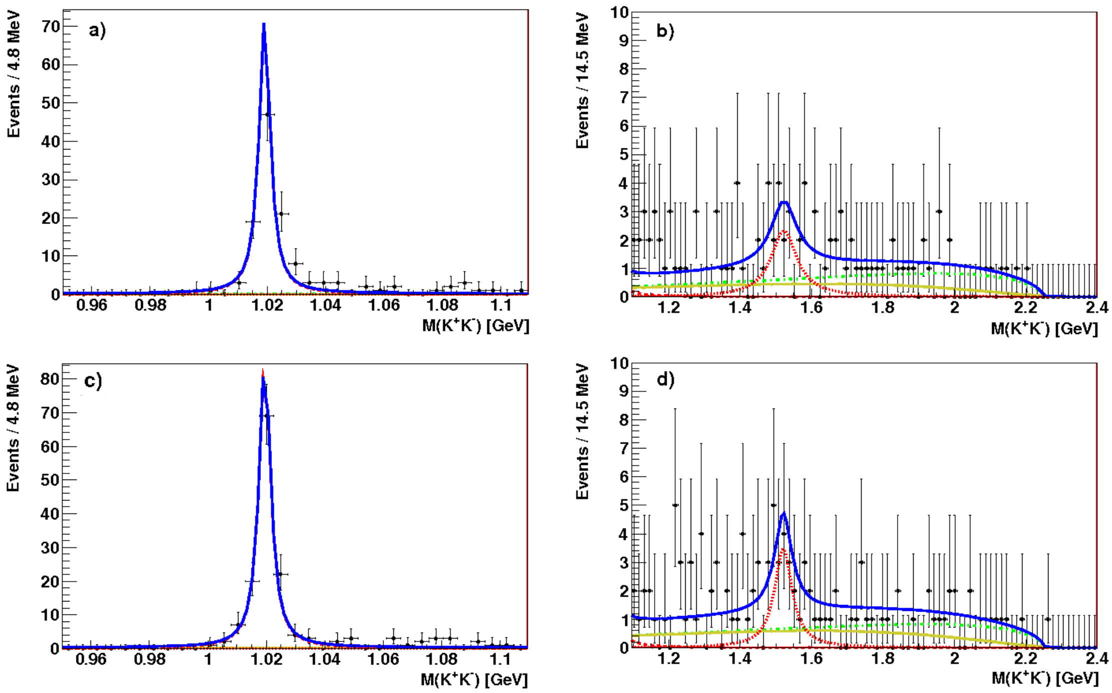

Figure 6.2: The fitted $M\left(K^{+}K^{-}\right)$ distribution is separated in two energy regions to provide a better overview. Plots a) and b) represent the $J/\psi \to e^{+}e^{-}$ channel, while c) and d) are the corresponding plots for the $J/\psi \to \mu^{+}\mu^{-}$ channel. The data is illustrated as black dots with error bars and the blue solid line represent the complete PDF model fitted to the data. The $J/\psi\phi\,(1020)$ component is indicated as red dashed line in a) and c), which overlaps with the line for the complete PDF. The red dashed line in b) and d) represent the $J/\psi f_{2}'\,(1525)$ component. In all plots the $J/\psi\left(K^{+}K^{-}\right)_{\text{other}}$ component and the background are shown as green dashed line solid yellow line, respectively.

separately for the $J/\psi \to e^{+}e^{-}$ and the $J/\psi \to \mu^{+}\mu^{-}$ channel. In equation 6.1 the parameter $N_{J/\psi\,\phi(1020)}$ denotes the fitted signal yield for the respective decay, $\mathcal{L}$ the luminosity of the full $\Upsilon\,(5S)$ Belle data sample, $\sigma_{b\bar{b}}$ the cross section for the process $e^{+}e^{-} \to b\bar{b}$, f_s the fraction of $b\bar{b}$ states containing a B_s meson, $f_{B_s^*\bar{B}_s^*}$ the ratio of $B_s^*\bar{B}_s^*$ states within all B_s events, and $\mathcal{B}[J/\psi \to \ell^{+}\ell^{-}]$ and $\mathcal{B}[\phi(1020) \to K^{+}K^{-}]$ the branching fractions of the respective sub-decays of the J/ψ and the $\phi\,(1020)$ resonances. The reconstruction efficiency ϵ is determined from signal MC data separately for $B_s^0 \to J/\psi\phi\,(1020)$, $B_s^0 \to J/\psi f_2'\,(1525)$ and $B_s^0 \to J/\psi\left(K^{+}K^{-}\right)_{\text{other}}$. It is defined as the ratio of correctly reconstructed events of one decay mode with respect to the total number of events that were generated in the MC data for the decays under consideration and has to be modified with a small correction factor arising from the lepton and kaon identification (see table 6.3). Table 6.2 summarizes the reconstruction efficiencies for all three decays, separately for the $J/\psi \to e^{+}e^{-}$

Channel	$\epsilon_{J/\psi\to e^+e^-}$ [%]	$\epsilon_{J/\psi\to \mu^+\mu^-}$ [%]
$J/\psi\,\phi(1020)$	31.0 ± 0.1	33.2 ± 0.1
$J/\psi(K^+K^-)_{\text{other}}$	29.7 ± 0.1	32.5 ± 0.1
$J/\psi\, f_2'(1525)$	28.4 ± 0.2	30.5 ± 0.2

Table 6.2: The reconstruction efficiency ϵ is given for all three investigated decay modes, separately for the $J/\psi \to e^+e^-$ and $J/\psi \to \mu^+\mu^-$ channel. These numbers already include the ratio $f_{B_s^*\bar{B}_s^*}$, but not the correction factor arising from the lepton and kaon identification (table 6.3). The quoted errors result from the uncertainty due to the limited MC statistics. The values for the decay $B_s^0 \to J/\psi\,\phi(1020)$ is obtained using the signal MC data sample that is based on the polarization parameters determined by CDF [27] (see section 4.2.2).

particle	e^+	e^-	μ^+	μ^-	K^+	K^-
correction factor	0.9844	0.9846	0.9832	0.9824	1.0059	1.0096

Table 6.3: The corrections factors for the reconstruction efficiencies are determined with $\gamma\gamma \to \ell^+\ell^-$ events for the leptons and from a D^* data sample for the kaons.

and the $J/\psi \to \mu^+\mu^-$ channels.

The absolute branching ratios for the decays $B_s^0 \to J/\psi\phi\,(1020)$, $B_s^0 \to J/\psi f_2'\,(1525)$ and $B_s^0 \to J/\psi K^+K^-$ are separately calculated for the $J/\psi \to e^+e^-$ and $J/\psi \to \mu^+\mu^-$ channel, before they are combined to a final results. Equations 6.2 to 6.4 present the obtained branching fractions for the decay $B_s^0 \to J/\psi\phi\,(1020)$:

$$\mathcal{B}\left[B_s^0 \to J/\psi_{e^+e^-}\phi\,(1020)\right] = (1.34 \pm 0.11\,(\text{stat}) \pm 0.09\,(\text{syst}) \pm 0.23\,(f_s))\,10^{-3} \tag{6.2}$$

$$\mathcal{B}\left[B_s^0 \to J/\psi_{\mu^+\mu^-}\phi\,(1020)\right] = (1.18 \pm 0.10\,(\text{stat}) \pm 0.08\,(\text{syst}) \pm 0.21\,(f_s))\,10^{-3} \tag{6.3}$$

$$\mathcal{B}\left[B_s^0 \to J/\psi\,\phi(1020)\right] = (1.25 \pm 0.07\,(\text{stat}) \pm 0.08\,(\text{syst}) \pm 0.22\,(f_s))10^{-3} \tag{6.4}$$

The statistical errors quoted in equations 6.2 and 6.3 arise from the uncertainty in the fitted signal yields. The combined result given in equation 6.4 is calculated as the weighted mean value of the branching fractions obtained for the $J/\psi \to e^+e^-$ and $J/\psi \to \mu^+\mu^-$ channels. The determination of the systematic error is described in section 6.2.

The branching ratios obtained for the $J/\psi \to e^+e^-$ and $J/\psi \to \mu^+\mu^-$ channels are consistent with each other within their error range. The combined result is in good agreement with the measurements from the CDF Run I ($\mathcal{B}\,[B_s^0 \to J/\psi\,\phi(1020)] = (0.93 \pm 0.28 \pm 0.10 \pm 0.14)10^{-3}$) [7,9] and their recent result obtained from the full

CDF data sample ($\mathcal{B}[B_s^0 \to J/\psi\,\phi(1020)] = (1.18 \pm 0.02 \pm 0.09 \pm 0.14 \pm 0.05)10^{-3}$) [8] as well as the LHCb measurement ($\mathcal{B}[B_s^0 \to J/\psi\,\phi(1020)] = (1.050 \pm 0.013 \pm 0.064 \pm 0.082)10^{-3}$) [6].

In order to determine the absolute branching fraction of the decay $B_s^0 \to J/\psi f_2'(1525)$, equation 6.1 is adapted by replacing the signal yield and the reconstruction efficiency with the values obtained for the $B_s^0 \to J/\psi f_2'(1525)$ component and exchanging the sub-decay branching ratio for $\phi(1020) \to K^+K^-$ with the one for $f_2'(1525) \to K^+K^-$. Equations 6.5 to 6.7 list the results that were obtained for the decay mode $B_s^0 \to J/\psi f_2'(1525)$:

$$\mathcal{B}\left[B_s^0 \to J/\psi_{e^+e^-} f_2'(1525)\right] = (0.32 \pm 0.10\,(\text{stat}) \pm 0.03\,(\text{syst}) \pm 0.06\,(f_s))\,10^{-3} \tag{6.5}$$

$$\mathcal{B}\left[B_s^0 \to J/\psi_{\mu^+\mu^-} f_2'(1525)\right] = (0.23 \pm 0.07\,(\text{stat}) \pm 0.02\,(\text{syst}) \pm 0.04\,(f_s))\,10^{-3} \tag{6.6}$$

$$\mathcal{B}\left[B_s^0 \to J/\psi\, f_2'(1525)\right] = (0.26 \pm 0.06\,(\text{stat}) \pm 0.02\,(\text{syst}) \pm 0.05\,(f_s))10^{-3} \tag{6.7}$$

The statistical error is again determined from the uncertainty in the fitted signal yield and the combined result is obtained as the weighted mean value of the $J/\psi \to e^+e^-$ and $J/\psi \to \mu^+\mu^-$ channels. The statistical significance of the absolute branching fraction for $B_s^0 \to J/\psi\, f_2'(1525)$ is calculated from the difference between the logarithm of the likelihood value obtained from the fit with all components and the value obtained from a fit without the $J/\psi\, f_2'(1525)$ component ("background hypothesis") [9]. Including the systematic uncertainty, it is equal to 3.3 standard deviations.

The branching ratios for the $J/\psi \to e^+e^-$ and $J/\psi \to \mu^+\mu^-$ channels are consistent within their error ranges and the combined result is in good agreement with the branching ratio calculated by LHCb ($\mathcal{B}\left[B_s^0 \to J/\psi\, f_2'(1525)\right] = (0.261 \pm 0.020^{+0.052}_{-0.046} \pm 0.020)10^{-3}$) [6].

The branching fraction for $B_s^0 \to J/\psi\, f_2'(1525)$ relative to the branching fraction for $B_s^0 \to J/\psi\,\phi(1020)$ is thus determined to be

$$\frac{\mathcal{B}[B_s^0 \to J/\psi\, f_2'(1525)]}{\mathcal{B}[B_s^0 \to J/\psi\,\phi(1020)]} = (21.5 \pm 4.9\,(\text{stat}) \pm 2.6\,(\text{syst}))\% \tag{6.8}$$

Figure 6.3 shows a comparison between this result and the values reported from LHCb [4] and DØ [5]. It is clearly visible, that this Belle result is in perfect agreement with the results from the hadron collider experiments.

The entire branching ratio for the decay $B_s^0 \to J/\psi K^+K^-$ that includes the resonant

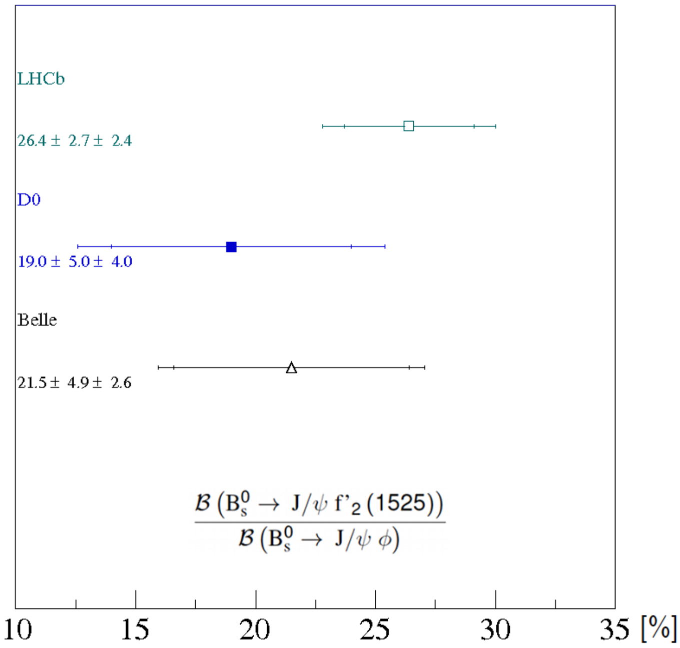

Figure 6.3: Comparison of the relative branching ratio $\mathcal{B}[B_s^0 \to J/\psi\, f_2'(1525)]/\mathcal{B}\,[B_s^0 \to J/\psi\,\phi(1020)]$ determined in this analysis with the results that are reported by hadron collider experiments [4, 5].

and nonresonant components is defined as:

$$\mathcal{B}\left(B_s^0 \to J/\psi K^+K^-\right) = \mathcal{B}\left[B_s^0 \to J/\psi\phi\,(1020)\right] \cdot \mathcal{B}\left(\phi \to K^+K^-\right) + \mathcal{B}\left(B_s^0 \to J/\psi\; K^+K^-_{\text{other}}\right) + \mathcal{B}\left[B_s^0 \to J/\psi\; f_2'\,(1525)\right] \cdot \mathcal{B}\left(f_2'\,(1525) \to K^+K^-\right) \tag{6.9}$$

The absolute branching ratios of the decays $B_s^0 \to J/\psi\phi\,(1020)$ and $B_s^0 \to J/\psi\; f_2'\,(1525)$ have to be adjusted with the sub-decay branching fractions for the $\phi\,(1020)$ and the $f_2'\,(1525)$ resonances. The obtained results are summarized in equations 6.10 to 6.12:

$$\mathcal{B}\left(B_s^0 \to J/\psi_{e^+e^-}K^+K^-\right) = \left(1.13 \pm 0.15\,(\text{stat}) \pm 0.12\,(\text{syst}) \pm 0.20\,(f_s)\right) 10^{-3} \tag{6.10}$$

$$\mathcal{B}\left(B_s^0 \to J/\psi_{\mu^+\mu^-}K^+K^-\right) = \left(0.93 \pm 0.12\,(\text{stat}) \pm 0.09\,(\text{syst}) \pm 0.16\,(f_s)\right) 10^{-3} \tag{6.11}$$

$$\mathcal{B}\left(B_s^0 \to J/\psi\, K^+K^-\right) = \left(1.01 \pm 0.09\,(\text{stat}) \pm 0.10\,(\text{syst}) \pm 0.18\,(f_s)\right)10^{-3} \tag{6.12}$$

As before, the results for the $J/\psi \to e^+e^-$ and $J/\psi \to \mu^+\mu^-$ samples are consistent within their error ranges. The weighted mean value cited in equation 6.12 is in good agreement with the branching fraction observed by LHCb ($\mathcal{B}\,(B_s^0 \to J/\psi\, K^+K^-) = (0.770 \pm 0.008\,(\mathrm{stat}) \pm 0.039\,(\mathrm{syst}) \pm 0.060\,(f_s))10^{-3}$) [6].

6.2 Systematic uncertainties of branching fractions

The systematic uncertainties that enter the calculation of the absolute branching ratios are summarized in table 6.4. They are divided into three categories: The first one includes all errors that are related to input parameters, such as the luminosity, the $e^+e^- \to b\bar{b}$ cross section and sub-decay branching fractions. This category gives the dominant contribution to the total systematic error due to the uncertainty in the fraction of $b\bar{b}$ states containing a B_s meson. Therefore the error related to f_s is quoted separately for all results presented in the previous section. The second group of uncertainties contains the errors that arise from the simulation of the decay modes and the detector response. These uncertainties change the reconstruction efficiency and include errors from the limited MC statistics as well as from the polarization in the decay $B_s^0 \to J/\psi\phi\,(1020)$, from track reconstruction and particle identification. The last category of systematic errors describe the impact of the PDF parametrization and of the choice of the PDF model.

As already indicated in section 4.2.2, the systematic error related to the polarization in the decay $B_s^0 \to J/\psi\phi\,(1020)$ is estimated by comparing two different signal MC data samples. One of the two samples was produced with the polarization parameters determined by the CDF collaboration [27] and used to determine the reconstruction efficiency given in table 6.2. This efficiency is compared with the efficiency obtained from the other MC sample based on the default values for the polarization parameters in the Belle MC which lie outside of the error range reported by CDF. The difference in the reconstruction efficiencies which are calculated for these two MC samples is taken as the systematic uncertainty related to polarization in $B_s^0 \to J/\psi\phi\,(1020)$.

The systematic error that arises from the lepton identification is determined using $\gamma\gamma \to \ell^+\ell^-$ events [59, 60, 70], while the uncertainty due to the kaon identification is based on a data sample of $D^{*+} \to D^0\pi^+$ decays with $D^0 \to K^-\pi^+$ [71].

The error originating from the uncertainty in the PDF shape is based on the applied PDF parametrization. Every PDF parameter that was determined during the development of the fitting procedure on the generic MC (see section 5.1.1) is de-

Parameter	Value	Error	%
$\mathcal{L}$	121.4 fb^{-1}	0.8498 fb^{-1}	0.7
$\sigma_{b\bar{b}}$ [47]	0.340 nb	0.016 nb	4.7
f_s [47]	0.172	0.030	17.4
$f_{B_s^* \bar{B}_s^*}$ [50]	0.87	0.017	2.0
$\mathcal{B}(J/\psi \to e^+e^-)$ [9]	0.0594	0.0006	1.0
$\mathcal{B}(J/\psi \to \mu^+\mu^-)$ [9]	0.0593	0.0006	1.0
$\mathcal{B}(\phi \to K^+K^-)$ [9]	0.489	0.005	1.0
$\mathcal{B}(f_2'(1525) \to K^+K^-)$ [9]	0.444	0.011	2.5
$\epsilon_{\text{MC statistic}}\ [J/\psi_{e^+e^-}\phi(1020)]$	-	0.001	0.4
$\epsilon_{\text{MC statistic}}\ [J/\psi_{\mu^+\mu^-}\phi(1020)]$	-	0.001	0.3
$\epsilon_{\text{MC statistic}}\ [J/\psi_{e^+e^-}\ (K^+K^-)_{\text{other}}]$	-	0.001	0.3
$\epsilon_{\text{MC statistic}}\ (J/\psi_{\mu^+\mu^-}\ (K^+K^-)_{\text{other}}]$	-	0.001	0.3
$\epsilon_{\text{MC statistic}}\ [J/\psi_{e^+e^-} f_2'(1525)]$	-	0.002	0.8
$\epsilon_{\text{MC statistic}}\ [J/\psi_{\mu^+\mu^-} f_2'(1525)]$	-	0.002	0.8
$\epsilon_{\text{polarization}}\ (J/\psi \to e^+e^-)$	-	0.004	1.3
$\epsilon_{\text{polarization}}\ (J/\psi \to \mu^+\mu^-)$	-	0.004	1.3
tracking	-	-	1.4
e$^+$ identification	-	0.0150	1.5
e$^-$ identification	-	0.0151	1.5
μ^+ identification	-	0.0151	1.5
μ^- identification	-	0.0143	1.5
K$^+$ identification	-	0.0089	0.9
K$^-$ identification	-	0.0099	1.0
PDF shape:			
$B_s^0 \to J/\psi_{e^+e^-}\phi(1020)$	-	1.9 events	1.1
$B_s^0 \to J/\psi_{\mu^+\mu^-}\phi(1020)$	-	1.5 events	1.0
$B_s^0 \to J/\psi_{e^+e^-}\ (K^+K^-)_{\text{other}}$	-	7.6 events	9.1
$B_s^0 \to J/\psi_{\mu^+\mu^-}\ (K^+K^-)_{\text{other}}$	-	3.9 events	5.8
$B_s^0 \to J/\psi_{e^+e^-} f_2'(1525)$	-	2.6 events	7.8
$B_s^0 \to J/\psi_{\mu^+\mu^-} f_2'(1525)$	-	1.4 events	5.4
PDF model:			
$B_s^0 \to J/\psi_{e^+e^-}\ (K^+K^-)_{\text{other}}$	-	2.0 events	2.4
$B_s^0 \to J/\psi_{\mu^+\mu^-}\ (K^+K^-)_{\text{other}}$	-	2.0 events	3.0

Table 6.4: List of all systematic errors that enter the determination of the absolute branching ratios described in section 6.1. The parameter f_s that describes the fraction of $b\bar{b}$ states containing a B_s meson is the most dominant systematic error and highlighted in blue.

fined by its central value and error. These values are used as input parameters for the position and the width of a Gaussian distribution. To determine the systematic error related to the PDF shape, a toy MC study is performed 1000 times, in which all PDF parameters are randomly selected from such a Gaussian distribution before the PDF model is fitted to the data. The distribution of all fitted signal yields that are obtained from these pseudoexperiments is then fitted with a Gaussian function and its width is defined as the related systematic error. Correlations between the different PDF parameters were investigated and found to be negligibly small.

The default PDF model used to extract the signal yields on the full $\Upsilon(5S)$ data sample applies a nonrelativistic Breit-Wigner PDF to fit the $\phi(1020)$ and the $f_2'(1525)$ resonance and an ARGUS function to model the $J/\psi\,(K^+K^-)_{\mathrm{other}}$ component. However, the test on the generic MC data samples has shown that the $\phi(1020)$ and the $f_2'(1525)$ peaks can also be described by a relativistic Breit-Wigner function or a nonrelativistic Breit-Wigner PDF with a phase space correction factor, while the $J/\psi\,(K^+K^-)_{\mathrm{other}}$ component can also be modeled with a pure phase space description instead of using the ARGUS function (see section 5.1.3). In order to estimate the systematic error due to chosen default PDF model, the difference between the default PDFs and the alternative PDFs on the signal yield on one MC stream are taken as systematic error. The different signal components $J/\psi\phi(1020)$, $J/\psi f_2'(1525)$ and $J/\psi\,(K^+K^-)_{\mathrm{other}}$ are selected based on information from the MC generator and fitted separately in the $M(K^+K^-)$ distribution.

In case of the $\phi(1020)$ resonance, the nonrelativistic Breit-Wigner PDF with a phase space correction factor and the relativistic Breit-Wigner function are taken into account as alternative PDFs. The signal yields obtained from the fit with the default nonrelativistic Breit-Wigner and the yields obtained from the two alternative PDFs show no differences. Fitting the $f_2'(1525)$ resonance with a relativistic Breit-Wigner and comparing the result with the fitted yields obtained with the default description using a nonrelativistic Breit-Wigner also shows no mismatch. Therefore, no systematic uncertainty is assigned for these components. The nonrelativistic Breit-Wigner with phase space correction factor is not investigated as possible alternative description of the $f_2'(1525)$ resonance as the phase space is flat around the $f_2'(1525)$ resonance. However, the comparison between the fitted yield of the $J/\psi\,(K^+K^-)_{\mathrm{other}}$ component using the default ARGUS function and the phase space description reveals a deviation of 2 events which is taken as systematic error.

The total systematic error of the results for the $J/\psi \to e^+e^-$ and the $J/\psi \to \mu^+\mu^-$ channels was obtained by adding all systematic uncertainties in quadrature. In order to determine the systematic error of the weighted mean value for the absolute branching fractions $\mathcal{B}[B_s^0 \to J/\psi\,\phi(1020)]$ and $\mathcal{B}[B_s^0 \to J/\psi\, f_2'(1525)]$, the systematic uncertainties quoted for the $J/\psi \to e^+e^-$ and the $J/\psi \to \mu^+\mu^-$ channels are treated as fully correlated which is a conservative approach. Regarding the weighted mean value of the branching fraction $\mathcal{B}(B_s^0 \to J/\psi\, K^+K^-)$, the systematic uncertainties arising from the PDF parametrization and the PDF model are regarded as uncorrelated components while all other contributing components are treated as correlated errors.

6.3 Determination of the S-wave contribution

Until now, the S-wave contribution within the $\phi(1020)$ mass range has only been measured at hadron collider experiments. While the ATLAS experiment reports an S-wave contribution of $(2 \pm 2)\,\%$ [29] which is consistent with zero, the CDF collaboration and the LHCb experiment publish S-wave components of $(0.8 \pm 0.2)\%$ [27] and $(1.1 \pm 0.1^{+0.2}_{-0.1})\%$ [6], respectively. Although these results are all based on slightly different $M(K^+K^-)$ regions around the $\phi(1020)$ resonance, they seem quite consistent and indicate an S-wave component in the order of 1% to 2%, which is in disagreement with the results published by the DØ experiment that claims an S-wave contribution of $(14.7 \pm 3.5)\,\%$ [28]. As all of these hadron collider experiments determine the S-wave component with an angular analysis, these results might suffer from the same systematic effects. Therefore, an independent analysis based on a different method provides a complementary measurement, which is helpful to clarify the current experimental situation.
Instead of performing an angular analysis, the method presented in this thesis distinguishes the S- and the P-wave components by the fitted $M(K^+K^-)$ distribution. In order to calculate the S-wave contribution within a specific mass region below the $\phi(1020)$ resonance, the following two assumptions are made:

1. The decay $B_s^0 \to J/\psi\phi(1020)$ is the only source of the P-wave contribution.

2. The S-wave contribution completely originates from the $J/\psi\,(K^+K^-)_{\text{other}}$ component.

In order to verify that the $J/\psi\,(K^+K^-)_{\text{other}}$ component is dominated by the nonresonant decay $B_s^0 \to J/\psi K^+K^-$ and thus is a pure S-wave component, the helicity distribution of this mode is investigated. The corresponding helicity angle is defined as the angle between the K^+ and B_s^0 meson in the K^+K^- rest frame. The angular distribution that is presented in figure 6.4 is obtained from the full $\Upsilon(5S)$ data sample by combining the $J/\psi \to e^+e^-$ and the $J/\psi \to \mu^+\mu^-$ channel. In figure 6.4, the helicity distributions of the decay $B_s^0 \to J/\psi\phi(1020)$ (determined from signal MC data based on the CDF polarization parameters [27]) and the combinatorial background (estimated via the sideband in M_{bc}, defined by $5.25\,\mathrm{GeV} \leq M_{bc} \leq 5.35\,\mathrm{GeV}$) are subtracted from the data sample and a $\pm 5\sigma$ region around the $f_2'(1525)$ resonance is faded out. Thus, only events from the $J/\psi(K^+K^-)_{\mathrm{other}}$ component remain in the plotted data which are consistent with a flat distribution as expected from a contribution that is dominated by an S-wave component.

During the test of the fitting procedure on generic MC data (see section 5.1.3) as well as during the fit on the full $\Upsilon(5S)$ data sample (see section 6.1), no evidence for any additional signal component besides $J/\psi\phi(1020)$, $J/\psi(K^+K^-)_{\mathrm{other}}$ and $J/\psi f_2'(1525)$ was found. Otherwise, the observed agreement between the data and the applied PDF model would not have been possible. Furthermore, after subtracting the helicity distribution of the decay $B_s^0 \to J/\psi\phi(1020)$ no additional P-wave component has been found in the angular distribution presented in figure 6.4. Thus, the decay $B_s^0 \to J/\psi\phi(1020)$ is the only significant source of the P-wave contribution for this investigation.

In this analysis, the S-wave contribution (S) is defined as the ratio between the number of events from the $J/\psi(K^+K^-)_{\mathrm{other}}$ component and the total amount of events from the $J/\psi\phi(1020)$ and the $J/\psi(K^+K^-)_{\mathrm{other}}$ components within a specific

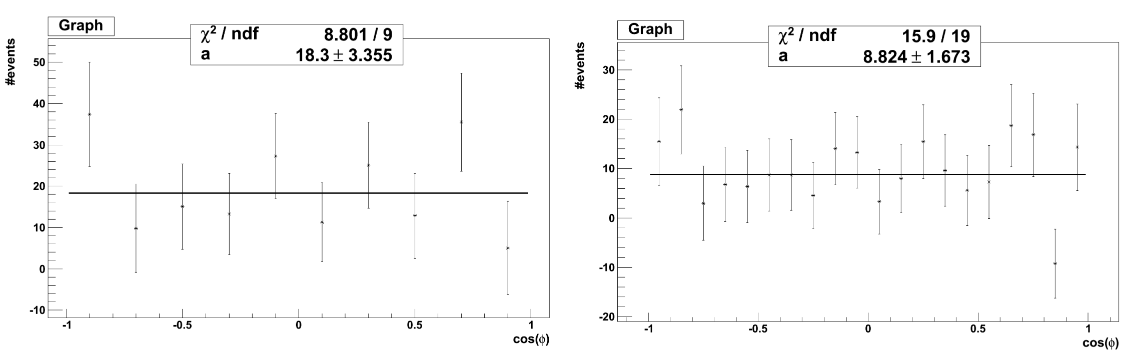

Figure 6.4: The distribution of the helicity angle for the $J/\psi(K^+K^-)_{\mathrm{other}}$ component is given in radiant and combines the data from the $J/\psi \to e^+e^-$ and the $J/\psi \to \mu^+\mu^-$ channel in 10 bins (left plot) and 20 bins (right plot), respectively. Both histograms are fitted with a constant function and the obtained χ^2/ndf value shows, that they are in good agreement with the assumption of a flat distribution.

Mass range	1.009 GeV – 1.028 GeV
CDF [27]	$(0.8 \pm 0.2)\%$
This analysis	$(0.47 \pm 0.07 \pm 0.22^{+2.2}_{-0})\%$
Mass range	1.007 GeV – 1.031 GeV
LHCb [6]	$(1.1 \pm 0.1^{+0.2}_{-0.1})\%$
This analysis	$(0.57 \pm 0.09 \pm 0.26^{+2.0}_{-0})\%$

Table 6.5: The quoted values for the S-wave contribution are the combined results from the $J/\psi \to e^+e^-$ and $J/\psi \to \mu^+\mu^-$ channel. The calculation is performed for the same mass regions around the $\phi(1020)$ resonance that were used by the CDF and the LHCb experiments. The first cited error is the statistical uncertainty, while the second error arises from systematic uncertainties. The third error arises from the uncertainty due to a possible $B_s^0 \to J/\psi f_0(980)$ contribution (see section 6.4).

mass range:

$$S = \frac{\alpha \cdot N\left[J/\psi\,(K^+K^-)_{\text{other}}\right]}{\alpha \cdot N\left[J/\psi\,(K^+K^-)_{\text{other}}\right] + \beta \cdot N\left[J/\psi\phi\,(1020)\right]} \tag{6.13}$$

In equation 6.13 the variables $N\left[J/\psi\,(K^+K^-)_{\text{other}}\right]$ and $N\left[J/\psi\phi\,(1020)\right]$ denote the signal yields given in table 6.1. The parameters α and β are the fractions of the ARGUS function and the nonrelativistic Breit-Wigner, respectively, within the mass range around the $\phi\,(1020)$ resonance that is considered in this analysis.

Table 6.5 summarizes the results obtained in this analysis for the mass ranges used by the CDF and LHCb experiments. As it was done for the determination of the absolute branching ratios, the calculation of the S-wave contribution is performed separately for the $J/\psi \to e^+e^-$ and $J/\psi \to \mu^+\mu^-$ channels, before it is combined for the final result. Even though the central values obtained using equation 6.13 are somewhat smaller than the results reported by the hadron collider experiments, they are still in agreement with the CDF and LHCb values.. The statistical error of the determined S-wave contribution is calculated from the uncertainties in the fitted signal yields of the $J/\psi\phi\,(1020)$ and $J/\psi\,(K^+K^-)_{\text{other}}$ components. The systematic error that arises from the uncertainty in the PDF parametrization and the applied PDF model is propagated through the parameters α and β. The possible presence of a $B_s^0 \to J/\psi f_0\,(980)$ component, as it was claimed by LHCb [6], results in an additional source of a systematic error. This error is quoted separately in table 6.5 and discussed in the next section.

6.4 Systematic error from a possible $B_s^0 \to J/\psi\, f_0\,(980)$ component

The decay $B_s^0 \to J/\psi f_0\,(980)$ in which the $f_0\,(980)$ meson decays into two oppositely charged kaons has not been studied yet in this analysis. However, the LHCb collaboration claims that this decay mode is of a similar size than the decay $B_s^0 \to J\psi f_2'\,(1525)$ [6], which would mean that it has a significant impact on the study of $B_s^0 \to J\psi K^+K^-$ decays.
The LHCb experiment models the $f_0\,(980)$ resonance with a Flatté function [72] and takes into account the interference effects with the $J/\psi\,(K^+K^-)_{\text{other}}$ component. Thus, the $B_s^0 \to J/\psi f_0\,(980)$ decay is included in the present analysis by exchanging the ARGUS function that describes the $J/\psi\,(K^+K^-)_{\text{other}}$ component in the $M\,(K^+K^-)$ distribution in the default PDF model (see section 5.2) with a coherent sum $CS\,(x)$ of a Flatté function $F\,(x)$ and an ARGUS function $A\,(x;p,c,m_0)$:

$$CS\,(x) = a^2 \cdot F\,(x) + A\,(x;p,c,m_0) + 2a \cdot \cos(\theta) \cdot \sqrt{F\,(x) \cdot A\,(x;p,c,m_0)} \quad (6.14)$$

The parametrization of the Flatté function is based on the BES measurements [73], while the ARGUS parametrization is the same as in the default PDF model. The parameter a denotes the relative normalization between the $J/\psi f_0\,(980)$ and the $J/\psi\,(K^+K^-)_{\text{other}}$ components and θ is the relative phase between these two components. The relative normalization as well as the phase are fixed to $a = 2$ and $\theta = -259°$, respectively, according to the results reported by LHCb [6].
The new PDF model that includes the $B_s^0 \to J/\psi f_0\,(980)$ decay is applied to the generic MC data and to toy MC data as well as to the full $\Upsilon\,(5S)$ data sample and no systematic effect is observed in the fitted yields: most of the yields obtained on MC data are in agreement with the MC truth within the statistical uncertainty. The fit results from the full $\Upsilon\,(5S)$ data sample are presented in table 6.6 and vary

Channel	e^+e^-	$\mu^+\mu^-$
$J/\psi\,\phi\,(1020)$	144±13	139±13
S-wave($\mathrm{J}/\psi\,\mathrm{f}_0\,(980)$) and $\mathrm{J}/\psi\,\left(\mathrm{K}^+\mathrm{K}^-\right)_{\text{other}}$)	109±17	87±15
$J/\psi\, f_2'(1525)$	35±10	27±8
Background	229±19	297±19

Table 6.6: The fitted yields including the decay $B_s^0 \to J/\psi f_0\,(980)$ where the $\mathrm{J}/\psi\,\mathrm{f}_0\,(980)$) and $\mathrm{J}/\psi\,\left(\mathrm{K}^+\mathrm{K}^-\right)_{\text{other}}$ components were fitted according to equation 6.14.

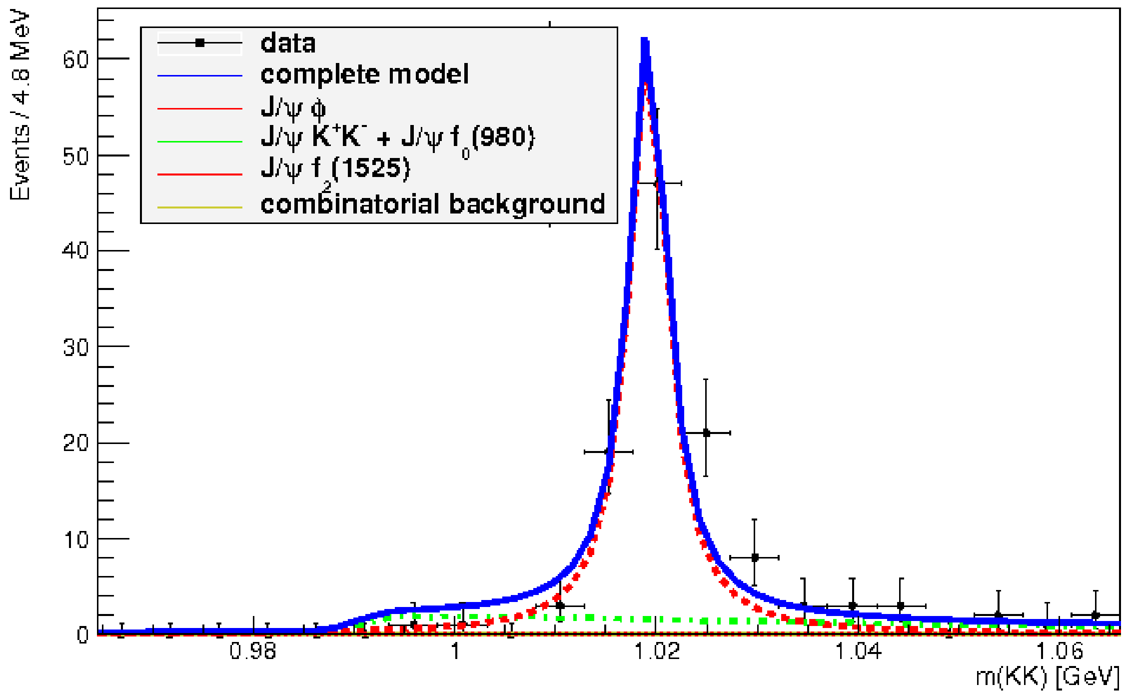

Figure 6.5: The low energy region of the $M(K^+K^-)$ distribution is fitted including the decay mode $B_s^0 \to J/\psi f_0(980)$ and possible interference effects of this mode with the $J/\psi(K^+K^-)_{\text{other}}$ component (equation 6.14). The black dots with error bars present the data obtained from the full $\Upsilon(5S)$ data sample, while the blue solid line illustrates the complete PDF model. The green solid line indicate the coherent sum of the Flatté PDF and the ARGUS function that is used to describe the $J/\psi f_0(980)$ and $J/\psi(K^+K^-)_{\text{other}}$ component simultaneously.

approximately within one standard deviation compared to the results obtained with the default PDF model shown in table 6.1. Thus, the decay $B_s^0 \to J/\psi f_0(980)$ has no significant systematic impact on the determined branching ratios in section 6.1 and no systematic error is assigned.

The fit of the $M(K^+K^-)$ distribution in the full $\Upsilon(5S)$ data sample including a $J/\psi f_0(980)$ component is shown in figure 6.5 for the low energy region around the $\phi(1020)$ resonance. The $J/\psi f_0(980)$ and the $J/\psi(K^+K^-)_{\text{other}}$ components are described by the PDF given in equation 6.14, while all other components are still modeled according to the default PDF model. Any effects arising from the $f_0(980)$ resonance are expected to appear in the energy region just below the $\phi(1020)$ resonance. However, the Belle data does not support the presence of this $J/\psi f_0(980)$ component as the total PDF, illustrated as a blue solid line, systematically lies above the data points in the energy region $M(K^+K^-) \leq 1.1\,\text{GeV}$.

Even though the integration of the decay $B_s^0 \to J/\psi f_0(980)$ has no significant effect on the fitted yields and thus on the determined branching fractions, it still is an important systematic error in the calculation of the S-wave contribution in the $\phi\,(1020)$ mass region. As the signal yield of the $J/\psi f_0\,(980)$ component cannot be estimated with the current Belle statistics, the systematic error arising from this component is propagated through the parameter α which basically describes the shape of the S-wave component in equation 6.13. The uncertainty in α due to a possible $B_s^0 \to J/\psi f_0\,(980)$ contribution is determined by comparing the default PDF model used in this analysis and the PDF model used by LHCb [6]. The value of the parameter α for the LHCb model is estimated from their S-wave contribution of 1.1%, which means an increase of α in the $J/\psi \to e^+e^-$ channel from 0.8% and 1.0% to 5.0% for the CDF and LHCb mass range, respectively, and from 0.9% and 1.1% to 5.0% in the $J/\psi \to \mu^+\mu^-$ channel. This difference is assigned as systematic error due to a possible $J/\psi f_0\,(980)$ component and quoted separately in table 6.5.

Chapter 7

Summary and Conclusion

Although the Standard Model of Particle Physics, describing the fundamental interactions between the elementary particles, is one of the most successful theories so far, it is still considered to be incomplete. One possibility to search for deviations from the Standard Model is the investigation of the CP violating phase ϕ_s, which is accessible through the decay $B_s^0 \to J/\psi\,\phi\,(1020)$ with $J/\psi \to \ell^+\ell^-$ and $\phi\,(1020) \to K^+K^-$. Therefore, dedicated studies of other contributions with the same final state, including the decay $B_s^0 \to J\psi\,f_2'\,(1525)$ as well as nonresonant modes are of great interest in this context. Until now, all information on these decays are mainly based on results from the hadron collider experiments LHCb, CDF and DØ. An investigation performed at a lepton collider experiment is thus a valuable extension to the present experimental status.

The presented analysis is a comprehensive study of the decay mode $B_s^0 \to J/\psi\,K^+K^-$ and determines the absolute branching fractions of the decays $B_s^0 \to J/\psi\,\phi\,(1020)$, $B_s^0 \to J\psi\,f_2'\,(1525)$ and the entire branching ratio for the decay $B_s^0 \to J/\psi\,K^+K^-$, including the resonant and nonresonant decay modes. The full $\Upsilon\,(5S)$ data sample recorded by the Belle experiment at the asymmetric energy electron-positron collider KEKB is used, which corresponds to an integrated luminosity of $121.4\,\mathrm{fb}^{-1}$.

The decay $B_s^0 \to J/\psi\,K^+K^-$ is reconstructed in the $J/\psi \to e^+e^-$ and the $J/\psi \to \mu^+\mu^-$ channel and both channels are investigated separately throughout the analysis. The yields for the three signal components $B_s^0 \to J/\psi\,\phi\,(1020)$, $B_s^0 \to J/\psi\,f_2'\,(1525)$ and $B_s^0 \to J/\psi\,(K^+K^-)_{\mathrm{other}}$ and for the background are extracted using a 2-dimensional unbinned maximum likelihood fit in the energy difference ΔE and the invariant kaon mass distribution $M\,(K^+K^-)$. The absolute branching fractions that were obtained for the $J/\psi \to e^+e^-$ and the $J/\psi \to \mu^+\mu^-$

channels are consistent within their error range for all investigated decay modes. Combining the results of both channels, the absolute branching ratios are measured to be

$$\mathcal{B}\left[B_s^0 \to J/\psi\,\phi(1020)\right] = (1.25 \pm 0.07\,(\text{stat}) \pm 0.08\,(\text{syst}) \pm 0.22\,(f_s))10^{-3} \quad (7.1)$$
$$\mathcal{B}\left[B_s^0 \to J/\psi\,f_2'\,(1525)\right] = (0.26 \pm 0.06\,(\text{stat}) \pm 0.02\,(\text{syst}) \pm 0.05\,(f_s))10^{-3} \quad (7.2)$$
$$\mathcal{B}\left[B_s^0 \to J/\psi\,K^+K^-\right] = (1.01 \pm 0.09\,(\text{stat}) \pm 0.10\,(\text{syst}) \pm 0.18\,(f_s))10^{-3} \quad (7.3)$$

while the branching fraction for $B_s^0 \to J/\psi\,f_2'\,(1525)$ relative to the branching fraction for $B_s^0 \to J/\psi\,\phi(1020)$ is calculated to be

$$\frac{\mathcal{B}[B_s^0 \to J/\psi\,f_2'(1525)]}{\mathcal{B}[B_s^0 \to J/\psi\,\phi(1020)]} = (21.5 \pm 4.9\,(\text{stat}) \pm 2.6\,(\text{syst}))\% \quad (7.4)$$

All these results are in good agreement with the values reported from the hadron collider experiments LHCb, CDF and DØ. The Belle collaboration decided to submit these results to the Particle Data Group for incorporation into the next edition of the "Review of Particle Physics".
The S-wave contribution within two specific $\phi\,(1020)$ mass regions has been determined by separating the S- and P-wave components via the invariant kaon mass distribution. The obtained results for the S-wave are $(0.47 \pm 0.07 \pm 0.22^{+2.2}_{-0})\%$ for a mass range of 1.009 GeV to 1.028 GeV, and $(0.57 \pm 0.09 \pm 0.26^{+2.0}_{-0})\%$ in the range 1.007 GeV to 1.031 GeV. Even though the central values are somewhat smaller than the values published by the CDF and LHCb collaborations, they are still in agreement with the hadron collider results within their error range. In this context, the presence of a possible contribution from the decay $B_s^0 \to J/\psi\,f_0\,(980)$ with $f_0\,(980) \to K^+K^-$, as is claimed by LHCb, has been investigated but not observed. Thus, the LHCb result concerning this decay cannot be confirmed.
However, the Belle II experiment, which is currently being prepared to start data taking in 2016, is expected to collect a data sample with an integrated luminosity 50 times higher than the one obtained at Belle. A search for the decay $B_s^0 \to J/\psi f_0\,(980)$ with $f_0\,(980) \to K^+K^-$ at this next generation experiment can certainly help to clarify this topic.

Appendix A

The Pauli spin matrices and Gell-Mann matrices

The special unitary group $SU(n)$ has $n^2 - 1$ independent generators $T^\alpha = \frac{1}{2}\lambda^\alpha$ which are hermitian $n \times n$ matrices and define the fundamental representation of the $SU(n)$ algebra.
In case of the $SU(2)_L$ symmetry group which describes the weak interaction, the generators are given by the Pauli spin matrices σ_i [1]

$$\sigma_1 = \begin{pmatrix} 0 & 1 \\ 1 & 0 \end{pmatrix} \qquad \sigma_2 = \begin{pmatrix} 0 & -i \\ i & 0 \end{pmatrix} \qquad \sigma_3 = \begin{pmatrix} 1 & 0 \\ 0 & -1 \end{pmatrix} \tag{A.1}$$

satisfying the commutation relation $[\sigma_i, \sigma_j] = 2i\,\epsilon_{ijk}\sigma_k$, where ϵ^{ijk} is the Levi-Civita symbol.
The generators of the $SU(3)_C$ symmetry group for QCD are the Gell-Mann matrices λ^i:

$$\lambda^1 = \begin{pmatrix} 0 & 1 & 0 \\ 1 & 0 & 0 \\ 0 & 0 & 0 \end{pmatrix} \qquad \lambda^2 = \begin{pmatrix} 0 & -i & 0 \\ i & 0 & 0 \\ 0 & 0 & 0 \end{pmatrix} \qquad \lambda^3 = \begin{pmatrix} 1 & 0 & 0 \\ 0 & -1 & 0 \\ 0 & 0 & 0 \end{pmatrix} \tag{A.2}$$

$$\lambda^4 = \begin{pmatrix} 0 & 0 & 1 \\ 0 & 0 & 0 \\ 1 & 0 & 0 \end{pmatrix} \qquad \lambda^5 = \begin{pmatrix} 0 & 0 & -i \\ 0 & 0 & 0 \\ i & 0 & 0 \end{pmatrix} \qquad \lambda^6 = \begin{pmatrix} 0 & 0 & 0 \\ 0 & 0 & 1 \\ 0 & 1 & 0 \end{pmatrix} \tag{A.3}$$

$$\lambda^7 = \begin{pmatrix} 0 & 0 & 0 \\ 0 & 0 & -i \\ 0 & i & 0 \end{pmatrix} \qquad \lambda^8 = \frac{1}{\sqrt{3}} \begin{pmatrix} 1 & 0 & 0 \\ 0 & 1 & 0 \\ 0 & 0 & -2 \end{pmatrix} \tag{A.4}$$

List of Figures

List of Tables

Bibliography

[1] A. Pich, *The Standard Model of Electroweak Interactions*, hep-ph/07054264 (2007).

[2] J. Charles *et al.* (The CKMfitter Group), *Predictions of selected flavour observables within the Standard Model*, Phys. Rev. D **84**, 033005, hep-ph/1106.4041 (2011).

[3] R. Aaij *et al.* (LHCb Collaboration), *Measurement of CP violation and the B_s^0 meson decay width difference with $B_s^0 \to J/\psi\, K^+K^-$ and $B_s^0 \to J/\psi\, \pi^+\pi^-$ decays*, Phys. Rev. D **87**, 112010, hep-ex/1304.2600 (2013).

[4] R. Aaij *et al.* (LHCb Collaboration), *Observation of $B_s \to J/\psi\, f_2'(1525)$ in $J/\psi\, K^+K^-$ final states*, Phys. Rev. Lett. **108**, 151801, hep-ex/1112.4695 (2012).

[5] V. M. Abazov *et al.* (DØCollaboration), *Study of the decay $B_s^0 \to J/\psi\, f_2'(1525)$ in $\mu^+\mu^-K^+K^-$ final states*, Phys. Rev. D **86**, 092011, hep-ex/1204.5723 (2012).

[6] R. Aaij *et al.* (LHCb Collaboration), *Amplitude analysis and branching fraction measurement of $B_s^0 \to J/\psi K^+K^-$*, Phys. Rev. D **87**, 072004, hep-ex/1302.1213 (2013).

[7] F. Abe *et al.* (CDF Collaboration), *Ratios of bottom meson branching fractions involving J/ψ mesons and determination of b quark fragmentation fractions*, Phys. Rev. D **54**, 6596, hep-ex/9607003 (1996).

[8] O. Norniella, K. Pitts *et al.* (CDF Collaboration), *BR($B_s^0 \to J/\psi\phi$ measurement and extraction of the fragmentation fractions)*, Public Note **10795** (2012).

[9] J. Beringer *et al.* (Particle Data Group), Phys. Rev. D **86**, 010001 (2012) and 2013 partial update for the 2014 edition.

[10] E. Noether, *Invariante Variationsprobleme*, Nachr. v. d. Ges. d. Wiss. zu Gö ttingen, S. 235-257 (1918).

[11] J. Goldstone, Nuov. Cim. **19**, 154, (1961).

[12] P. W. Higgs, Phys. Rev. **145**, 1156, (1966).

[13] S. Chatrchyan *et al.* (CMS Collaboration), *Observation of a new boson at a mass of 125 GeV with the CMS experiment at the LHC*, Phys. Lett. B **716**, 30, hep-ex/1207.7235 (2012).

[14] G. Aad *et al.* (ATLAS Collaboration), *Observation of a new particle in the search for the Standard Model Higgs boson with the ATLAS detector at the LHC*, Phys. Lett. B **716**, 1, hep-ex/1207.7214 (2012).

[15] H. V. Klapdor-Kleingrothaus and K. Zuber, *Teilchenastrophysik*, Teubner (1997).

[16] A. D. Sacharov, JETP Lett **6**, 24 (1967).

[17] M. Kobayashi and T. Maskawa, Prog. Theor. Phys. **49**, 652 (1973).

[18] N. Cabibbo, Phys. Rev. Lett. **10**, 531 (1963).

[19] L. Wolfenstein, Phys. Rev. Lett. **51**, 1945 (1983).

[20] The CKM fitter group, http://ckmfitter.in2p3.fr/ (Mar. 5th 2014).

[21] BaBar Collaboration, edited by P. F. Harrison and H. R. Quinn, *The BaBar Physics Book*, SLAC-R-504 (1998).

[22] S. Esen, *Measurement of $B_s^0 \to D_s^{(*)-} D_s^{(*)+}$ and determination of the $B_s - \bar{B}_s$ width difference $\Delta\Gamma_s$ using e^+e^- collisions*, Ph.D. thesis, University of Cincinnati (2012).

[23] I. Dunietz, R. Fleischer and U. Nierste, Phys. Rev. D **63**, 114015, hep-ph/0012219v2 (2001).

[24] I. Dunietz, Phys. Rev. D **52**, 3048, hep-ph/9501287 (1995).

[25] A. J. Buras, *Flavour Theory: 2009*, PoS EPS-HEP 2009, 024, hep-ph/0910.1032 (2009).

[26] C.-W. Chiang *et al.*, *New Physics in $B_s \to J/\psi\phi$: a General Analysis*, JHEP 1004, 031, hep-ph/0910.2929 (2010) and references therein.

[27] T. Aaltonen *et al.* (CDF Collaboration), *Measurement of the CP-Violating Phase* $\beta_s^{J/\Psi\phi(1020)}$ *in* $B_s^0 \to J/\Psi\phi(1020)$ *Decays with the CDF II Detector*, Phys. Rev. Lett. **109**, 171802, hep-ex/1208.2967 (2012).

[28] V. M. Abazov *et al.* (DØCollaboration), *Measurement of the CP-violating phase* $\phi_s^{J/\psi\phi}$ *using the flavor-tagged decay* $B_s^0 \to J/\psi\phi$ *in* $8\,fb^{-1}$ *of* $p\bar{p}$ *collisions*, Phys. Rev. D **85**, 032006, hep-ex/1109.3166 (2012).

[29] G. Aad *et al.* (ATLAS Collaboration), *Time-dependent angular analysis of the decay* $B_s^0 \to J/\psi\phi$ *and extraction of* $\Delta\Gamma_s$ *and the CP-violating weak phase* ϕ_s *by ATLAS*, JHEP **1212**, 072, hep-ex/1208.0572 (2012).

[30] S. Choi, *et al.* (Belle Collaboration). *Observation of a narrow charmonium - like state in exclusive* $B^\pm \to K^\pm\pi^+\pi^- J/\psi$ *decays*, Phys. Rev. Lett. **91**, 262001 (2003), hep-ex/0309032.

[31] R. Mizuk, *et al.* (Belle Collaboration). *Evidence for the* $\eta_b(2S)$ *and observation of* $h_b(1P) \to \eta_b(1S)\gamma$ *and* $h_b(2P) \to \eta_b(1S)\gamma$, Phys. Rev. Lett. **109**, 232002 (2012), hep-ex/1205.6351.

[32] S. Kurokawa and E. Kikutani, Nucl. Instrum. Methods Phys. Res. Sect. A **499**, 1 (2003), and other papers included in this Volume; T.Abe *et al.*, Prog. Theor. Exp. Phys. **2013**, 03A001 (2013) and following articles up to 03A011.

[33] T. Abe. *et al.*, *Compensation of the Crossing Angle with Crab Cavities at KEKB*, conference proceeding, (2007), hep-ex/0706.3248v1.

[34] T. E. Browder, K. Honscheid, *B mesons*, Prog. Part. Nucl. Phys. **35**, pp. 81–220 (1995), hep-ph/9503414.

[35] A. Abashian *et al.* (Belle Collaboration), Nucl. Instrum. Methods Phys. Res. Sect. A **479**, 117 (2002); also see detector section in J. Brodzicka *et al.*, Prog. Theor. Exp. Phys. **2012**, 04D001 (2012).

[36] R. Louvot, *Study of* B_s^0*-meson production and measurement of* B_s^0 *decays into a* $D_s^{(*)-}$ *and a light meson in* e^+e^- *collisions at* $\sqrt{s} = 10.87$ *GeV*, Ph.D. thesis, École Polytechnique Fédérale de Lausanne (2012).

[37] Z. Natkaniec *et al.*, *Status of the Belle silicon vertex detector*, Nucl. Instr. Meth. A **560**, 1 (2006).

[38] H. Hirano *et al.*, *A high resolution cylindrical drift chamber for the KEK B factory*, Nucl. Instr. Meth. A **455**, 294 (2000).

[39] T. Iijima *et al.*, *Aerogel Cherenkov counter for the BELLE detector*, Nucl. Instr. Meth. A **453**, 321 (2000).

[40] R. Brun and F. Rademakers, *The* ROOT *User's Guide*, http://root.cern.ch/download/doc/ROOTUsersGuideA4.pdf (Nov. 30th, 2013).

[41] W. Verkerke, D. Kirkby, RooFit *Users Manual v2.91*, http://root.cern.ch/download/doc/RooFit_Users_Manual_2.91-33.pdf (Nov. 30th, 2013).

[42] I. Adachi *et al.*, *Belle computing system*, Nucl. Instrum. Meth. A **534**, 53 (2004).

[43] M. Nakao *et al.*, *Switchless Event Building Farm for the Belle Data Acquisition System*, IEEE Trans. Nucl. Sci. **48**, 2385 (2001).

[44] R. Itoh, *BASF-BELLE AnalysiS Framework*, presented at the Computing in High-Energy Physics (CHEP 97) Conference, Berlin, Germany (1997).

[45] M. Artuso *et al.* (CLEO Collaboration), *First evidence and measurement of $B_s^*\bar{B}_s^*$ production at the $\Upsilon(5S)$*, Phys. Rev. Lett. **95**, 261801 (2005), hep-ex/0508047.

[46] G. Bonvicini *et al.* (CLEO Collaboration), *Observation of B_s production at the $\Upsilon(5S)$ resonance*, Phys. Rev. Lett. **96**, 022002 (2006), hep-ex/0510034.

[47] These results are obtained by Belle using 121.4 fb^{-1} of data and the method described in
A. Drutskoy *et al.* (Belle Collaboration), *Measurement of inclusive D_s, D_0 and J/ψ rates and determination of the $B_s^*\bar{B}_s^*$ production fraction in $b\bar{b}$ events at the $\Upsilon(5S)$ resonance*, Phys. Rev. Lett. **98**, 052001 (2007), hep-ex/0608015.

[48] B. Aubert *et al.* (Babar Collaboration), *Measurement of the $e^+e^- \to b\bar{b}$ cross section between $\sqrt{s}$ = 10.54-GeV and 11.20-GeV*, Phys. Rev. Lett. **102**, 012001 (2009), hep-ex/0809.4120.

[49] D. Besson *et al.* (CLEO Collaboration), *Observation of new structure in the e^+e^- cross section above the $\Upsilon(4S)$*, Phys. Rev. Lett. **54**, 381 (1985).

[50] This result is obtained by Belle using 121.4 fb^{-1} of data and the method described in

R. Louvot *et al.* (Belle Collaboration), *Measurement of the Decay $B_s^0 \to D_s^- \pi^+$ and Evidence for $B_s^0 \to D_s^\mp K^\pm$ in e^+e^- Annihilation at $\sqrt{s}$ 10.87 GeV*, Phys. Rev. Lett. **102**, 021801 (2009), hep-ex/0809.2526.

[51] D. J. Lange, *The EvtGen particle decay simulation package*, Nucl. Instrum. Meth. A **462**, 152 (2001).

[52] A. Abashian *et al.* (BELLE Collaboration), *Measurement of inclusive production of neutral pions from $\Upsilon(4S)$ decays*, XXXth International Conference on High Energy Physics, Osaka, BELLE-Conf-0008, (July 2000)

[53] K. Abe *et al.* (BELLE Collaboration), *Measurement of inclusive production of neutral pions from $\Upsilon(4S)$ decays*, Phys. Rev. D **64**, 072001 (2001) hep-ex/0103041.

[54] E. Barberio and Z. Was, *PHOTOS: A Universal Monte Carlo for QED radiative corrections. Version 2.0*, Comput. Phys. Commun. **79**, 291 (1994).

[55] B. Barish *et al.* (CLEO Collaboration), *Measurement of the B semileptonic branching fraction with lepton tags*, Phys. Rev. Lett. **76**, 1570 (1996).

[56] R. Brun, F. Bruyant, M. Maire, A. C. McPherson and P. Zanarini, *Geant3*, CERN-DD/EE/84-1.

[57] A. S. Dighe, I. Dunietz, H. J. Lipkin, J. L. Rosner, *Angular distributions and lifetime differences in $B_s \to J/\psi\,\phi$ decays*, Phys. Lett. B **369**, 144 (1996) hep-ph/9511363.

[58] A. Dighe, I. Dunietz, R. Fleischer, *Extracting CKM Phases and $B_s - \bar{B}_s$ Mixing Parameters from Angular Distributions of Non-Leptonic B Decays*, Eur. Phys. J. C **6**, 647 (1999) hep-ph/9804253.

[59] K. Hanagaki *et al.*, *Electron identification in Belle*, Nucl. Instrum. Meth. A **485**, 490 (2002).

[60] A. Abashian *et al.*, *Muon identification in the Belle experiment at KEKB*, Nucl. Instrum. Meth. A **491**, 69 (2002).

[61] G.C. Fox and S. Wolfram, Phys. Rev. Lett. **41**, 1581 (1978).

[62] B. Casey, *HadronB*, Belle internal note #390.

[63] J. Li *et al.* (Belle Collaboration), Phys. Rev. Lett. **106**, 121802 (2011), hep-ex/1102.2759.

[64] J. E. Gaiser, *Charmonium Spectroscopy from radiative decays of the J/ψ and ψ'*, Ph.D. thesis, Stanford University (1982).

[65] T. Skwarnicki, Ph.D. Thesis, Institute for Nuclear Physics, Krakow 1986; DESY Internal Report, DESY F31-86-02 (1986).

[66] H. Albrecht *et al.* (ARGUS Collaboration), Phys. Lett. B**241**, 278 (1990).

[67] M. Prim, Karlsruhe Institute of Technology, Germany, private communication.

[68] The `ROOT` online documentation, http://root.cern.ch/root/html/src/RooArgusBG.cxx.html#LwL.qE (December 9th, 2013).

[69] R. Mizuk, Institute for Theoretical and Experimental Physics, Russia, private communication.

[70] L. Hinz, *Lepton ID efficiency correction and systematic error*, Belle internal note #954.

[71] S. Nishida, *Study of kaon and pion identification using inclusive D^* sample*, Belle internal note #779.

[72] S. M. Flatté, *Coupled-channel analysis of the $\pi\eta$ and $K\overline{K}$ system near $K\overline{K}$ threshold*, Phys. Lett. B **63**, 224 (1976).

[73] M. Ablikim *et al.* (BES Collaboration), *Resonances in $J/\psi \to \phi\pi^+\pi^-$ and ϕK^+K^-*, Phys. Lett. B**607**, 243 (2005) hep-ex/0411001.

Danksagung

An dieser Stelle möchte ich mich bei allen Personen bedanken, die mich während meiner Forschungsarbeit und der Erstellung dieser Doktorarbeit unterstützt haben.

Professor Dr. Christian Fabjan, dem pensionierten Direktor des Instituts für Hochenergiephysik, danke ich für die freundliche Aufnahme am Hephy und sein Interesse an meiner Arbeit.

Privatdozent Dr. Christoph Schwanda, dem Leiter der Belle Arbeitsgruppe am Hephy, möchte ich meinen tief empfundenen Dank für seine hervorragende Betreuung während der letzten drei Jahre aussprechen. Von Anfang an stand er nicht nur während der wöchentlichen Besprechungen der Belle Analysegruppe, sondern auch außerhalb dieser Zeiten zur Klärung von Fragen zur Verfügung. Durch seine große Erfahrung im Bereich der Datenanalyse und der Statistik, sowie seinem detaillierten Wissen über das Belle Experiment, der CP-Verletzung und der B-Physik, konnte ich während unserer Diskussionen meine Kenntnisse in diesen Gebieten vertiefen. Aber nicht nur in Bezug auf die inhaltlichen Aspekte der Teilchenphysik, sonder auch was deren Präsentation in Vorträgen und Publikationen betrifft, habe ich unter seiner Anleitung sehr viel gelernt.

Bei Dr. Winfried Mitaroff bedanke ich mich für seine Erläuterungen zu verschiedensten Themen wie z.B. die Produktion von B_s^0 Mesonen, B_s^0 Zerfallskanäle und unterschiedlichen Aspekten des Standardmodells, die ich sehr geschätzt habe, sowie für das Korrekturlesen meiner Dissertation.

Meinen Bürokollegen am Hephy, DI Robin Glattauer, Mag. Jakob Lettenbichler und Dr. Moritz Nadler danke ich für die unzähligen Gespräche und Diskussionen sowohl über physikalische als auch nichtphysikalische Themen. Ich habe die Atmosphäre in unserem Büro immer als sehr angenehm empfunden und ich hatte mit euch eine wirklich tolle Zeit.
Bei DI Robin Glattauer möchte ich mich auch noch mal extra dafür bedanken, dass

er sich beim Korrekturlesen durch meine gesamte Dissertation gekämpft hat.

Within the Belle Collaboration I would like to express my thanks to Dr. Roman Mizuk, one of the conveners of the $\Upsilon(5S)$ group and member of the Belle internal referee committee for my analysis. His comments and expertise during the different stages of this analysis were very valuable.
Furthermore, I thank Prof. Alan Schwartz and Prof. Jin Li for their comments and the review of my analysis as members of the referee committee.

Doch auch bei aller fachlichen Unterstützung die ich am Institut für Hochenergiephysik und innerhalb der Belle Kollaboration erhalten habe, wäre diese Arbeit ohne den Rückhalt meiner Familie nicht entstanden.

Daher möchte ich mich bei meinen Großeltern Hedwig und Walter Scherer bedanken die mich von frühester Kindheit an begleitet haben. Insbesondere danke ich meinem Großvater dafür, dass er schon während meiner Schulzeit mein Interesse für Mathematik und logisches Denkvermögen gefördert hat. Es tut mir sehr leid, dass er die Fertigstellung dieser Dissertation nicht mehr miterlebt hat.

Ich danke meiner Mutter Renate Thorne von ganzem Herzen für ihre grenzenlose Unterstützung und bedingungslose Liebe. Sie ist mir nicht nur eine fürsorgliche Mutter, sondern auch eine wunderbare Freundin. Ohne sie wäre ich nicht der Mensch der ich heute bin, und dafür danke ich ihr.

Mein größter Dank gilt meinem Verlobten M.Sc. Joscha Breibeck. Obwohl er über die räumliche Trennung die durch meinen Umzug nach Wien entstand nicht glücklich war, hat er mich trotzdem bei meinem Vorhaben unterstützt und es mir nie vorgehalten. Ich danke ihm für seine Liebe, sein Verständnis, seine Freundlichkeit, ich danke ihm dafür dass er an meiner Seite steht und mich auch in schwierigen Zeiten zum Lachen bringen kann. Ich hoffe dass ich ihm all dies, was ich von ihm bekomme auch zurückgeben kann.

Curriculum Vitae: Felicitas Andrea Thorne

born: December 26th, 1984 in Steinheim/Westf., Germany

Cumberlandstrasse 111, Top 22, 1140 Vienna, Austria
Tel. +43 676 376 1917
Felicitas.Thorne@oeaw.ac.at

Professional Employment

Feb. 2011 – now Research assistant at the Institute of High Energy Physics, Austrian Academy of Sciences, working on the Belle experiment

July 2009 – Aug. 2009 Working student at the Technical University of Munich, Study of radioactive background in the solar neutrino experiment Borexino,
supervisor: Prof. Lothar Oberauer (E15, chair for astroparticle physics)

Education

Feb. 2011 – now Graduate studies in experimental particle physics at the Vienna University of Technology and the Institute of High Energy Physics, Austrian Academy of Sciences;
Ph.D. thesis at the Belle experiment at KEK ("Measurement of the Decays $B_s^0 \to J/\psi\,\phi(1020)$, $B_s^0 \to J/\psi\, f_2'(1525)$ and $B_s^0 \to J/\psi\, K^+K^-$ at Belle"), supervisor: Dr. Christoph Schwanda, thesis to be submitted in March 2014.

Dec. 2009 – Dec. 2010 Diploma thesis in experimental particle physics at the neutrino experiment Borexino ("Spectral Analysis of Neutrino and Background Events in the solar Neutrino Experiments Borexino and Lena"), supervisor: Prof. Lothar Oberauer;
degreed physicist since Dec. 2010.

Oct. 2005 – Nov. 2009 Undergraduate studies in general physics at the Technical University of Munich

Aug. 1996 – June 2005 Secondary school education; general qualification for university entrance obtained in June 2005.

Language skills German, English, French

Awards and Fellowships

Mar. 2012 Young Scientist Fellowship, Les Rencontres de Physique de La Vallée d'Aoste (La Thuile 2012)

Oct. 2005 – June 2006 Book award and gratuitous membership of the DPG (German Physical Society) for outstanding achievements in physics

Research Responsibilities and Service to the Discipline

Feb. 2012 Common Belle II SVD-PXD Meeting (chairman assistance, registration)

2010 Performed shift duties for the Borexino experiment, including detector calibration and review of data quality.

Conference Presentations

Sep. 2013 "Measurement of the Decays $B_s^0 \to J/\psi\,\phi(1020)$, $B_s^0 \to J/\psi\,f_2'(1525)$ and $B_s^0 \to J/\psi\,K^+K^-$ at Belle", Joint annual meeting of the Austrian and Swiss Physical Societies, Linz, Austria (September 3-6, 2013)

July 2013 "B_s^0 decays at Belle", European Physical Society Conference on High Energy Physics, Stockholm, Sweden (July 17-24, 2013)

Sep. 2012 "Study of $B_s^0 \to J/\psi K^+K^-$ decays at the Belle experiment", 62nd Annual meeting of the Austrian Physical Society, Graz, Austria (September 18-21, 2012)

July 2012 "B_s decays at Belle", 36th International Conference on High Energy Physics, Melbourne, Australia (July 4-11, 2012)

Feb./Mar. 2012 "Results of $B_s \to CP$ Eigenstates at Belle", XXVI Rencontres de Physique de La Vallée d'Aoste, La Thuile, Italy (Feb. 26 - March 3, 2012)

June 2011 "Study of B and B_s decays at the Belle experiment in Vienna", Joint annual meeting of the Austrian and Swiss Physical Societies, Lausanne, Switzerland (June 15-17, 2011)

Seminar Talks

Mar. 2011 — "Spectral Analysis of Neutrino and Background Events in the solar Neutrino Experiments Borexino and Lena", Student seminar, Institute of High Energy Physics, Austrian Academy of Sciences, Mar. 6, 2011

Dec. 2010 — "Spectral Analysis of Neutrino and Background Events in the solar Neutrino Experiments Borexino and Lena", Seminar on Advances in Astroparticle Physics, Technical University Munich (E15, chair for astroparticle physics), Dec. 21, 2010

Oct. 2010 — "Spectral fits for the solar neutrino experiments BOREXINO and LENA", Institute of High Energy Physics, Austrian Academy of Sciences, Oct. 15, 2010

June 2010 — "Spectral fits in the solar neutrino experiment BOREXINO", Technical University Munich (E15, chair for astroparticle physics), June 6, 2010

Teaching and Student Supervision

Mar. 2013 – Dec. 2013 — Co-advisor of Matthias Tschanter (Bachelor student), Measurement of $B^0 \to D^*\pi$ at Belle, Institute of High Energy Physics, Vienna, Austria

2010 — Advisor of working student in the context of spectral fits in Borexino, Technical University of Munich, Germany

2009–2010 — Supervision of undergraduate laboratory course (Measurement of equation of state for gases), Technical University of Munich, Germany

Oct. 2009 – Feb. 2010 — Lecture exercise course for Experimental Physics 1, examination supervisor and examination corrector, Technical University of Munich, Germany

Feb. 2009 — Lecture refresher course (including exercises) for Experimental Physics 2, Technical University of Munich, Germany

July 2008 — Lecture refresher course (including exercises) for Experimental Physics 1, Technical University of Munich, Germany

2008 — Supervision of undergraduate laboratory course (Measurement of transistor characteristics), Technical University of Munich, Germany

Outreach Activities

Mar./Apr. 2013 — Head of the month for the outreach web page `www.teilchen.at`

July 2011 — Contribution to "Perchtoldsdorfer Forschertage" at "Schulzentrum Roseggergasse", Perchtolsdorf, Austria

2011 — Co-tutor at the outreach event "Physik zum Anfassen", Vienna, Austria

Additional Qualifications

Sep./Oct. 2010 — Attendance of the International School on Astroparticle Physics, Early Universe and Gravitational Waves, Pisa, Italy (Sep. 26 - Oct. 5, 2010)

Apr. 2006 – July 2006 — Attendance at language course "Modern Chinese - Level 1", Technical University of Munich

Aug. 2003 — Participant at the "Deutsche Schüler Akademie", attended course: "The Lambda-Calculus", Bildung und Begabung e.V., Hilden, Germany

Publication list: Felictias Andrea Thorne

1. F. Thorne *et al.* (Belle Collaboration)
   "Measurement of the Decays $B_s^0 \to J/\psi\,\phi(1020)$, $B_s^0 \to J/\psi\,f_2'(1525)$ and $B_s^0 \to J/\psi\,K^+K^-$ at Belle",
   Phys. Rev. D 88, 114006, [arXiv:1309.0704 [hep-ex]] (2013).

2. F. Thorne, C. Schwanda
   "B_s^0 decays at Belle"
   Conference proceeding for the EPS-HEP 2013,
   submitted to PoS (2013).

3. F. Thorne, C. Schwanda
   "B_s^0 decays at Belle"
   Conference proceeding for the ICHEP 2012,
   PoS, 256 (2013).

4. F. Thorne, C. Schwanda
   "Results of $B_s^0 \to CP$ eigenstates at Belle
   Conference proceeding for La Thuile 2012,
   Il nuoco cimento C, Vol. 35, N.6, 373 (2012).

5. M. Wurm *et al.* (Lena Collaboration)
   "The next-generation liquid-scintillator neutrino observatory LENA",
   Astropart. Phys., Vol. 35, 685,
   arXiv:1104.5620 [astro-ph.IM] (2012).

6. Yu. N. Novikov, T. Enqvist, A. N. Erykalov, F. v.Feilitzsch, J. Hissa, K. Loo, D. A. Nesterenko, L. Oberauer, F. Thorne, W. Trzaska, J. D. Vergados, M. Wurm
   "Neutrino oscillometry at the next generation neutrino observatory",
   arXiv:1110.2983 [physics.ins-det] (2011).

Further publications

1. I. Adachi *et al.* (Belle Collaboration)
   "Measurement of the CP Violation Parameters in $B^0 \to \pi^+\pi^-$ Decays",
   arXiv:1302.0551v1 [hep-ex] (2013).

2. I. Adachi *et al.* (Belle Collaboration)
"Measurement of $B^- \to \tau^- \bar{\nu}_\tau$ with a Hadronic Tagging Method Using the Full Data Sample of Belle" arXiv:1208.4678v1 [hep-ex] (2013).

3. I. Adachi *et al.* (Belle Collaboration)
"Study of $B^0 \to \rho^0 \rho^0$ decays, implications for the CKM angle ϕ_2 and search for other four pion final states", arXiv:1212.4015v1 [hep-ex] (2012).

4. I. Adachi *et al.* (Belle Collaboration)
"Study of Three-Body $\Upsilon(10860)$ Decays", arXiv:1209.6450 [hep-ex] (2012).

5. I. Adachi *et al.* (Belle Collaboration)
"Evidence for a $Z_b^0(10610)$ in Dalitz analysis of $\Upsilon(5S) \to \Upsilon(nS)\pi^0\pi^0$", arXiv:1207.4345v1 [hep-ex] (2012).